# The formation and tensile behaviour of $\alpha$-case in fine-grained Ti-6Al-4V.

Graham Richards

March 2018

# Acknowledgements

I would like to express my sincere gratitude to Dr Martin Jackson, for his remarkable patience and perseverance throughout this project, without which it would not have been possible.
I would like to thank Mark Dixon, Dave Rugg, Eddie Saunders and Mike Wallis of Rolls Royce for their invaluable technical input into the research, as well as the supply of test material and the use of the SEM.
I am also grateful to Brad Wynne for his technical advice, and Cerise Edwards for her contributions to the project during her MEng Final Year Project.
I would finally like to thank Lucy Procter for her support and understanding, and my family and friends for pushing me when I needed it, and leaving me be when I did not.

# Abstract

The formation mechanisms of $\alpha$-case in Ti-6Al-4V were examined, and the effects of $\alpha$-case on the material under monotonic tensile loading at room temperature, elevated temperatures of 300℃ - 600℃, and superplastic forming (SPF) temperature of 920℃ were investigated. Regular arrays of cracks were found to occur in the $\alpha$-case in most instances, which were analysed by light optical microscopy, scanning electron microscopy (SEM) and electron backscatter diffraction (EBSD) to gain an understanding of the mechanisms which were operating.

The impact of various material textures on the fracture behaviour were considered, both to provide insight in to the differences in fracture morphology which were observed, and to widen the applicability of the research. Crystallographic orientation was found to be an important aspect of crack behaviour, impacting the extent of each phase of fracture.

Both oxygen and nitrogen were utilised to form the $\alpha$-case, and the behaviour of the material was found to differ between the two. This was particularly pronounced when they were introduced during SPF, where the flow stress in the material was found to dramatically alter with the presence of oxygen or nitrogen. The absorption rates of these elements were investigated with thermal gravimetric analysis (TGA), where it was found that the interaction between them could be a factor in the absorption rate and therefore formation of $\alpha$-case.

The lack of a robust definition for $\alpha$-case has been discussed, and the need for an understanding of the term which reflects developments in the field has been emphasised. A simple test for the presence of "effective $\alpha$-case" has been proposed, which would allow rapid determination of the minimum machining depth to remove the affected material.

# Contents

**Acknowledgements** **1**

**Abstract** **2**

**1 Introduction** **5**
1.1 Introduction to $\alpha$-case in titanium . . . . . 6
1.2 The relevance of $\alpha$-case in the aerospace industry . . . . . 8

**2 Formation of $\alpha$-case** **10**
2.1 Literature review . . . . . 10
2.1.1 Diffusion of oxygen and nitrogen in titanium . . . . . 10
2.2 Experimental methods . . . . . 18
2.2.1 Formation of $\alpha$-case . . . . . 18
2.2.2 Measurement of $\alpha$-case thickness . . . . . 19
2.3 Thermal gravimetric analysis (TGA) . . . . . 23
2.3.1 TGA experimental methods . . . . . 23
2.3.2 TGA results and discussion . . . . . 25
2.4 Classification of $\alpha$-case . . . . . 30

**3 Behaviour of $\alpha$-case under tension** **32**
3.1 Introduction . . . . . 32
3.2 Experimental methods . . . . . 32
3.2.1 Room temperature tensile testing at the University of Sheffield . . . . . 33
3.2.2 Room temperature tensile testing at the Advanced Forming Research Centre (AFRC) . . . . . 34
3.2.3 "Warm" tensile testing at 300℃ - 600℃ . . . . . 36
3.2.4 Interrupted tensile testing at room and elevated temperatures . . . . . 38
3.3 Crack detection and analysis techniques . . . . . 42
3.3.1 Dye penetrant inspection (DPI) . . . . . 42
3.3.2 Light optical and scanning electron microscopy . . . . 42
3.3.3 Digital image correlation (DIC) . . . . . 43
3.4 Results and discussion . . . . . 53

3.4.1 Warm tensile testing . . . . . 53
3.4.2 Crack initiation and path in $\alpha$-case . . . . . 67
3.4.3 Comparison between material with and without $\alpha$-case 72
3.5 Analysis techniques for characterising fracture behaviour . . . 75
3.5.1 Secondary electron SEM fractography . . . . . 75
3.5.2 Light optical microscopy of polished cross-sections . . 78
3.5.3 Electron backscatter diffraction (EBSD) analysis . . . 88
3.6 Factors influencing the mechanisms of crack propagation . . . 92
3.6.1 Crack mechanisms . . . . . 93
3.6.2 The influence of crystallographic texture on crack path 94
3.7 Chapter summary . . . . . 97

**4 The formation and behaviour of $\alpha$-case under superplastic forming (SPF) conditions 98**
4.1 Introduction . . . . . 98
4.2 Experimental methods . . . . . 100
4.2.1 Adaptation of the SPF tensile testing rig at the AFRC 100
4.3 Results and discussion . . . . . 105
4.3.1 Analysis of the effect of introducing oxygen or nitrogen to virgin Ti-6Al-4V during the SPF process . . . . . 105
4.3.2 Analysis of the effect of pre-existing $\alpha$-case on the SPF process . . . . . 111
4.3.3 The influence of oxygen and nitrogen on the flow stress of SPF-grade Ti-6Al-4V . . . . . 112
4.4 Chapter summary . . . . . 115

**5 Conclusions and recommendations for further work 116**
5.1 Conclusions . . . . . 116
5.2 Recommendations for further work . . . . . 117

# Chapter 1

# Introduction

$\alpha$-case in titanium is a phenomenon that has been known about for as long as the material has been used industrially. Indeed to many people, it is considered to be a long-since solved issue; if $\alpha$-case is present, then it should be removed by mechanical or chemical means, which will prevent it from causing a problem. This approach is usually sufficient for $\alpha$-case formed during manufacture, and provided that all affected surfaces are accessible, and a sufficiently conservative machining allowance is used, based for instance on the nomogram created by Dobeson et al. [1], then it is unlikely that any failure would occur on account of the $\alpha$-case.

There are situations, however, where this approach is not capable of dealing with the issue, such as in components with inaccessible surfaces, or when the $\alpha$-case forms in-service. In these cases, the primary objective is to prevent it from forming in the first place, but failing this, understanding the severity and the impact of an elevated concentration of oxygen or nitrogen at the surface is necessary, in order to determine the options available for dealing with it. This may range from doing nothing, at low relative concentrations, to reducing the rated fatigue life, or immediately scrapping the component. The latter option is likely to be the least appealing, but in the absence of sufficient knowledge and data on the behaviour of $\alpha$-case, it may also be the only available option.

This study, along with other recent work in this field [2, 3, 4, 5, 6], aims to improve the understanding of the formation and mechanical behaviour of $\alpha$-case, to the benefit of industry as well as for academic purposes. This was achieved by conducting thermal exposures on Ti-6Al-4V in various atmospheres, and tensile testing the material at room temperature, elevated temperatures of 300 - 600 ℃, and superplastic forming temperature of 920 ℃. Analysis of the material and test data was then used to assess the impact of the $\alpha$-case on the material's behaviour, and combined with thermal gravimetric analysis results to aid the understanding of the $\alpha$-case formation.

## 1.1 Introduction to $\alpha$-case in titanium

The traditional understanding of titanium $\alpha$-case was that it consisted of a discrete layer of fully stabilised alpha phase at the surface of the material, typically of the order of tens of micrometres in depth. Beyond the interface, the bulk material was considered to be free-from and therefore unaffected by $\alpha$-case. Reasonably simple measurement and detection techniques were used, such as light optical microscopy of etched cross sections, or examination of surfaces treated with a blue anodize etch, for example [7]. This allows for reliable detection of $\alpha$-case as per the above definition.

More recent research has highlighted the greater complexity of $\alpha$-case however, and it has become apparent that a discrete layer of $\alpha$-phase is not necessary for a titanium specimen to be negatively, or positively in certain situations [8, 9], affected by $\alpha$-case. This is on account of the formation mechanism of $\alpha$-case being an inward diffusion of oxygen and/or nitrogen from the surface towards the bulk, which proceeds according to standard laws of diffusion. There is therefore no boundary at which the diffusion stops - it forms a concentration gradient. The distinct boundary seen in micrographs, which is the limit of the "traditional $\alpha$-case", is simply the material's response to a particular point along this concentration gradient, where the oxygen or nitrogen interstitial content is sufficiently high to stabilise the $\alpha$-phase to an identifiable extent. However since the mechanical properties of titanium depend on far more than just the phase proportions, this visible boundary does not necessarily have any particular significance or consistency in the behaviour and extent of the $\alpha$-case. The issue of defining $\alpha$-case is discussed in more detail in Section 2.4, but it should be noted at this stage that the name can be misleading; not only is $\alpha$-phase not required for a material to suffer from "$\alpha$-case", but it is also possible for $\alpha$-alloys to be afflicted by it.

This makes the task of identifying $\alpha$-case more difficult - it is generally not practical to measure the oxygen and nitrogen concentrations on the subsurface of production parts, due to time and cost constraints. Whilst a blue etch anodizing treatment could be applied to every component in a batch, the same is not true of most of the micro-analytical methods. This leaves two main options for titanium components undergoing elevated temperature processing:

1. Assume $\alpha$-case *will* form - Include sufficient machining allowance to ensure that all oxygen or nitrogen enriched material is removed. The assumption is that every component will have $\alpha$-case, so no examination is required to inspect for it. An appropriately conservative safety factor is required on the machining allowance to justify the lack of inspection, and this option is only suitable for components without inaccessible surfaces

2. Assume $\alpha$-case *will not* form - By performing the heat treatment in a high vacuum, or entirely under a controlled atmosphere with oxygen and nitrogen measuring facilities, then $\alpha$-case can be prevented from forming. It is not possible to entirely eliminate $O_2$ and $N_2$ from the atmosphere, so it is important that the levels can be quantified, and demonstrated to be low enough to not adversely affect the material. This approach is suitable for components with inaccessible surfaces, such as shown in Figure 1.1, and those where subsequent machining could introduce problems, such as thin sections which risk distortion.

In the latter case, additional measures can be taken to reduce the effect of any oxygen or nitrogen ingress, such as oxygen scrubbers in the chamber, or protective coatings on the material surface. There are many coatings which can be utilised, [10, 11, 12, 13], which may be designed for service or production, but they come with the potential risk if they cannot be removed post-treatment, that whilst they may prevent $\alpha$-case from forming, the coating itself can have a detrimental effect on the material.

The discussion thus far applies primarily to heat-treatment processes after

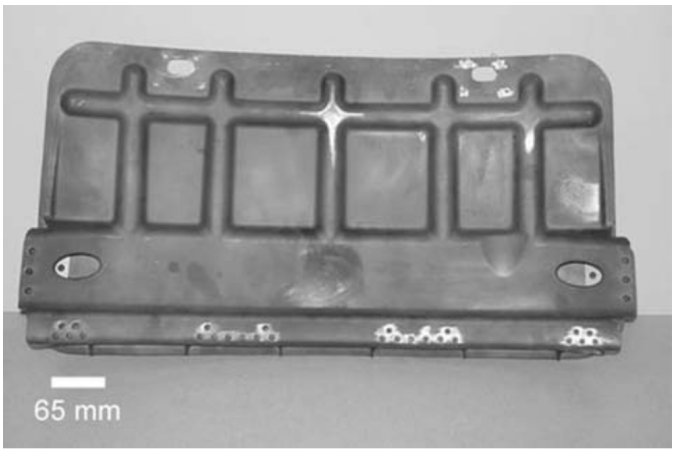


Figure 1.1: Example of a diffusion bonded, superplastic formed titanium structure [14]. If $\alpha$-case were to form in the "inflated" sections during forming, then its removal, and inspection to verify this, would be essentially impossible.

the forging stage, such as ageing and stress relief [4], and also hot forming processes, such as superplastic forming (SPF). However another stage at which oxygen or nitrogen ingress can occur is during machining, where either unsuitable parameters, or tool or lubricant failure [15] can cause sufficiently high temperatures for the rapid diffusion of interstitials. The options for prevention used during hot processes, such as surface coatings and oxygen scrubbers, are not applicable during machining, and removal by machining is clearly not a satisfactory solution. Machining under vacuum, with suitable

deoxygenated coolant, could be a failsafe solution, but the costs associated with this are likely to be prohibitive.
There is little alternative but to ensure that temperature in machining is kept low, and when it is found or expected to have increased, the assumption should be that oxygen or nitrogen ingress *will* have occurred. The extent of which can be estimated based upon recorded machine data, if it is not possible to measure it directly, but a surface treatment such as blue etch anodizing should perhaps not be relied upon, as it could produce false negatives if the ingress is not significant.

## 1.2 The relevance of $\alpha$-case in the aerospace industry

The demands that the aerospace industry place on titanium alloys are increasingly high, with service temperatures rising as nickel alloys further back in the engine are replaced by titanium. One of the main limitations to the maximum usage temperature of titanium is the material's inherent combustibility [16], which places an upper limit of ~500℃ on most alloys, although in some cases this has been increased beyond 600℃ [17]. At these temperatures, $\alpha$-case may be forming at a low rate during service, and the behaviour of this or any pre-existing $\alpha$-case will differ to that at room temperature. Detecting and quantifying the different levels of $\alpha$-case which can form, and the effect on the material's performance under the conditions encountered during service, is an important consideration, and one which is not yet well-understood.

The blue etch anodizing technique is common in the aerospace and other industries, as a simple method to detect the presence of $\alpha$-case. However as has already been discussed, it will not reveal the presence of elevated oxygen and nitrogen levels beneath a certain concentration. When evaluating the usefulness of the technique, the question must therefore be, "How detrimental are the oxygen and nitrogen levels below the blue etch anodizing detection threshold?". This is not a research technique, it is a production one, and a pragmatic approach must be taken to its use. If it can be demonstrated that it will not fail to detect harmful concentrations, then it would be largely academic that slightly elevated levels of interstitials went undetected. However this would rely on a comprehensive understanding of the interplay of mechanisms in operation, in order to confidently assess the material as safe, and this has not yet been obtained.

Alternative methods for the detection of $\alpha$-case during production and routine maintenance may therefore be required; however, in the latter case especially, these must be non-destructive if they are to be useful beyond data gathering. In production this is less critical, as sacrificial prolongations of

parts can be utilised for destructive testing purposes, if they represent the regions of a part which are at the highest risk of forming $\alpha$-case. Non-destructive techniques do not currently provide the analytical capability to assess the extent and impact of $\alpha$-case as effectively as destructive laboratory methods, but this may be possible with surface chemical analysis for example, by calibrating against destructively-assessed samples with $\alpha$-case.

# Chapter 2

# Formation of $\alpha$-case

## 2.1 Literature review

### 2.1.1 Diffusion of oxygen and nitrogen in titanium

The effect of temperature on the mechanical behaviour of $\alpha$-case is an important consideration for titanium components which are operating at elevated temperatures. Ti-6Al-4V is typically used at temperatures of up to 315℃, and other titanium alloys such as IMI 834 can be used at up to 600℃ [18], the maximum temperature generally being limited by reduced creep performance and increased absorbance of oxygen.

The two main effects that were of interest in this testing were the increasing diffusion rate of oxygen and nitrogen interstitials, and the reducing brittleness of the $\alpha$-case at the surface. The diffusion was expected to become significant from approximately 300℃,[19] and the $\alpha$-case ductility from around 500℃. [20]

In theory it should be possible to reasonably accurately calculate the diffusion rate of oxygen and nitrogen in titanium with the Arrhenius equation:

$$D = D_0 exp(-Q/RT) \tag{2.1}$$

with $D$ being the diffusion coefficient, $D_0$ the temperature-independent pre-exponential, $Q$ the activation energy, the gas constant $R$, and temperature $T$.

One apparent issue with using equation (2.1) is the considerable variation in the available data on $D_0$: the figures quoted for alpha titanium cover several orders of magnitude, from 20 $m^2$/sec to 5x$10^{-7}$ $m^2$/sec, making calculating the diffusion rate seem a somewhat futile exercise.[21] However when the diffusion rate is calculated, it can be seen that the large differences in $D_0$ ultimately have a relatively minor effect on the diffusion coefficient, $D$, as shown in Table 2.1. These values can then be used to calculate the depth to which oxygen will penetrate over a given time and temperature, to estimate

the thickness of $\alpha$-case which will be formed, with the following equation:

$$\frac{C_S - C_0}{C_x - C_0} = 1 - erf\left(\frac{2}{2\sqrt{(Dt)}}\right) \tag{2.2}$$

With, in this case, $C_S$ being the oxygen concentration at the surface, $C_0$ being the initial oxygen concentration in the material, $C_x$ the oxygen concentration at depth $x$, *erf* the error function, $D$ the diffusion coefficient, and $t$ the time in seconds.

Table 2.1: Table of diffusion data from the literature, and calculated diffusion rates, based on an initial bulk oxygen concentration of 1500 ppm, surface concentration of 12.5 wt.%, and concentration at depth '$x$' of 1 wt.%.

| $T$ (°C) | $D$ ($m^2$/sec) | $D_0$ ($m^2$/sec) | $Q$ (kJ/mol) | Ref |
|---|---|---|---|---|
| 450 | 2.2 x $10^{-19}$ | 1 x $10^{-4}$ | 203 | [22] |
| 450 | 2.15 x $10^{-18}$ | 5.0 x $10^{-11}$ | 102 | [23] |
| 450 | 3.0 $10^{-15}$ | 4.5 x $10^{-5}$ | 170 | [24] |

The value used for $C_S$ has several possibilities, depending essentially on what is the rate limiting factor in the given situation. In an atmosphere with a relatively low partial pressure of oxygen, the atmospheric concentration would be used for $C_S$. Where there is ample oxygen available, then either the concentration of oxygen in the oxide, or the solubility limit of oxygen in the metal can be used. It can be difficult to determine which of these latter two is more appropriate; it depends upon the rate of oxygen diffusion through the oxide, which varies according to the composition of the oxide, its micro and macro structure, and its integrity.

The primary oxide species which forms on commercially pure titanium is rutile, $TiO_2$ [25, 26]; whereas the oxide on Ti-6Al-4V is known to form in multiple alternating layers of $TiO_2$ and $Al_2O_3$ [27], and these layers differ in their permeability to oxygen. This can also change over time as cracks form, which they are liable to in rutile due to the Pilling-Bedworth ratio of 1.75 between titanium and rutile [28], which although in the range which often produces a protective oxide, in titanium the substantial thickness of the oxide at higher temperatures has a tendency to form cracks. This introduces the atmosphere directly to the layer below, effectively removing the influence of the cracked layer in the region of each surface breach. The magnitude of this region will be controlled by the relative diffusion rates of the cracked layer, and the one below it; if the fractured layer has a much higher diffusion coefficient than the one immediately below it, then the consequence of these cracks forming will be minimal. However if the fractured

layer has a lower diffusion coefficient than the one below it, then the effect of the crack formation would be more marked. This only applies to cracks which breach the surface; those forming in intermediate layers would be expected to reduce the diffusion rate in that layer, on account of reducing the cross section available for diffusion. The presence of nitrogen also affects the oxidation mechanisms, as oxidation of titanium nitride (TiN) will be occurring, additionally to the oxidation of the metallic titanium [29][30]. The actual composition of the oxide is considerably more complex than this however, with up to fifteen possible oxidation states for the titanium, before the aluminium and vanadium are even considered, as can be seen in Figure 2.1. These different phases can be almost impossible to distinguish experimentally, and there is little information in the literature to determine which ones are likely to form in practice. The titanium-nitrogen phase diagram, shown in Figure 2.2 is less complex and displays fewer discrete phases, particularly at the superplastic forming temperatures that this study is concerned with, of approximately 920℃, where the only nitride phases that may form are TiN and $Ti_2N$.

The approach taken by Rogers et al.[33] was to combine the various phases into four groups; $TiO_2$, mixed higher oxides, mixed lower oxides, and Ti-O (solid solution), and consider each as a single separate entity for the calculation of diffusion coefficients. This method provides a useful simplification, and the temperatures that it dealt with, between 300 and 500℃, are applicable to this study. Table 2.2 shows the diffusion rates through each of these zones at three temperatures, as calculated from experimental data. The authors calculated the uncertainty in this data to be a conservative 70 %, however the $\alpha$-titanium values are reasonably similar to the values reported in table 2.1. The main point of note is that the diffusion rates through the various oxides are consistently and substantially lower than those through the metal, indicating that it is the former that is the limiting factor in the formation of $\alpha$-case.

An interesting observation from the work of Rogers et al. [33] was that the oxidation rate of titanium was independent of the partial pressure of oxygen, between the values tested of 400 - $4x10^5$ Pa. For reference, the partial pressure of oxygen in air at sea level is approximately $2.1x10^5$ Pa, and the 1% and 5% $O_2$ mixtures utilised throughout this study equate to partial pressures of 1200 and 5700 Pa.

So far only $\alpha$-titanium has been considered, and it is not reasonable to assume that the same figures adequately represent the more complex situation of $\alpha$-$\beta$ alloys such as Ti-6Al-4V. However there is a distinct lack of data in the literature for the diffusion of oxygen in $\beta$-titanium at these temperatures. At higher temperatures (>900℃), the calculated diffusion rates in $\beta$-titanium are in some cases approximately an order of magnitude greater than in $\alpha$-titanium. At the temperatures considered in this section,

the proportion of $\beta$ phase in Ti-6Al-4V is approximately 10 %, so although it will have an effect on the overall diffusion rate, it is not the overwhelming dominating term that it would be at temperatures approaching the beta transus.

It was proposed by Dobeson et. al. [34] that in Grade 2 titanium, the limiting factor in oxygen diffusion from the surface would be the boundary region between the innermost oxide layer, and the oxygen diffusion zone (ODZ); regions 1 and 3 in Figure 2.3 respectively. This is on account of the oxygen level being sufficiently high in this region, that it will remain in the $\alpha$-phase regardless of temperature, so any higher diffusion rate exhibited by $\beta$-titanium would not be relevant once $\alpha$-case formation had commenced.
If this assertion is correct, then it may suggest a mechanism by which the different morphologies of $\alpha$-case can form. If the diffusion rate of oxygen is indeed higher in $\beta$-phase than in $\alpha$-phase, then the proportion of $\beta$-phase present in the ODZ and bulk at a given temperature would be expected to affect the oxygen distribution. A higher proportion of $\beta$-phase would tend to diffuse the oxygen away from the fully $\alpha$-stabilised layer (Region 2 in Figure 2.3 considerably faster than it could be replenished by diffusion from the surface, leading to a deeper oyxgen-enriched region, and only a shallow fully stabilised "$\alpha$-case".
Conversely, a low proportion of $\beta$-phase in the ODZ and bulk would allow the oxygen to diffuse through the ODZ only at a comparable rate to which it was being replenished from the surface, creating a region more enriched in oxygen, but shallower in total depth than the former mechanism. This would be more akin to the traditional definition of $\alpha$-case. These two distinct $\alpha$-case morphologies have been observed to occur in titanium [20], however there is not yet an accepted mechanism to explain the differences in formation. If the $\beta$-phase proportion is a key aspect of the differences in $\alpha$-case morphology, then the change from one to the other would be both temperature and alloy dependant; a simple way to begin testing the theory would be to subject a near-$\alpha$ and a near-$\beta$ alloy to the same conditions, and observe the differences in $\alpha$-case formed. It would be expected that the near-$\beta$ alloy would exhibit a shallower $\alpha$-case than the near-$\alpha$ alloy. Samples could also be exposed to temperatures where they exhibit comparable phase proportions (i.e. a higher temperature for the near-$\alpha$ alloy than the near-$\beta$ alloy), which would be expected to produce comparable $\alpha$-case morphologies, albeit with some differences caused by the variation in temperature.

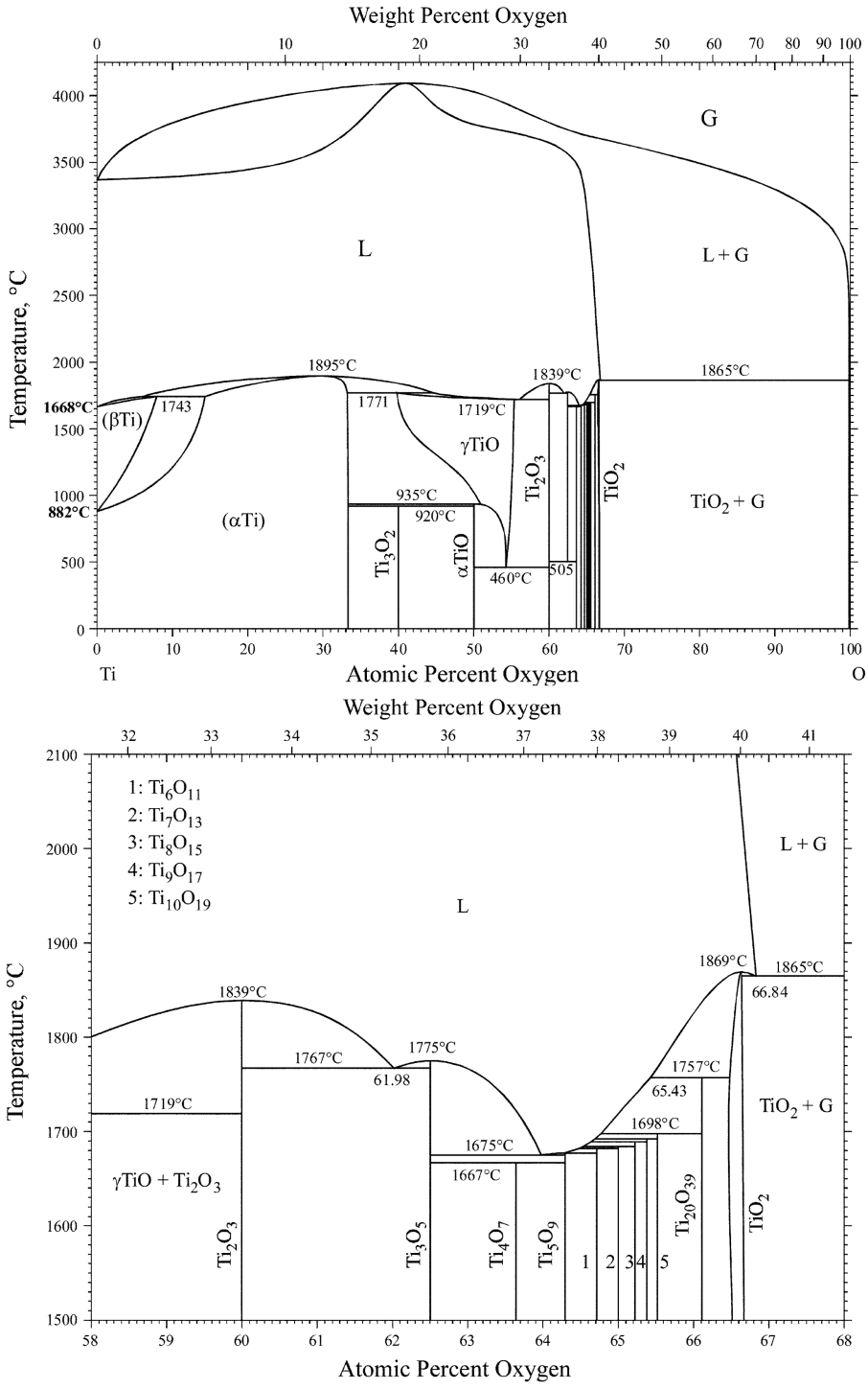


Figure 2.1: Titanium - oxygen equilibrium phase diagram, showing the large number of possible phases which can form at the test temperature. Bottom - higher resolution version of the section from 58 to 68 at.% oxygen. [31].

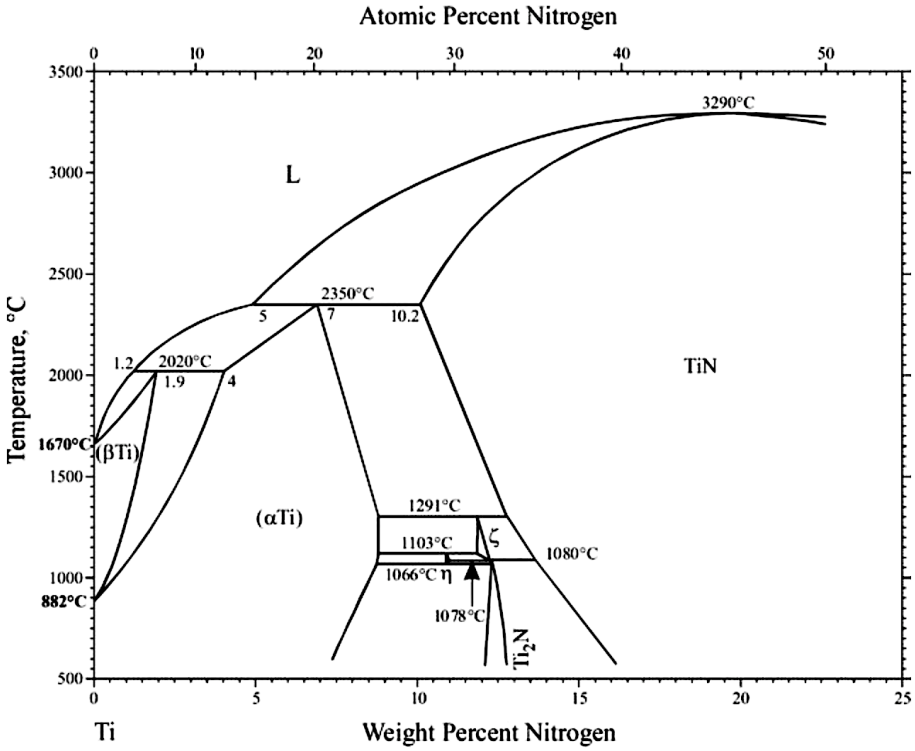


Figure 2.2: Titanium-nitrogen phase diagram. Comparison to the Ti-O phase diagram 2.1 shows the greater potency of nitrogen as an $\alpha$-phase stabiliser [32].

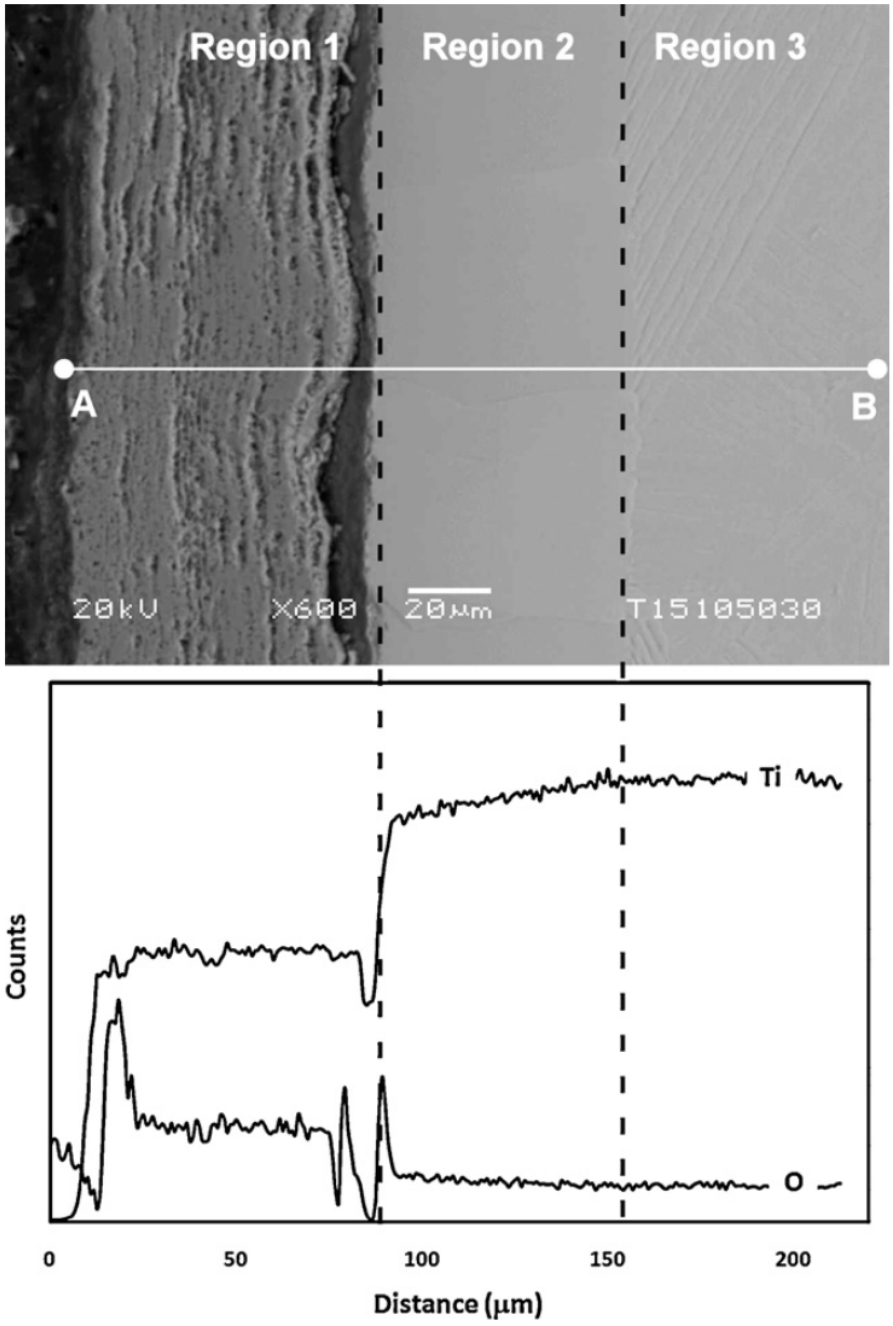


Figure 2.3: SEM image of Grade 2 titanium sample exposed to air for 30 minutes at 1050℃, showing regions 1. oxide layer, 2. $\alpha$-case, 3. oxygen diffusion zone (ODZ). Qualitative measurement of the oxygen level by energy-dispersive X-ray (EDX) spectroscopy along line A-B indicates relative compositions of each region, although the resolution suggested by this chart is noticeably finer than can actually be achieved by EDX. [34]

Table 2.2: Diffusion coefficients throughout the metal and mixed oxides [33]

| Temp (°C) | $D$ ($m^2$/sec) | | | |
|---|---|---|---|---|
| | $TiO_2$ | Mixed higher oxides | Mixed lower oxides | TiO (SS) |
| 300 | $2.9 \times 10^{-20}$ | $2.8 \times 10^{-20}$ | $2.9 \times 10^{-21}$ | $8.8 \times 10^{-22}$ |
| 400 | $1.2 \times 10^{-18}$ | $2.0 \times 10^{-18}$ | $1.6 \times 10^{-19}$ | $3.4 \times 10^{-20}$ |
| 500 | $7.6 \times 10^{-16}$ | $4.7 \times 10^{-18}$ | $1.1 \times 10^{-18}$ | $3.7 \times 10^{-19}$ |

One aspect of diffusion thought to be significant in this case is the grain boundary diffusion. It has been estimated by Brockman et al.[35] that grain boundary diffusivity can be up to five orders of magnitude greater than the diffusivity in bulk $\alpha$-Ti, and in the fine grained ($<10$ $\mu$m) superplastic-forming grade of Ti-6Al-4V that this research primarily concerns, grain boundary diffusion is likely to make a fairly significant contribution to the overall rate, although it is not thought to be the controlling factor in the overalll diffusion rate.
Measuring the grain boundary thickness, and hence the volume proportion that the grain boundaries comprise, is unfortunately imprecise by any conventional method, greatly limiting the usefulness of the data. The interaction between grains and boundaries further complicates this, as the oxygen diffusing along grain boundaries will also diffuse into the adjacent grains, due to the concentration gradient that exists between the two. This then creates a far more complicated set of concentration gradients within the alpha grains than the linear situation might predict, which affects the diffusion calculations to the point that a finite element model is required. The development work that would be required for this, including the substantial volume of experimental data necessary to validate it, is beyond what was justified by this research project, of which this represents a relatively small aspect.

The calculated diffusion figures presented should therefore be viewed with a degree of caution, as errors of an order of magnitude or more are not unlikely.

## 2.2 Experimental methods

### 2.2.1 Formation of $\alpha$-case

The majority of the specimens tested required an $\alpha$-case to be developed on the surface and sub-surface prior to testing, stabilised by oxygen, nitrogen, or a combination of the two. Titanium's affinity for these interstitials means that this was easily achievable by exposing the specimens to an atmosphere containing them at elevated temperature, however the repeatability of the setup was important in order to produce a consistent $\alpha$-case between specimens. The difficulty associated with measuring the depth of $\alpha$-case, as discussed in section 2.2.2, made this particularly relevant, since the depth of $\alpha$-stabilisation cannot not be readily quantified. This meant that there was no option of applying a correction factor to normalise the $\alpha$-case between specimens, so the aim had to be to maximise the stability of the setup.
There were only four main parameters to control: temperature, duration, partial pressure of oxygen/nitrogen, and flow rate of the controlled atmosphere. A simple system running at <80 % capacity was therefore the preference, which allowed these variables to be fixed between batches, and without the risk of machine limitations affecting batches differently.

The furnace used was a Carbolite TRT1000; a sealed horizontal tube furnace with gas flow capability, rated to 1200℃, with a hot-zone approximately 90 mm in diameter x 1000 mm in length. This was controlled by a Carbolite 2408 programmable furnace controller, allowing a multi-stage furnace cycle to be operated. The calibration of the controller and stability of the furnace was verified by positioning calibrated K-type thermocouples at the centre of the hot-zone, and 250 mm to either side, which demarcated the section which would be utilised. Between the thermocouples were small alumina blocks, which would be used to hold the test specimens when performing the thermal exposures. Pureshield bottled argon gas was flowed through the tube at two litres per minute, and the controller programmed to heat to a set-point of 900℃ and hold for one hour, with a variable ramp rate to prevent overshoot.
The readings from the three thermocouples were recorded using PicoLog software, connected to a Pico Technology TC-08 data logger. These showed consistent readings at 900℃, within 1℃ of each other. The average of these was taken, and was 3.1℃ below the temperature indicated on the furnace controller, so a +3℃ adjustment was made to the set-point on the programme cycle. Over the course of the one hour dwell at 900℃, the variation in temperature did not exceed 2℃.
These additional thermocouples could not be used whilst thermally exposing the batches of specimens, as their inclusion compromised the gas seal on the furnace. The calibration discussed above was therefore deemed to be sufficient to verify the accuracy of the system, and the errors and uncertainties

from this were assumed to apply to all thermal exposures using the same set-up and temperature.

The controlled atmosphere was achieved with the use of bottled gas mixtures supplied by BOC. These were filled to prescribed proportions of oxygen or nitrogen, with the balance being made up of argon. The four gas mixtures which were used to develop the $\alpha$-case were as follows:

1. 1 % oxygen, balance argon. Partial pressure of oxygen at atmospheric pressure = 1140 Pa.

2. 5 % oxygen, balance argon. Partial pressure of oxygen at atmospheric pressure = 5660 Pa.

3. 1 % nitrogen, balance argon. Partial pressure of nitrogen at atmospheric pressure = 1300 Pa.

4. 5 % nitrogen, balance argon. Partial pressure of nitrogen at atmospheric pressure = 6420 Pa.

Additionally, two sources of argon were utilised in some exposures; BOC Pureshield argon, with a purity of 99.998 %, and N6.0 argon, with a purity level of 99.9999 %. The former equates to an impurity level of up to 20 ppm, and the latter an impurity level of <1 ppm. These were used to produce control specimens, which were subject to the same thermal cycle as used to form $\alpha$-case, but in a neutral atmosphere.
The gas mixtures were supplied to the furnace tube via a two-stage regulator. The first stage was a HiQ C106X/1B regulator set to two bar outlet pressure, which was connected to an inline flowmeter with built in control valve, set to two litres per minute flow rate. This flow rate was kept constant throughout the thermal exposures, with the exception of the initial purge before the furnace commenced heating, when it was increased to five litres per minute.

This setup was utilised to form the $\alpha$-case on all specimens which required it, with all parameters remaining constant between batches other than the gas mixture.

### 2.2.2 Measurement of $\alpha$-case thickness

It is commonly thought that $\alpha$-case in titanium is a well-defined phenomenon, in both senses of the word; physically, in how it is detected, and theoretically, in what constitutes $\alpha$-case. These are misconceptions, and the situation is in fact considerably more complicated.

Figure 2.4 shows what would traditionally be considered to be $\alpha$-case. The lighter coloured near-surface region is the "$\alpha$-case", which abruptly changes to apparently unaffected bulk material at an approximately constant distance below the surface, in this instance around 30 $\mu$m. This visible $\alpha$-case is considered to be the entire extent of the feature when it is assessed by

this yes/no methodology, which does not allow for any non-visible affected regions. This approach is flawed in that it is focusing on one of the symptoms of oxygen enrichment, $\alpha$-phase stabilisation, rather than the cause itself, thereby imposing a lower limit on the range of detection, and offering only a binary assessment. The issue is partly one of terminology; $\alpha$-case implies a layer of fully stabilised $\alpha$-phase, however the effects of oxygen are observed at concentrations lower than that required to stabilise the $\alpha$-phase.
A more useful term which has entered common usage is "oxygen rich layer", which avoids some of the confusion, however this is still not ideal, as "rich" is a subjective term; oxygen is not the only species which can cause these effects; and "layer" suggests a discrete, homogeneous band. An alternative term is proposed; "interstitial enriched region" (IER), which although vague, does encompass the whole range of the "$\alpha$-case" phenomenon. Throughout this document, however, it will primarily be referred to as $\alpha$-case for the sake of simplicity, and because the usage of the term needs to adapt to reflect the recent developments in the field.

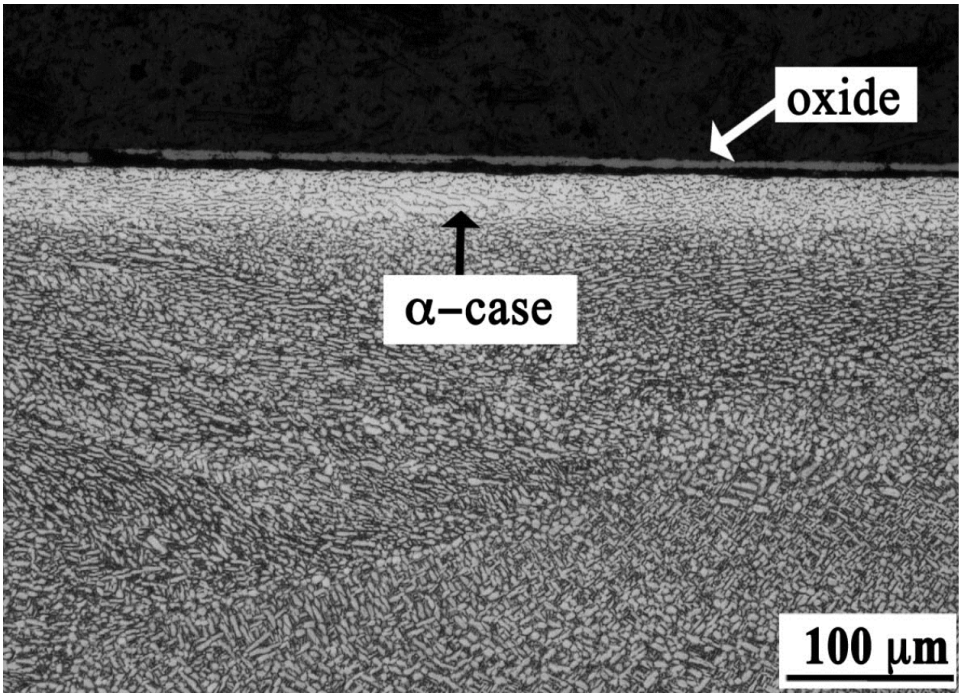


Figure 2.4: Optical micrograph of Ti-6Al-4V sample exposed to air for 500 hours at 593℃. The sample was etched in Kroll's reagent followed by Weck's reagent, to reveal the visible $\alpha$-case, which extends to a depth of approximately 30 $\mu$m below the surface. [3].

### Comparison of common evaluation techniques

There are two methods commonly employed to measure the depth of $\alpha$-case; image analysis from light optical microscopy, and micro-hardness profiling. [36, 37, 38]The former can only be utilised to detect regions which have been sufficiently enriched to stabilise or alter the microstructure of the $\alpha$-phase, whereas the latter can give an indication of the degree of enrichment below this level. A combination of the two techniques is the usual approach taken, as each provides useful information.

A third set of techniques are the various methods of chemical analysis, such as EDX spectroscopy, dynamic secondary ion mass spectrometry (D-SIMS), and glow discharge optical emission spectrometry (GDOES). These potentially offer the most informative data, as the concentration of interstitial elements can be directly measured, rather than measuring the effects of these elements, as per the two former methods. The challenges associated with obtaining reliable and accurate data with these techniques often renders them impractical or ineffective, however, so they do not provide the perfect solution.

One area where they can provide uniquely useful information is in distinguishing between the interstitial elements, in particular oxygen and nitrogen. This was investigated by Schuman et. al. [39] using a variation on D-SIMS; secondary neutral mass spectrometry (SNMS), which the author suggested gave an improvement in accuracy for quantitative measurement of light elements. This showed similar depths of diffusion for nitrogen and oxygen, in a sample of TA3V exposed to an oxygen/nitrogen/argon gaseous mixture at 720℃ for 150 minutes, as shown in Figure 2.5. This is contrary to findings by Gaddam et. al. [3], who have not detected any substantial diffusion of nitrogen in this region, but it is in agreement with the diffusion theory of Conrad [40]. The diffusion layer shown in this figure includes a region of simultaneously decreasing-oxygen and increasing-nitrogen levels, and this provides an interesting insight into the ternary-phase behaviour of these elements; TiN can form a solid solution with TiO, however in the work of Lengauer [41], there proved to be an interface between the two, with little or no coexistance. The nitrogen content in Figure 2.5 begins to increase at an oxygen level of approximately 55 at.%, meaning that the oxygen is still in oxide form, but not $TiO_2$, so it may be that the nitrogen or $Ti_2N$ has increased solubility in these other mixed oxides. The specimen preparation method involved a degree of cold-deformation of the material, which would have introduced dislocations into the matrix, and this could have affected the diffusion rate and mechanisms. This was not accounted for in the diffusion calculations, and the amount of deformation that was imposed was not stated, so the magnitude of this effect is not known. However, there are a wide range of values reported in the literature for $D$, $D_0$ and $Q$, on account of the different measurement techniques used, the variations in composition

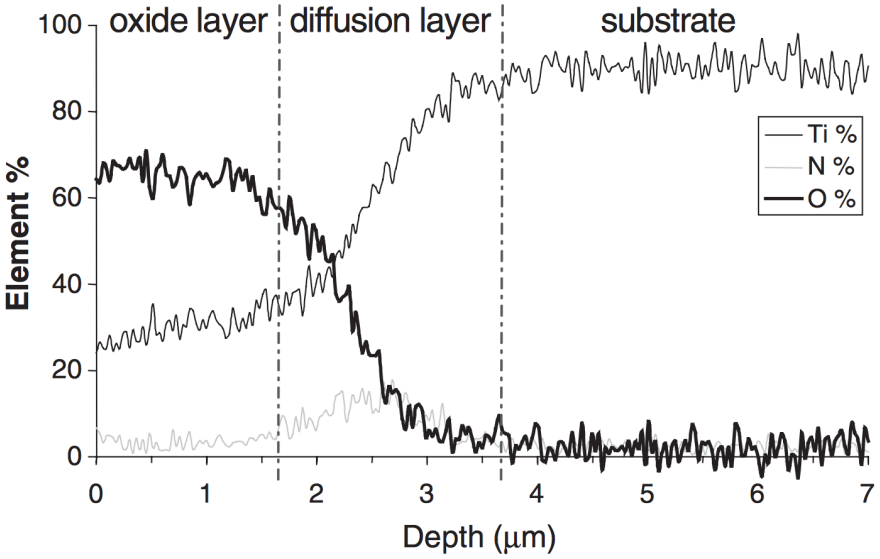


Figure 2.5: Secondary neutral mass spectrometry (SNMS) trace showing the concentrations of oxygen and nitrogen with respect to depth beneath the specimen surface, on a sample of TA3V exposed to a gaseous oxygen/nitrogen/argon mixture at 720℃ for 150 minutes. The nitrogen and oxygen concentration both reduce to the bulk level at similar depths beneath the surface. [39].

and microstructure, and the data analysis techniques employed, so there will always be a substantial level of uncertainty when leveraging these values for systems which are not exactly comparable.

## 2.3 Thermal gravimetric analysis (TGA)

### Introduction to TGA

To aid understanding of the $\alpha$-case thicknesses and properties observed in Ti-6Al-4V specimens which were exposed to both oxygen and nitrogen, TGA was employed to investigate the absorption rate of the two elements. It has been suggested [26] that the presence of nitrogen in the near-surface region will inhibit the absorption or diffusion of oxygen, based upon the oxidation rates of titanium in air versus pure oxygen, although at SPF temperatures, oxidation of the TiN may reduce this effect. By conducting TGA in atmospheres of oxygen and nitrogen, using commercially pure bottled gas from BOC, it was hoped that the absorption rate of each element could be estimated, and perhaps more importantly, the effect that each element had on the other when exposed consecutively.

### 2.3.1 TGA experimental methods

The equipment used was a PerkinElmer Pyris 1 TGA, capable of heating samples at up to 200℃/min, allowing the time at intermediate temperatures to be minimised, and thereby simplifying the analysis. The system allowed rapid switching between different atmospheres, with a small furnace volume giving a purge time of approximately 150 seconds.
The titanium specimens were sectioned from 0.73 mm thick Ti-6Al-4V membrane sheet using a Struers Minitom low-speed precision cut-off machine, to approximately 4 mm x 4 mm. All cut faces were ground to a P1200 finish to ensure consistency between samples, and the top and bottom faces retained the as-received linished surface. As it was not possible to produce identical specimens, it was necessary to normalise the results to account for the differences between individual samples. The simplest way to achieve this would have been by mass, since this was already accurately recorded by the TGA machine. However given the importance of the surface in these experiments, rather than the bulk material, it was more appropriate to normalise based on the surface area. It was assumed that given the short durations of thermal exposures, the centre of the specimens would not reach a state of equilibrium, therefore the small variations in mass between samples would not have a significant effect on the results. Over longer time periods this would not be the case, and the absorption rate would be expected to reduce as the oxygen and nitrogen content throughout the material increased towards saturation. The TGA test matrix is shown in Table 2.3.1. Specimens were retained after exposure, to allow some to be examined using standard metallographic procedures, and hardness profiles measured using a Struers Durascan 70 hardness tester.

Table 2.3: Thermal gravimetric analysis (TGA) test matrix. Specimens were approximately 4 x 4 x 0.7 mm Ti-6Al-4V membrane sheet, with as-received linished faces, and P1200 ground faces. Exposure temperature was 900°C for all specimens. Heat-up was always performed under the first atmosphere, the transition between atmospheres was performed at-temperature, and cool-down was always under argon.

| **Thermal gravimetric analysis test matrix** | | | | | | |
|---|---|---|---|---|---|---|
| | **First atmosphere** | | | **Second atmosphere** | | |
| Test No. | Gas | Flow rate (ml/min) | Duration (mins) | Gas | Flow rate (ml/min) | Duration (mins) |
| 8 | $N_2$ | 20 | 15 | $O_2$ | 20 | 15 |
| 9 | $N_2$ | 20 | 30 | - | - | - |
| 10 | $O_2$ | 20 | 15 | $N_2$ | 20 | 15 |
| 11 | $O_2$ | 20 | 30 | - | - | - |
| 14 | $N_2$ | 20 | 60 | - | - | - |
| 15 | $O_2$ | 20 | 60 | - | - | - |
| 16 | $O_2$ | 20 | 30 | $N_2$ | 20 | 30 |
| 17 | $N_2$ | 20 | 30 | $O_2$ | 20 | 30 |
| 22 | $O_2$ | 50 | 60 | - | - | - |
| 23 | $N_2$ | 50 | 60 | - | - | - |
| 24 | $O_2$ | 50 | 30 | $N_2$ | 50 | 30 |
| 25 | $N_2$ | 50 | 30 | $O_2$ | 50 | 30 |
| 26 | $O_2$ | 20 | 120 | - | - | - |
| 27 | $N_2$ | 20 | 120 | - | - | - |
| 28 | $O_2$ | 20 | 60 | $N_2$ | 20 | 60 |
| 29 | $N_2$ | 20 | 60 | $O_2$ | 20 | 60 |

### 2.3.2 TGA results and discussion

One of the main expectations for the TGA was that specimens which were exposed to nitrogen prior to oxygen, would show a decrease in oxygen absorption rate, compared to those which were not exposed to nitrogen. However the initial results, shown in Figure 2.6, suggest that this is not the case, and perhaps even the opposite occurred: the presence of nitrogen in the material *increased* the oxygen absorption rate, and increased levels of oxygen in the material were protective against nitrogen absorption.

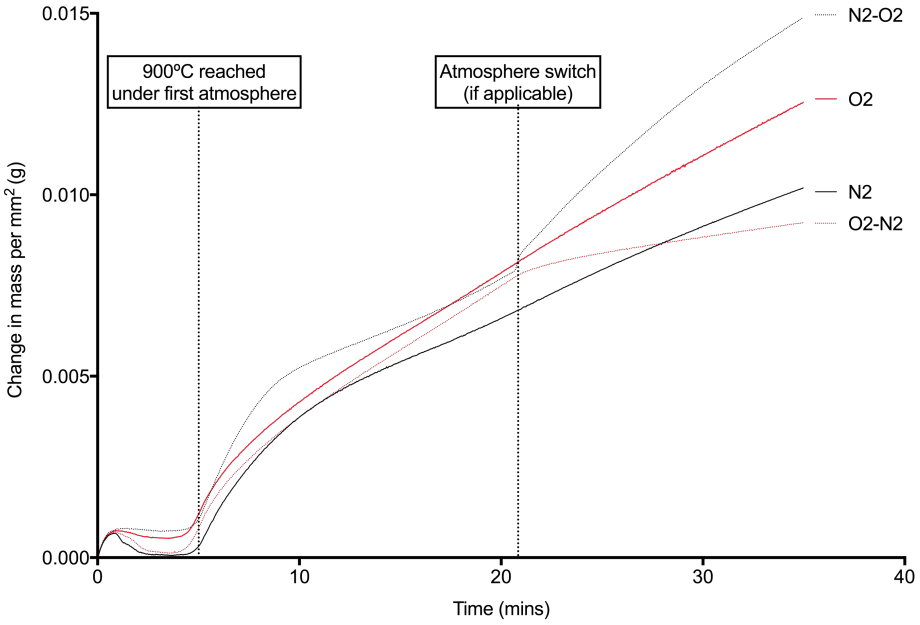


Figure 2.6: Graph showing the increase in mass of Ti-6Al-4V specimens under oxygen and nitrogen atmospheres at 900℃. The units have been normalised to account for minor (<5 %) variation of surface area between specimens.

Before any such surprising conclusions could be drawn, as well as conducting further experiments, it was necessary to investigate the basis of comparison between sections of the graph, as it was not clear which regions could be considered equivalent. The first five minutes of the graph can be largely disregarded, as this was the section of rapid heating to the test temperature of 900℃. The subsequent section, between five and 20 minutes, can be broken down in to two phases:

1. Phase 1. Rapid increase in mass, for approximately 1.5 minutes (oxygen) or three minutes (nitrogen). Prior to this point, the material was as-received and free of an oxygen or nitrogen enriched layer, with the

exception of anything absorbed in the short heat-up phase. The rate of increase in mass was higher in the nitrogen atmosphere than the oxygen atmosphere.

2. Phase 2. Steady state increase in mass, at a lower rate than in Phase 1. The rate of increase in mass was the reverse of Phase 1 - it was higher in an oxygen atmosphere than in a nitrogen atmosphere.

The specimens which remained in the same atmospheres throughout the experiment, shown by the solid lines, maintained a roughly constant rate of increase in mass from the beginning of Phase 2, to the end of the exposure at 35 minutes. This two-phase growth rate is similar to previously reported TGA results of oxygen absorption in titanium [42]. However those which were switched to the other atmosphere after 20 minutes entered additional phases:

1. Phase 3. The change in rate occurred approximately one minute after the switching point, which correlated with the time taken to purge the system. The specimen which was switched from oxygen to nitrogen showed a sharp increase in rate for approximately 30 seconds. This is the only specimen which exhibited this phase.

2. Phase 4. The specimen switched from nitrogen to oxygen, decreased slightly to a steady state, and the specimen switched from oxygen to nitrogen decreased substantially, and was also steady until the end of the exposure.

Table 2.4: Rate of increase of mass slopes of various phases of the TGA curves shown in Figure 2.6

| | | **Rate of increase of mass (%/min/mm$^2$)** | | | |
|---|---|---|---|---|---|
| **Test no.** | **Atmospheres** | **Phase 1** | **Phase 2** | **Phase 3** | **Phase 4** |
| 11 | $O_2$ | 0.097 | 0.033 | - | - |
| 9 | $N_2$ | 0.096 | 0.025 | - | - |
| 10 | $O_2$ - $N_2$ | 0.098 | - | 0.009 | |
| 8 | $N_2$ - $O_2$ | 0.123 | 0.024 | 0.160 | 0.044 |

Oxidation of titanium nitride is an established phenomenon [29, 43, 41], where the nitrogen in the structure is replaced by oxygen. If such a reaction was occurring during the TGA experiments, then it would manifest itself as an artificially low rate of oxygen absorption in the specimens which were initially exposed to nitrogen, on account of the mass of the nitrogen being lost to the atmosphere. Measuring the magnitude of this effect would not have been trivial, and was beyond the scope of this research, however by analysing the exhausted gas from the TGA, or the composition of the oxide/nitride layers, it should be possible to estimate the impact of it. This may allow verification or invalidation of the results presented here.

The simplicity of TGA gives it some limitations, and in this instance the primary concern was an inability to distinguish between oxygen or nitrogen absorbed into solid solution in the metal; and oxide or nitride formed on the surface. Whilst this was largely inconsequential in the single-gas tests, for the two-gas tests it caused uncertainty about whether it was the nitride, or the nitrogen-rich titanium, which was affecting the oxygen absorption, and vice versa. It was not feasible to resolve this experimentally, so assumptions had to be made based upon the information in the literature. A somewhat surprising aspect of the results was the similarity between the oxygen and nitrogen absorption rates. In both cases, the oxide or nitride layer was expected to have formed rapidly as the temperature increased. However given the reported values for oxygen diffusion in $TiO_2$ are around 50 times higher than in $\alpha$-Ti [44], and higher still in the sub-stoichiometric titanium-oxides, whereas the diffusion of nitrogen in TiN has been measured to be approximately 30 times *lower* than in $\alpha$-Ti, as shown in Figure 2.8, it may be expected that there would have been a substantial difference in rate of mass gain between the two. There are a number of possible explanations for this disparity; the complex oxide and nitride structure that exists in Ti-6Al-4V compared to pure $\alpha$-titanium, as mentioned in Section 2.1.1, is a likely contributing factor, as the overall difference in nitrogen and oxygen coefficients through these mixed oxides and nitrides is not known, but is unlikely to be the same as for the simple case. The formation time for the oxides and nitrides is also uncertain, with wide ranging values reported in the literature [28, 33, 43], so it is possible that the primary cause of the mass gain measured was the early formation of these, rather than longer range diffusion where the rate limitations would have a greater effect.

Cassar et. al. [45] noted that one effect of the diffusion coefficient of oxygen being higher in $TiO_2$ than in $\alpha$-Ti was that the rate of diffusion could be maintained at its maximum, regardless of the thickness of the oxide layer that formed, whereas the same was not true of nitrogen diffusion, as the nitride layer would provide an increasingly resistant barrier to further absorption [46]. The constant rate of mass increase that can be observed in Figure 2.7 for both oxygen and nitrogen over the course of one hour at 900°C however, suggested that either, the diffusion rates through neither oxide nor

nitride were rate limiting, or that these experiments exhibited only the early, constant rate stages of formation. The latter option does not appear to be the case, as hardness profiling, an example of which is shown in Table 2.5 and also in Figure 3.27, showed a significant depth of hardening, indicating that substantial oxygen and nitrogen diffusion in to the bulk material had occurred. However the titanium-nitride layer may not have proceeded to complete formation of TiN in the duration of these experiments, instead forming intermediate compounds of $TiNO_3$ and $Ti_2N$, which would have had greater transparency to oxygen and further nitrogen ingress, and therefore their presence would be unlikely to be detected from the TGA curves. Analysis of the surface using a technique such glancing-angle X-ray diffraction could potentially have determined which phases were present, although the resolution may have been insufficient, and some form of microprobe analysis would have been better suited.

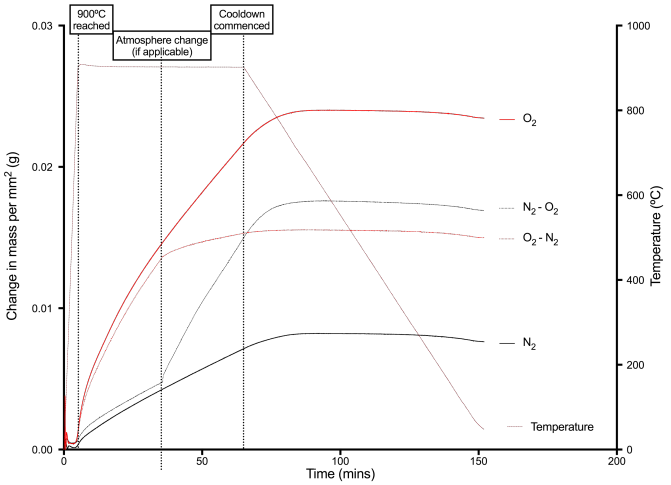


Figure 2.7: Graph showing the increase in mass of Ti-6Al-4V specimens under oxygen and nitrogen atmospheres at 900℃. The test duration was double that shown in Figure 2.6, but the rate of increase of mass remained constant throughout. The absorption can be seen to largely cease between 750℃ and 700℃ during cooldown.

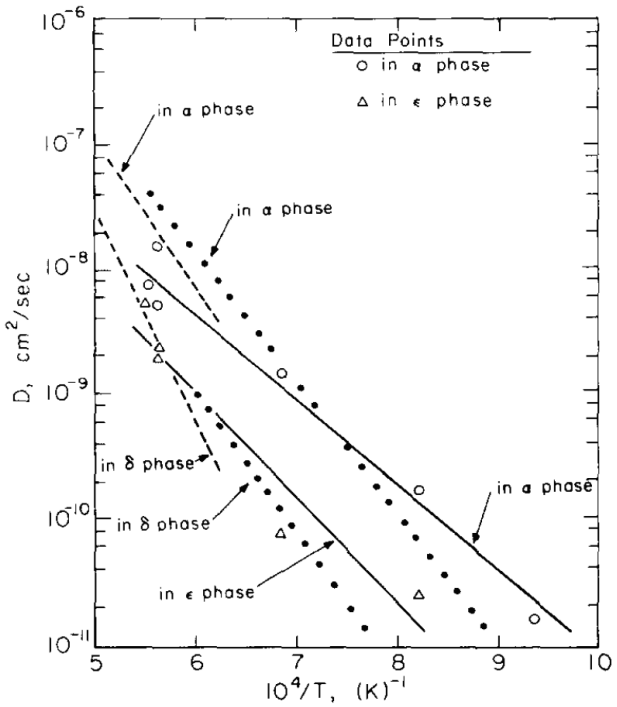


Figure 2.8: Diffusion coefficients of nitrogen in $\alpha$-titanium, and $\gamma$ and $\epsilon$ titanium-nitride phases, showing the substantially lower coefficient in titanium-nitride compared to metallic titanium [47].

Table 2.5: Measurement of visual $\alpha$-case depth by light optical microscopy, in three specimens used for TGA. Approximately 80 individual measurements were taken across top and bottom faces of each specimen, with depth of hardening measured by micro-Vickers hardness profiling as a comparison

| **Ti-6Al-4V alpha case depth measurements** | | | |
|---|---|---|---|
| **Specimen** | **Visual $\alpha$-case depth** | | **Depth of hardening ($\mu$m)** |
| | Depth ($\mu$m) | St. dev. ($\mu$m) | |
| 4 | 65 | 18 | 140 |
| 7 | 71 | 7 | 130 |
| 8 | 44 | 21 | 90 |

## 2.4 Classification of $\alpha$-case

The apparently simple task of defining $\alpha$-case, is in fact one of the major challenges associated with it, and any useful definition must be context dependent. It is generally understood to be an entirely negative feature, and it is sensible that this idea is maintained. In situations where a subsurface region is deliberately enriched in oxygen or nitrogen to benefit properties such as wear resistance [48], then this should be referred to by a different term to avoid confusion.
The requirement for context dependence to the definition is linked to the need for $\alpha$-case to be a negative effect; a given level of oxygen enrichment may cause surface cracking and a severe reduction in elongation-to-failure at room temperature, but have no detrimental effect at 500℃. The same material may therefore be considered to exhibit $\alpha$-case if its application is at room temperature, but not if it is to be used solely >500℃. It is possible that the surface will form short cracks at 500℃, which do not propagate under monotonic loading due to the ductility of the bulk material. However if cyclic loading is involved, then premature failure is likely to occur, so loading regime must also be considered. Conversely, the work of Cassar et. al. [45] showed that certain forms of nitrogen-stabilised case would produce compressive growth stresses, which could potentially lead to *improved* fatigue crack initiation resistance.
It is common for materials used at elevated temperatures to repeatedly be cooled to room temperature in operation, which may impact on the loading regime, because even if all loading is monotonic, this thermal cycling can cause crack growth. The applied stress at each temperature throughout the range of operation must also be considered, because although a component may be considered to be unaffected by $\alpha$-case at the normal operating temperature, this may not be the case during the heat-up phase, and so the stress at the lower temperatures must be sufficiently low to not cause crack initiation or growth.

Two sets of factors must therefore be taken into account when classifying $\alpha$-case.
Firstly, the physical properties of the material, as would usually be used to define $\alpha$-case:

1. The depth of material with increased oxygen/nitrogen concentration.
2. The concentration of these elements.

Or, when possible:

3. The oxygen/nitrogen concentration gradient from surface to bulk.

These attributes must then have context applied, to include the following, for example:

1. Normal temperature of operation
2. Minimum temperature of operation
3. Loading regime (monotonic/cyclic
4. Operating environment
5. Surface treatments applied
6. Expected surface wear

The combination of these two sets of information on the material and application can be used to determine whether the material should be considered to exhibit $\alpha$-case or not. This can be simplified to a more basic definition:
"*$\alpha$-case is the enrichment of oxygen or nitrogen in the surface region of titanium, sufficient to cause premature failure under operational conditions.*"

# Chapter 3

# Behaviour of $\alpha$-case under tension

## 3.1 Introduction

Understanding how different morphologies and degrees of $\alpha$-case responded under tension was one of the central focuses of this study, and has also been the subject of other recent research [49, 34]. The tensile behaviour is particularly important because, along with fatigue, it is one of the main scenarios where the detrimental effects of $\alpha$-case become apparent. The work was broken down into two main sections; room temperature, and elevated temperature, between 300℃ and 600℃. This served two purposes; firstly, it represented the likely range of operational temperatures for the material, and secondly, it was expected to provide a change in mechanism as the temperature increased, which could be used to identify more ways in which the $\alpha$-case was affecting the material.

## 3.2 Experimental methods

The Advanced Forming Research Centre (AFRC) at the University of Strathclyde is a state of the art testing facility, containing a wide variety of equipment for research into forming and forging techniques. Amongst these is a Zwick Roell Z250 tensile testing machine, equipped with an electric furnace and sealed retort, allowing for tensile tests to be performed at high temperatures under protective, or otherwise, atmospheres. This machine was utilised for three distinct projects; warm tensile testing, interrupted tensile testing, and superplastic forming (SPF) testing, in various controlled atmospheres as well as air. The first two projects are discussed here, whilst the latter is discussed in Chapter 4.

### 3.2.1 Room temperature tensile testing at the University of Sheffield

The initial tensile testing trials were conducted at the University of Sheffield, using both a Hounsfield 20 kN horizontal test rig, and an Instron 150 kN vertical test frame. These were utilised to determine the optimum parameters to include in the full test matrix, and provided valuable data on the behaviour of the $\alpha$-case under tension. These results are not presented here, as many of them are isolated and therefore of limited use for further analysis, and the full programme of testing conducted at the AFRC provides a more complete set of data.
In addition to optimising test parameters, these test frames were used to trial the various techniques for crack detection, such as in-situ dye-penetrant inspection (DPI) and microscopy, shown in Figure 3.1. The design of the Hounsfield made it more suitable for such trials than the larger machines, and its portability also aided access when developing the bespoke digital image correlation (DIC) system.

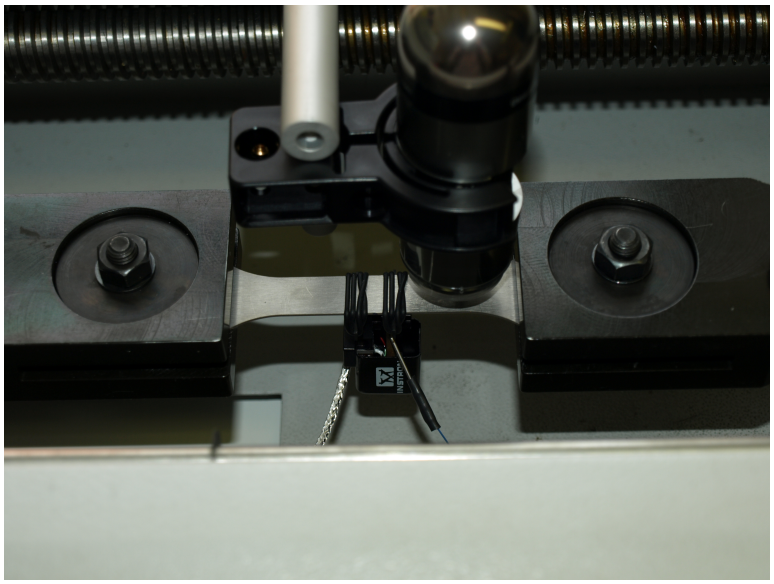

Figure 3.1: Photograph of a tensile test specimen in the Hounsfield test frame, with a digital light microscope fitted to attempt to record the formation of surface cracks.

### 3.2.2 Room temperature tensile testing at the Advanced Forming Research Centre (AFRC)

The test specimen design that was used for all sets of testing at the AFRC was that specified by ASTM E2448, shown in Figure 3.2. This was selected primarily for the SPF section of the testing, which had the most demanding requirements, but it also proved suitable for the room temperature and warm tensile testing. Three different forms of Ti-6Al-4V were tested; 0.7 mm thickness SPF-grade "membrane" sheet, uni-directionally rolled (UD) plate, and cross-rolled (XR) plate. The membrane sheet is so-called due to its application as the inside layers in SPF sandwich structures, where it forms the internal webs between the outer plates. The details of its production are not publically available, due to the proprietary nature of the processes required to developed the fine-grained microstructure, however the result is a sheet which does not exhibit a strong crystallographic texture in any one direction.
The UD plate was included for its strong basal texture, due to the rolling process being performed only in a single direction, giving a contrast to the uniformly textured membrane, which it was hoped would allow any texture-related effects on the behaviour to be isolated.
The XR plate was hot-rolled in two directions at 90 degrees to each other, giving a structure with alternating textures through the thickness. This was intended to help quantify the impact which texture had on the crack growth, by potentialy allowing individual cracks to propagate through multiple regions of differently textured material.

The plate material was sectioned to 1 mm thickness to match that of the majority of the sheet, using electro discharge machining (EDM), and the same technique was used to cut all of the profiles for the tensile specimens. An unwanted effect of the EDM process is the creation of a re-cast layer on the surface of the material, of the order of several microns in depth. This is known to reduce the fatigue resistance of titanium [50], and it was also expected to degrade the tensile properties in monotonic loading, in addition to clouding the effects of $\alpha$-case. This was not considered to be an issue on the edges of the samples following cutting of the profiles, but the plates which were sectioned down to 1 mm thickness exhibited this layer across the entire face of the sample. Since this surface was to be the focus of the project, it was important to completely remove this layer, without having a noticeable impact on the substrate material.
The specimens were therefore chemically etched in a solution of 6 % $HNO_3$, 2 % HF in distilled water, for fifteen minutes in five minute intervals, with very light abrasion with a paper towel between stages. This was effective at removing the re-cast layer and revealing the unaffected bulk Ti-6Al-4V underneath. The ratio of nitric acid to hydrofluoric acid in pickling solutions is important to prevent hydrogen embrittlement of the titanium, which can

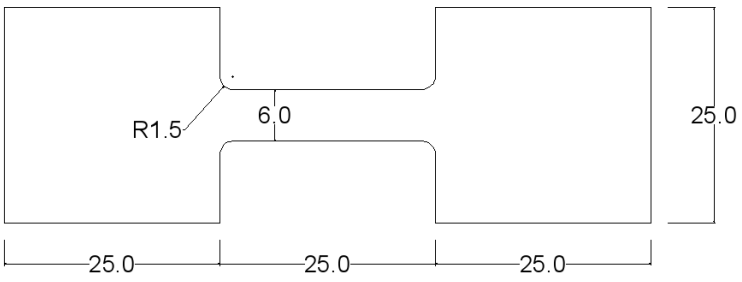


Figure 3.2: Superplastic forming test specimen used throughout all phases of this testing at the Advanced Forming Research Centre, as per ASTM E2448.

occur when the HF:$HNO_3$ ratio is too high. Too low, and the nitric acid causes passivation of the titanium surface [51, 52]. The latter situation is clearly the more preferable of the two, since it does not have a detrimental effect on the material, only the pickling process. Solutions should therefore be selected which are towards the lower side of the optimum HF:$HNO_3$ ratio, and as the operation proceeds the ratio will reduce further, so there is no risk of embrittlement.

$\alpha$-case is thought to remain brittle at temperatures up to approximately 500 °C [20]. Above this temperature, the ductility increases as dislocation motion becomes less restricted and more slip systems become favourable, and therefore its propensity for cracking was expected to be reduced. The effect of this on the behaviour of cracks that formed in terms of spacing, length and path was not known, nor whether the elevated temperature would reduce the detrimental effect that alpha-case has on overall mechanical properties; however the expectation was that its behaviour under tension is likely to differ from what has been observed when tensile testing at room temperature. A previous study by Daeubler et. al. [53] on IMI834 found that although cracks formed in the $\alpha$-case when uniaxially tensile tested at 600℃, these did not propagate to the bulk, and the failure mechanisms were similar to specimens without $\alpha$-case

The diffusion of interstitial elements becomes significant in the short-

term above approximately 350 °C [19], so it was expected that below this temperature the crack behaviour would be similar to room temperature, whilst above it some diffusion of the oxygen from the $\alpha$-case into the bulk would occur, increasing the depth but reducing the degree of stabilisation of the $\alpha$-case, therefore altering the crack behaviour.

### 3.2.3 "Warm" tensile testing at 300℃ - 600℃

The tensile testing machine used for these tests, as per the SPF testing, was a Zwick/Roell Z250, fitted with an Xforce K 250 kN load cell. This load cell has a significantly greater capacity than was required for these tests, which is generally not considered to be best practice, however the calibration certificates for this load cell indicated an error of only 0.23 % at the expected load; sufficiently low to be considered statistically insignificant in this context.

The machine was fitted with a 1600℃ split tube furnace, with resistive wire elements providing three independently controlled heat zones. The furnace contained a Kanthal APM (FeCrAl) retort, attached to water cooled flanges at either end and sealed with nitrile O-rings to provide a gas-tight system.
The lower O-ring was removed after test 17, and replaced with a fibrous seal, due to minor binding issues causing steps in the load reading. The magnitude of these steps was typically two to three Newtons, however in the SPF tests, discussed in Chapter 4, this represented up to 20% of the total load, so a potential small reduction in gas sealing was considered worthwhile to remedy it. The probability of air infiltrating the system was low, as the Pureshield argon was fed in under pressure through the lower flange, and exhausted at the top of the retort. The flow of the exhausted argon was continuously monitored, and due to the higher density of argon compared to air, the likelihood of air entering through the lower seal was considered to be low.

To provide fine temperature control, five calibrated N-type thermocouples were positioned within the furnace; one in contact with the sample, one in air adjacent to the sample, and the three others in contact with the interior of the retort, vertically spaced approximately 200 mm apart. For the SPF tests, due to the pronounced effect that temperature can have on flow stress, and the relatively long duration of the tests, it was important to obtain not only the correct temperature in the samples, but a homogeneous temperature throughout the retort.
The three independent heating zones in the furnace allowed for sufficient adjustment to obtain a temperature variation of <1℃ throughout the retort, taking into account the individual thermocouple calibration correction, and this was maintained throughout the duration of the tests. This is significantly lower than the ± 6℃ required by the ASTM E2448-11 standard.

At the lower operating temperatures used in the warm tests it was overly time consuming to obtain perfect balance between the five thermocouples, and less critical due to the shorter test duration, smaller specimen extension, and reduced temperature sensitivity. The aim, therefore, was to obtain temperatures in the sample and air within 1℃ of each other, and 0.5℃ of the target test temperature. Occasionally time constraints prevented both of these conditions being met simultaneously, in which case obtaining the correct temperature in the sample was the priority.
The ramp rate was set at 12℃/min for all tests, and the readings from all thermocouples recorded throughout the majority of the warm-up phase at 1 Hz, so that any variation in the heating profile for each sample could be accounted for in the results.

Prior to testing, the thickness and width of all samples were measured with a calibrated digital micrometer, to an accuracy of $\pm$ 2 $\mu$m, and gauge length and total sample length were measured with a pair of digital calipers to an accuracy of $\pm$ 25 $\mu$m. Samples were also measured in the same manner following removal from the sample holder, however the accuracy of the gauge and overall length measurements was greatly reduced due to the samples having been tested to fracture, as shown in Figure 3.3, and/or experiencing some deflection during the tests, an example of which is shown in Figure 3.4.
A pre-load of 25 N was applied to the specimens prior to the test commenc-

Figure 3.3: Example of specimen which fractured during testing, limiting the accuracy of subsequent length measurement.

ing, in order to allow the self-aligning mechanism in the tooling to operate, and to remove any backlash in the system. It became clear that in some of the tests, this pre-load was insufficient, as the load/displacement curve displayed a constant load of 26 - 90 N initially, before rapidly increasing once

Figure 3.4: Example of deflection seen in some specimens following testing, limiting the accuracy of subsequent dimensional measurements.

the slack in the tooling had been removed. This pre-load was maintained for the remainder of the tests regardless, for the sake of consistency, and the curves adjusted retrospectively, by removing the first section of the curve where the load was <100 N. The was essentially the same as applying a 100 N pre-load to the machine, rather than the 25 N which was actually used.

### 3.2.4 Interrupted tensile testing at room and elevated temperatures

One of the intentions of the project was to develop a constitutive model to explain the crack growth in $\alpha$-case, taking into account the chemical composition of the layer, the crystallographic orientation, and the stress and strain within the material. For this it was required to obtain information on the cracks at various strains, and this was achieved using the same tensile testing setup as described in Section 3.2.2. Since the cracks grow from the surface to bulk of the specimens, and may not extend to the edge, their depth can not be directly measured in-situ, and the small scale of the cracks makes non-destructive measurement techniques difficult. The solution was therefore to conduct a number of tests, and interrupt them at specific strains, followed by sectioning to allow the cracks to be imaged in cross section. This had the additional benefit of providing information on crack path and the effects of crystallographic orientation in addition to crack depth, which would not be achievable with non-destructive techniques.

The interrupted tensile testing was conducted in the same manner as the warm tensile testing, with two differences; firstly, the tests were terminated at pre-set strains, rather than progressing to failure, and the range of test temperatures included room temperature. The purpose of this was

to investigate the crack growth with respect to strain. It would have been preferable to measure this in-situ during extension, which would have ensured consistency through the different levels of strain, since it would be the same sample in every case. However the only way to accurately measure the cracks was by cross-sectioning the samples, which not only requires the tests to be stopped to remove the sample, but it is destructive. Differences between samples were therefore inevitable, since the material could never be entirely homogeneous. In addition to allowing accurate depth and spacing measurements to be made, however, this technique also had the benefit of revealing the crack path and its relationship with crystallographic orientation.

It was decided that testing a relatively small number of different strains, at four different elevated temperatures, would be preferable to testing greater number of strains at one or two temperatures. To ensure that a full crack depth versus strain profile was captured, a greater number of different target strains were included in the room temperature tests, as the reduced time required for these tests allowed a larger number to be conducted.

Table 3.1: Test matrix for interrupted tensile test specimens from Ti-6Al-4V membrane sheet material. Tests were terminated at pre-set strains, rather than fracture, except as indicated. All tests above room temperature were conducted in an argon atmosphere. An actual strain value below the target strain indicates that the specimen fractured before the target strain was attained.

| **Ti-6Al-4V membrane interrupted tensile test specimens** | | | | | |
|---|---|---|---|---|---|
| **Specimen** | **Target strain** | **Actual strain** | **Peak stress (MPa)** | **Temp** | **Condition** |
| 1 | 0.020 | 0.020 | 603 | 300 °C | $O_2$ $\alpha$-case |
| 2 | 0.060 | 0.060 | 731 | 300 °C | $O_2$ $\alpha$-case |
| 3 | 0.100 | 0.100 | 770 | 300 °C | $O_2$ $\alpha$-case |
| 4 | 0.020 | 0.020 | 550 | 400 °C | $O_2$ $\alpha$-case |
| 5 | 0.060 | 0.060 | 669 | 400 °C | $O_2$ $\alpha$-case |
| 6 | 0.100 | 0.090 | 705 | 400 °C | $O_2$ $\alpha$-case |
| 7 | 0.020 | 0.020 | 490 | 500 °C | $O_2$ $\alpha$-case |
| 8 | 0.060 | 0.060 | 593 | 500 °C | $O_2$ $\alpha$-case |
| 9 | 0.100 | 0.100 | 603 | 500 °C | $O_2$ $\alpha$-case |
| 10 | 0.020 | 0.020 | 367 | 600 °C | $O_2$ $\alpha$-case |
| 11 | 0.060 | 0.060 | 423 | 600 °C | $O_2$ $\alpha$-case |
| 12 | 0.100 | 0.100 | 383 | 600 °C | $O_2$ $\alpha$-case |
| 37 | 0.150 | 0.150 | 433 | 600 °C | $O_2$ $\alpha$-case |
| 29 | 0.010 | 0.010 | 335 | RT | $O_2$ $\alpha$-case |
| 30 | 0.020 | 0.020 | 780 | RT | $O_2$ $\alpha$-case |
| 31 | 0.030 | 0.026 | 890 | RT | $O_2$ $\alpha$-case |
| 32 | 0.040 | 0.034 | 903 | RT | $O_2$ $\alpha$-case |
| 33 | 0.025 | 0.022 | 834 | RT | $O_2$ $\alpha$-case |
| 34 | 0.015 | 0.015 | 555 | RT | $O_2$ $\alpha$-case |
| 35 | 0.030 | 0.026 | 878 | RT | $O_2$ $\alpha$-case |
| 36 | 0.005 | 0.005 | 189 | RT | $O_2$ $\alpha$-case |
| 40 | 0.010 | 0.010 | 375 | RT | $N_2$ $\alpha$-case |
| 41 | 0.020 | 0.020 | 808 | RT | $N_2$ $\alpha$-case |
| 42 | 0.030 | 0.023 | 856 | RT | $N_2$ $\alpha$-case |
| 43 | 0.040 | 0.015 | 564 | RT | $N_2$ $\alpha$-case |
| 44 | 0.050 | 0.021 | 853 | RT | $N_2$ $\alpha$-case |
| 45 | 0.060 | 0.024 | 900 | RT | $N_2$ $\alpha$-case |
| 46 | 0.070 | 0.022 | 874 | RT | $N_2$ $\alpha$-case |
| 47 | 0.080 | 0.030 | 905 | RT | $N_2$ $\alpha$-case |
| 50 | Yield | 0.005 | 193 | RT | $N_2$ $\alpha$-case |
| 51 | Yield | 0.023 | 895 | RT | $N_2$ $\alpha$-case |
| 60 | Yield | 0.023 | 850 | RT | $N_2$ $\alpha$-case |

Table 3.2: Test matrix for interrupted tensile test specimens from Ti-6Al-4V unidirectional sheet material in the 0 ° direction. Tests were terminated at pre-set strains, rather than fracture, except when fracture occurred before this strain was reached (indicated in red). All tests above room temperature were conducted in an argon atmosphere.

| **Ti-6Al-4V UD 0 ° interrupted tensile test specimens** | | | | | |
|---|---|---|---|---|---|
| **Specimen** | **Target strain** | **Actual strain** | **Peak stress (MPa)** | **Temp** | **Condition** |
| 21 | 0.010 | 0.010 | 310 | RT | $O_2$ $\alpha$-case |
| 14 | 0.020 | 0.020 | 610 | RT | $O_2$ $\alpha$-case |
| 15 | 0.030 | 0.030 | 871 | RT | $O_2$ $\alpha$-case |
| 16 | 0.040 | 0.040 | 866 | RT | $O_2$ $\alpha$-case |
| 17 | 0.050 | 0.050 | 898 | RT | $O_2$ $\alpha$-case |
| 18 | 0.060 | 0.060 | 908 | RT | $O_2$ $\alpha$-case |
| 19 | 0.070 | 0.039 | 862 | RT | $O_2$ $\alpha$-case |
| 20 | 0.080 | 0.040 | 888 | RT | $O_2$ $\alpha$-case |
| 22 | 0.070 | 0.056 | 878 | RT | $O_2$ $\alpha$-case |
| 52 | 0.100 | 0.010 | 355 | RT | $N_2$ $\alpha$-case |
| 53 | 0.020 | 0.020 | 723 | RT | $N_2$ $\alpha$-case |
| 54 | 0.030 | 0.030 | 929 | RT | $N_2$ $\alpha$-case |
| 55 | 0.035 | 0.035 | 944 | RT | $N_2$ $\alpha$-case |
| 56 | 0.040 | 0.040 | 963 | RT | $N_2$ $\alpha$-case |
| 57 | 0.045 | 0.045 | 963 | RT | $N_2$ $\alpha$-case |
| 58 | 0.050 | 0.035 | 935 | RT | $N_2$ $\alpha$-case |
| 59 | 0.080 | 0.043 | 955 | RT | $N_2$ $\alpha$-case |

## 3.3 Crack detection and analysis techniques

Throughout the course of this study, detecting and accurately measuring the depth of any cracks present was a key priority. Several different techniques were tested with varying degrees of success, and these are summarised below.

### 3.3.1 Dye penetrant inspection (DPI)

DPI is one of the most commonly used non-destructive inspection techniques, and is often the preferred method for detecting surface-breaking cracks in materials. The size of the cracks generated in these tests were towards the lower limit of what can reliably be detected with DPI, however the benefits if it could be used successfully made it worth attempting. The primary aim was to allow cracks to be detected in-situ, and rapidly, so that the point of crack initiation could be identified without ending a test; instead it could be paused for a duration of a few minutes and then resumed after the DPI, which would affect the test results less than removing the sample for examination. However in practice, it was found that the technique did not have sufficient sensitivity; the crack dimensions were too small to allow detection with DPI, despite trialling various soak-times for the penetrant, none of the cracks could be detected.
A variation on DPI is FPI - fluorescent penetrant inspection. This is the same technique as visible dye DPI, but rather than the dye being red in colour, it fluoresces yellow when exposed to ultra-violet light, increasing the contrast between it and the developer. Different sensitivity levels are available, depending on the specific requirements of the application. This allows smaller cracks to be detected by eye than is possible with visible dye, increasing the effective resolution. This is a widely-used technique in industry, where there is frequently a need for repeatable and rapid non-destructive examination of materials, and specifications such as ASTM E1417 work to achieve this.
FPI was not used in this case, but it may provide a solution to the in-situ crack detection in future studies. Its usefulness may also be enhanced by further research into the detectability of cracks at more and higher levels of strain, as the greater degree of crack opening at higher strains has been shown to improve the success rate of DPI. [54]

### 3.3.2 Light optical and scanning electron microscopy

Microscopy techniques provide some of the most useful measures of $\alpha$-case thickness, although they are typically destructive, and like other methods, do not provide a definitive value for $\alpha$-case depth, but rather a value which depends on the particular measurement technique. This is discussed in more detail in Section 3.5.

### 3.3.3 Digital image correlation (DIC)

#### Introduction to DIC

In order to maximise the proportion of interrupted tensile tests which could provide useful data, attempts were made to identify the onset point of cracking with respect to strain. This information could then be utilised to determine the optimum strain range to target in the tensile testing, to capture all of the stages of crack development. The technique for detecting this point had to be non-destructive, else it would offer no benefit over the interrupted tensile testing which it was intended to aid, and ideally it would operate over the continuous range of the test, rather than at discrete points. DPI is an example of the latter, as to utilise it in this manner would involve pausing the test at various points to perform the inspection, and then the strains at which cracks were and weren't detected could be interpolated between. This is less precise than a method which continuously monitors the surface for the appearance of cracks, and as discussed in Section 3.3, DPI is also not well suited to the fine cracks generated in this study. The solution that was pursued was digital image correlation (DIC), a technique typically used for measurement of strain and strain distribution over the surface of a specimen, although it has been utilised successfully for crack growth analysis [55]. The principle is simple; a camera in a fixed position takes regular photographs of the test specimen, at a frequency appropriate to the test technique, which can vary from fractions of a Hz for creep testing, to MHz for ballistic studies. These images are then processed by the DIC software, which identifies many distinct groups of pixels, and tracks their positions from one image to the next, then based on this calculates the displacement and strain throughout the specimen. The methods used to measure the displacement and calculate the strain have been reviewed in detail by Pan et. al. [56], and will not be covered here. The software can utilise consecutively-captured images from any source, from SEM to telescopes, but for the purposes of this study only macro-scale optical images are considered. There are a number of off-the-shelf systems available for DIC, both two-dimensional, for in-plane deformation, and three-dimensional, which allow for out-of-plane deformation. For detecting the fine cracks that develop in $\alpha$-case, however, many of these systems lack the necessary resolution. A bespoke setup was therefore developed for this study, which would offer the optimum parameters for the application, with the additional aim of making the technique more accessible by utilising conventional equipment, rather than the specialised systems typically required.

#### Development of bespoke DIC setup

Central to the bespoke DIC system was the use of a conventional digital single lens reflex (DSLR) camera for image capture, rather than the dedicated

CCD (charge-coupled device) cameras typically utilised. The DSLR has a number of notable advantages over the CCD:

1. Resolution. CCDs used for DIC often have a sensor resolution of approximately 2500 x 2000 pixels, whereas the Nikon D7000 used in this study has a sensor resolution of 4928 x 3264 pixels, and other DSLRs are readily available with much greater resolutions, such as the Canon EOS 5DS with 8700 x 5800 pixels. Although the sensor resolution is only one of a number of factors which determine the minimum resolvable feature size, the increased resolution does allow for greater flexibility with regards to camera positioning and specimen geometry; it is often difficult to utilise a large proportion of the frame, and as such many pixels are "wasted". A thorough investigation of the importance of camera system resolution on DIC was conducted by Reu et al. [57].

2. Lens choice. As alluded to in point 1, to maximise the utilisation of the available sensor resolution, the region of interest on the specimen should ideally fill the frame. When dealing with a variety of specimen geometries and test rigs, this will necessitate the use of different lenses with a variety of focal lengths and magnifications. There are a wide range of lenses available for DSLRs, so the system can be optimised for every application.

3. Accessibility. Every research institution will have access to a DSLR, and the cost of even the most advanced models is small compared to that of a dedicated system, giving this setup a very low barrier to entry.

The DSLR is not without its disadvantages, however, and it is not being suggested as a better alternative to dedicated DIC camera setups in all scenarios. As with all techniques, the relative merits and shortfalls of each method should be considered for each application when selecting equipment. The main limitations of the DSLR setup are:

1. Frame rate. The maximum frame rate achievable by a DSLR camera is limited by the mechanical shutter, which allows for a maximum frame rate of approximately 10 Hz. To obtain higher frame rates, such as the kHz or MHz required by high strain rate systems, a specialised setup must be used. It is possible to increase the frame rate of a DSLR up to 60 Hz by operating in "video" mode, in which the shutter remains constantly open, but this also limits the available resolution.

2. Equipment lifespan. The rated life expectancy of a mechanical shutter in a DSLR is typically 150k to 300k cycles. For a system which will see sustained long-term usage, this may affect the economic viability.

3. Two-camera setups. If out-of-plane deformation occurs, then a two-camera setup is required for the three-dimensional DIC. The cameras must be synchronised, and this is likely to be challenging without a dedicated system.

For the applications relevant to this study, the DSLR setup offered the optimum balance of properties, and used the following hardware:

1. Nikon D7000 DSLR camera body. 23.6 mm x 15.6 mm sensor, with a maximum resolution of 4928 x 3264 pixels. Maximum framerate 6 Hz.
2. Sigma 105 mm f/2.8 macro lens.
3. SanDisk Extreme PRO SD memory card. 95 MB/s data transfer rate.
4. Slik Pro 400DX tripod.
5. Two 30 W mobile LED floodlights, 6000 K colour temperature.
6. Nikon MC-DC2 remote shutter release
7. VIC-2D DIC software. Open-source alternatives, such as Ncorr, are available.

The setup used for the initial development of the system is shown in Figure 3.5. The horizontal tensile test rig applied load to the specimen at a constant velocity, and this was used for refinement of the camera system, as well as providing the crack initiation point data as described in 3.3.3

**Frame rate measurement**

When utilising standard equipment for specialised applications, it is often necessary to perform additional calibration and measurement checks. In this instance, the consistency and accuracy of the frame rate setting had to be measured, so that the DIC could measure the strain rate with a known error and uncertainty. It was important that this did not require the use of specialised calibration equipment, in order to maintain the aim of keeping the setup accessible. Initially, a computer's stopwatch was trialled, which displayed elapsed time with thousandth of a second precision. The camera was set to five FPS, as this was the setting that would be used during most tests, and a number of images of the on-screen timer were captured. The time displayed in each image was manually entered into a spreadsheet, allowing the time between frames to be calculated.

However discrepancies were noticed with the times, and it became apparent that the refresh rate of the monitor, 50 Hz, was causing incorrect values to be displayed as the screen would refresh at a frequency 20 times lower than that of the numbers that the timer attempted to display on it. Due to

Figure 3.5: Early experimental setup used for refining the DIC camera system, and obtaining initial results on crack initiation points.

the way the timer refreshed, with the tenths, hundredths and thousandths of a second not updating simultaneously when they changed, it was decided that the method was fundamentally flawed and not worth pursuing.

All similar methods utilising digital displays possessed this same flaw, which could only be resolved by using a display with a significantly higher refresh rate. However a simpler solution was to find an analogue method, which would be inherently more suitable for the task. This was achieved by printing a paper disc graduated with 0.5° lines, which was attached to the platen of a Buehler Phoenix polishing machine. A fixed pointer was positioned to the side of machine, overlapping the edge, and the camera mounted on a tripod facing vertically downwards, directly above the pointer to minimise parallax error.

The platen speed was set to a nominal 125 RPM. To measure the actual speed, a red mark was drawn on the graduated disc, and the machine was run whilst being filmed by the camera at 25 FPS. Precisely one minute of this recording was then played back, and the number of times that the red marker passed the fixed pointer was recorded, confirming that the disc was rotating at 125 (+/- 0.5) RPM. The inertia of the platen, on account of its substantial rotating mass, minimised the risk of minor fluctuations in the rotational velocity.

The frame time of the camera could now be measured by simply running the machine at 125 RPM, and taking a large number (c. 100) of images at the desired FPS. The position of the pointer on the graduated disc (Figure 3.6) was then manually recorded from each image, which allowed the degrees

of rotation, and hence time between frames, to be calculated.

With the camera set to five FPS, the time between frames was measured between 0.199 and 0.201 seconds, a variation of 0.5 %. The measurement error was minimal; with the pointer position being recorded with 0.5 precision, and the disc rotating 750 degrees per second, the error was approximately 0.0007 %.

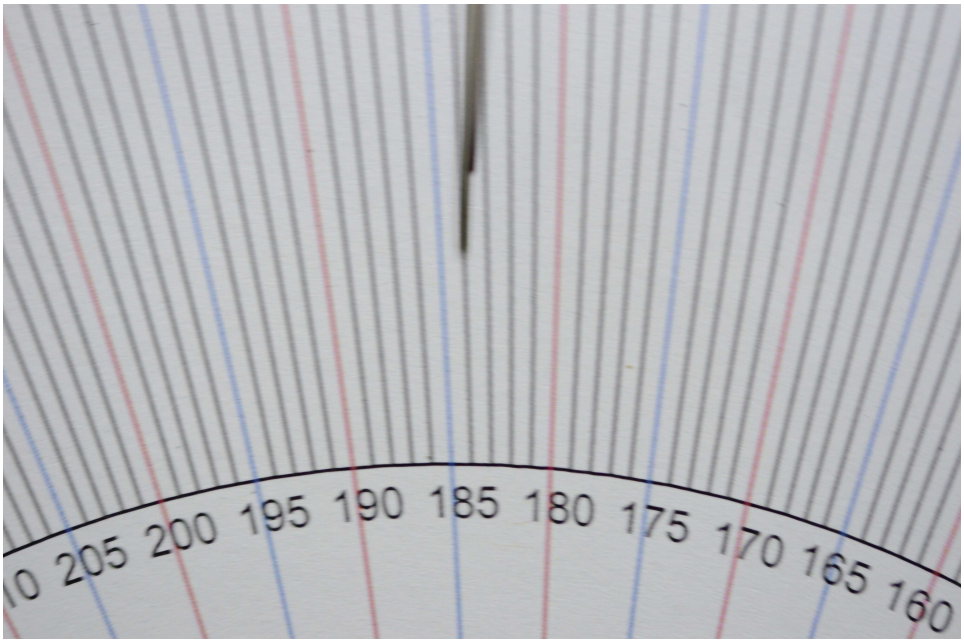


Figure 3.6: Image used for measuring the frame rate of the Nikon D7000 camera, by recording the degrees of rotation per frame of a platen rotating at 125 RPM

### Speckle pattern

The DIC technique requires distinctive features on the surface of the sample in order for the software to be able to track the movement. This is typically achieved by painting the surface with a random black and white speckle pattern. Several variations of speckling technique were trialled, leading to a refinement of the method to make it suitable for this purpose: The conventional method that is typically used to apply a speckle pattern to a sample, involves first spraying the gauge length with a coat of white primer paint from an aerosol can, to create a solid white background to provide contrast. Once this has dried, an aerosol of matte black paint is used to create a speckle pattern over the white paint, by using only light pressure on the trigger, causing it to sputter. An example of a sample speckled in this way is shown in Figure 3.7. There are two limitations with this method. The

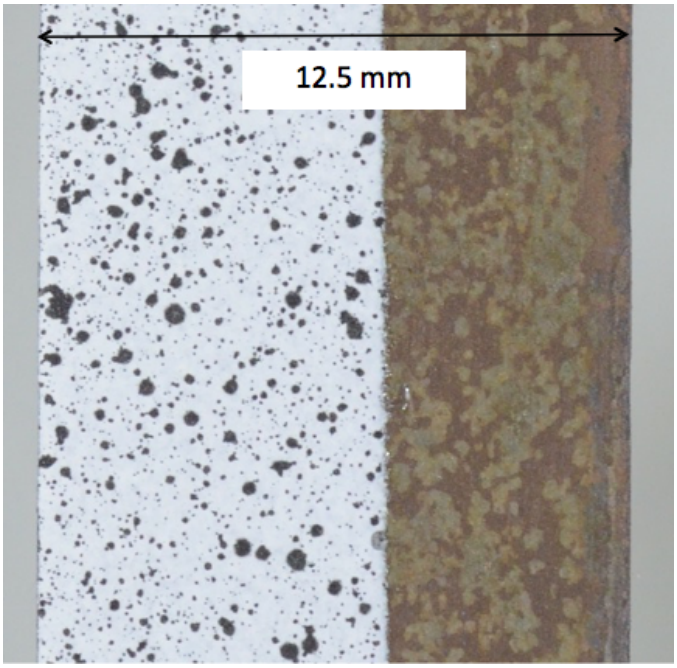


Figure 3.7: An example of the typical DIC black and white speckle contrast paint applied to a flat tensile specimen. The right hand side of the specimen exhibits patches of spalled oxide following thermal exposure, which do not offer sufficient contrast for DIC.

first is one of resolution; there are large white spaces uninhabited by any black speckles, and also some large black speckles. DIC relies on being able to uniquely identify individual regions, known as subsets, as shown in Figure 3.8, and the software tracks the movement and distortion of these. In order for the subsets to be reliably identified in each image, they must contain pixels with a variety of different greyscale values, ideally changing according to a smooth gradient, as would be the case around a black speckle on a white background. In a largely white or black area however, although there may be the occasional pixel of a different colour, there is rarely the smooth transition, and typically the software struggles to identify these regions.

This requires the subset to be sufficiently large to ensure that every one contains at least one speckle, and some contrasting white background. In the case of Figure 3.7, there are white regions of up to 30 pixels square, so the subset size must be greater than this to obtain adequate indexing. At this scale, 30 pixels equates to almost 0.5 mm, so this subset size severely limits the resolution of the DIC. The second issue relates to the paint. Although primer is designed to adhere well to a metallic substrate, it also bonds strongly to itself, creating a complete layer over the surface of the sample. This naturally introduces some uncertainty into the results; the

Figure 3.8: Diagram illustrating a subset as used for DIC. Each square represents a pixel, and the numbers represent grey values of each pixel.

images taken are all of the paint, not the substrate, so the DIC is actually measuring the deformation of the paint, not the sample. It is not known whether the two are behaving identically or independently, or a combination of the two. The assumption has to be that the paint is following the movement of the sample, and this does seem to be a reasonable assumption when dealing with strain on a macro scale.

However when operating on a finer scale, and especially when surface cracking is involved, the evidence suggests that this method is not suitable. There are two problems that can occur; the first, illustrated in Figure 3.9, is that the paint can crack independently of the sample, giving misleading results which may appear to display the expected behaviour, but are actually unrelated to the sample. The second issue, shown in Figure 3.10, is that the sample can form cracks, but these do not transfer to the paint, and therefore cannot be detected by DIC. To address the problems with the conventional method, two novel adaptations were made:

1. Speckle density. In order to eliminate the large white and black regions present in the conventional speckle, the black paint was sprayed through a fine (150 $\mu$m) stainless steel mesh, housed in an aluminium jig designed to fit over the sample. This resulted in a greatly refined speckle pattern, allowing for a significant improvement in DIC resolu-

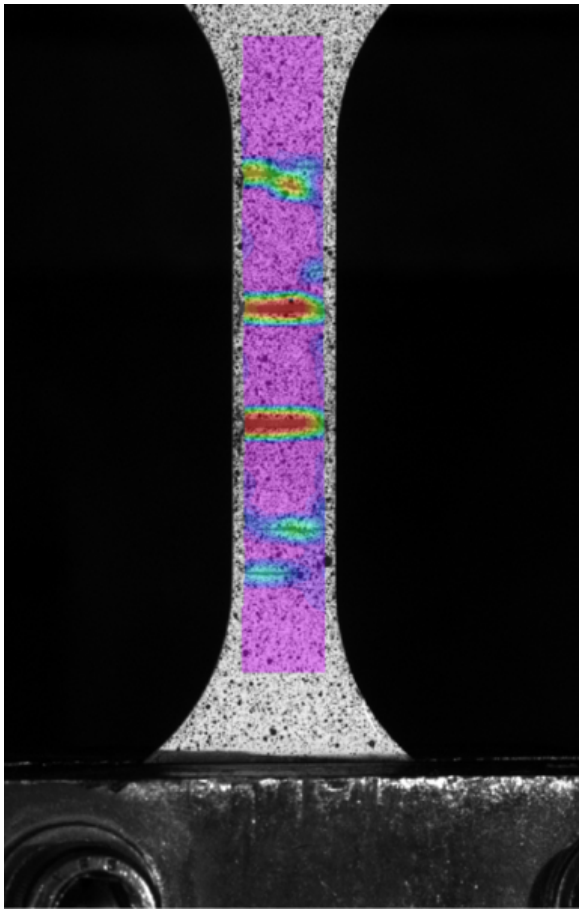

Figure 3.9: DIC overlay on a tensile test specimen. The colours indicate strain, with the highest strain areas shown in red. These red regions suggest cracking in the specimen, but destructive evaluation revealed that only the paint cracked at these points, not the metallic substrate

tion (Figure 3.11).

2. Paint layer behaviour. The white primer used as a basecoat was switched for a developer spray normally used for dye penetrant inspection. The application method is similar to that for paint, however the developer consists of white powder suspended in solvent, which does not form a strongly bonded layer over the surface of the sample. This allowed it to match the motion of the substrate far better, and the surface cracks on the substrate were transmitted through to the surface of the developer layer. Some of the finer cracks may still be bridged, but the majority are visible, as demonstrated by the DIC image in Figure 3.12.

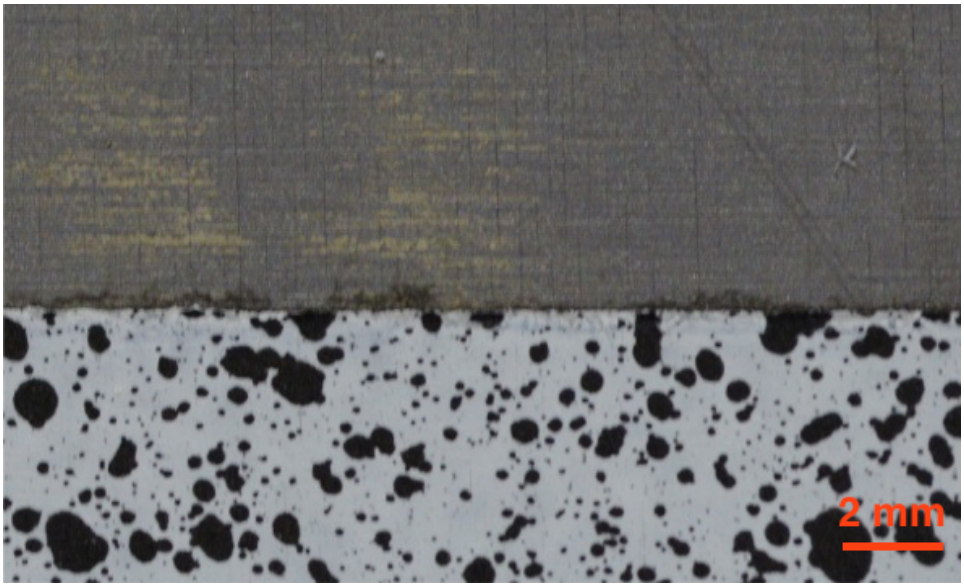


Figure 3.10: Specimen post-tensile testing, with speckle pattern only applied to one half of the gauge length. Cracks are visible in the metallic substrate at the top of the image, but these were not transferred to the paint in the lower half of the image.

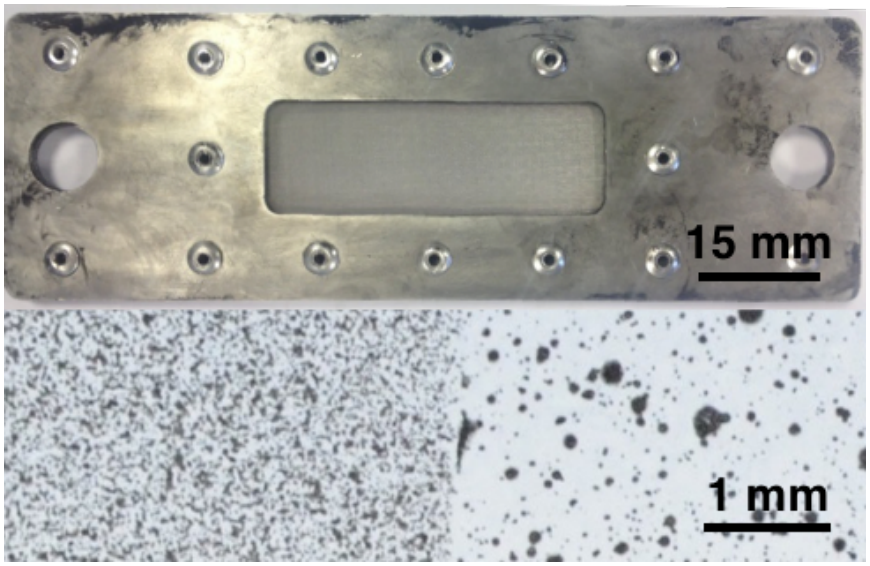


Figure 3.11: Top: Jig used for creating fine speckle on specimens, by forcing the paint through a stainless steel mesh with 150 $\mu$m aperture. Bottom left: Speckle pattern created using jig. Bottom right: Standard speckle pattern at the same scale, for comparison.

### Application of DIC

It was established early on that DIC would not provide sufficient information for crack growth analysis, due to it only being possible to record the surface opening of the cracks, and with resolution which was orders of magnitude too low to accurately measure dimensions of the cracks. However as a complimentary technique to subsequent destructive analysis of the specimens it was useful, as it alllowed crack initiation to be identified retrospectively without interrupting the tests, which otherwise would not have been possible. The microscopic examination of the specimens then allowed thorough evaluation of the cracks.

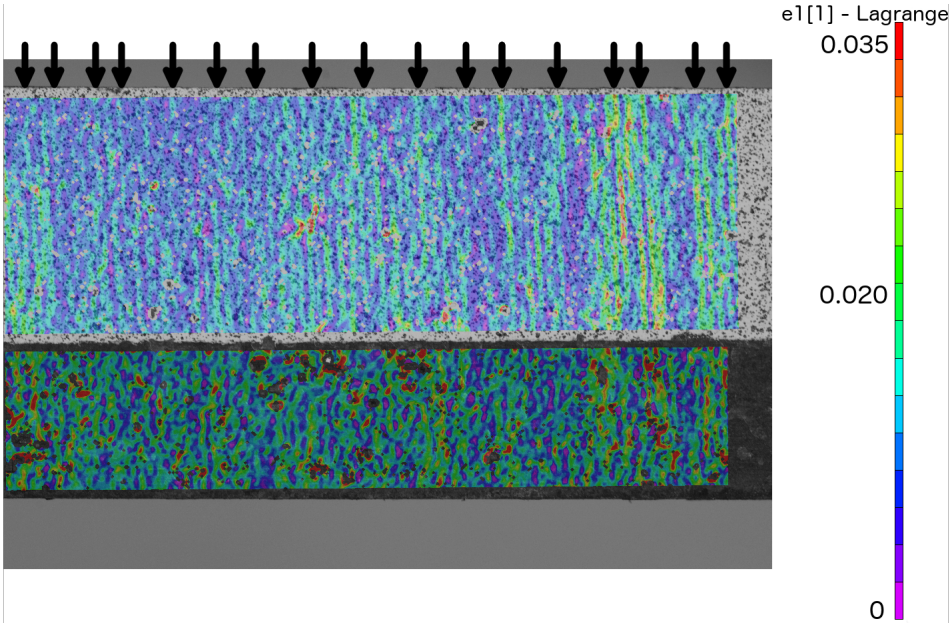


Figure 3.12: DIC overlay of specimen during tensile testing. The top section of the specimen has developer "paint" and the fine mesh speckle applied, whilst the lower section retains the as-thermally exposed surface. The arrows indicate some of the cracks identified from the DIC, which were subsequently confirmed with destructive evaluation.

During the planning of the interrupted tensile testing, introduced in Subsection 3.2.4, it was necessary to pre-determine the range of strain values that would be required to effectively cover the full range of crack initiation and growth; there was little value in producing multiple specimens which were terminated at the pre-initiation stage, thereby reducing the number of specimens exhibiting the crack growth phases. The DIC was valuable for this purpose, as it indicated that at room temperature, cracks would not begin to form in $\alpha$-case at strain levels of $<0.010$, so this was a suitable starting point

to include the complete range of crack development. It was subsequently utilised during the interrupted tensile testing to attempt to identify the strain at which each crack had initiated, which proved to require greater resolution than was available. However it did allow the general pattern of crack formation to be identified, including the multiple arrays as discussed in Section 3.5.2, which the DIC sequences showed formed consecutively as groups.

## 3.4 Results and discussion

### 3.4.1 Warm tensile testing

The tensile tests conducted at moderate temperatures, the details of which are shown in Table 3.3, were analysed by a number of methods after testing. The stress/strain curves recorded during the test were normalised by removing the data points at a load of <100 N, as a form of retrospective preload to eliminate slack in the system, as described in Section 3.2.3. This was necessary in order to obtain accurate strain figures, since the subtle differences in initial tooling position could result in a variation in displacement of several millimetres between samples, which with a gauge length of 25 mm and actual strain-to-failures of the order of 0.1 - 0.2, resulted in substantial errors, far greater than those incurred from this slightly crude "retrospective preload" technique, as can be seen in Figure 3.13. The correction was applied as follows:

1. The raw load/displacement data was collected from the tensile testing machine.
2. The first point at which the load exceeded 100 N was identified, but the load value was not changed since all the load was transmitted through the specimen.
3. The displacement value associated with this point was subtracted from itself, and every subsequent displacement data point, to set the new zero position.
4. Stress and strain values were calculated from this corrected data, using the original specimen dimensions.

The normalised stress/strain curves are shown in Figure 3.14. These provide valuable insight in to the mechanisms operating at each of the test temperatures, and are useful for interpretation of the results obtained from fractography and microscopy.

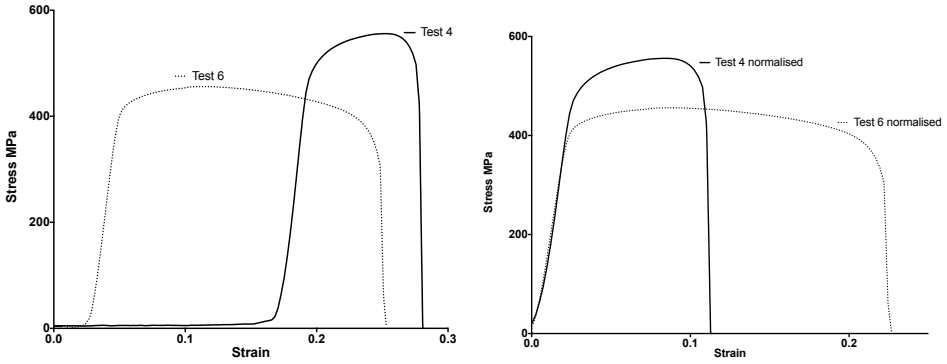


(a) Stress/strain curve before normalisation (b) Stress/strain curve after normalisation.

Figure 3.13: Stress strain curves for two tensile specimens before (a) and after (b) normalisation, as described in Section 3.4.1. The process eliminates the effects of the variable slack in the tooling to provide comparable data.

Table 3.3: Test matrix for warm tensile tests of Ti-6Al-4V sheet material with differing crystallographic textures, on account of the rolling technique used to produce them. All specimens were exposed to an oxygen-containing atmosphere at 920℃ prior to testing, as per Section 2.2.1. Tests were continued until fracture, and all were conducted in an argon atmosphere.

| **Specimen** | **Strain rate** ($s^{-1}$) | **Temp** | **Material** | **Failure strain** | **Peak stress (MPa)** |
|---|---|---|---|---|---|
| S2-13 | 0.02 | 300℃ | Membrane | 0.123 | 795 |
| S2-14 | 0.02 | 400℃ | Membrane | 0.132 | 764 |
| S2-15 | 0.02 | 500℃ | Membrane | 0.139 | 691 |
| S2-16 | 0.02 | 600℃ | Membrane | 0.214 | 527 |
| S2-17 | 0.02 | 300℃ | UD 0° plate | 0.100 | 858 |
| S2-18 | 0.02 | 400℃ | UD 0° plate | 0.094 | 642 |
| S2-19 | 0.02 | 500℃ | UD 0° plate | 0.139 | 669 |
| S2-20 | 0.02 | 600℃ | UD 0° plate | 0.150 | 536 |
| S2-21 | 0.02 | 300℃ | XR plate | 0.127 | 795 |
| S2-22 | 0.02 | 400℃ | XR plate | 0.119 | 667 |
| S2-23 | 0.02 | 500℃ | XR plate | 0.091 | 698 |
| S2-24 | 0.02 | 600℃ | XR plate | 0.197 | 518 |

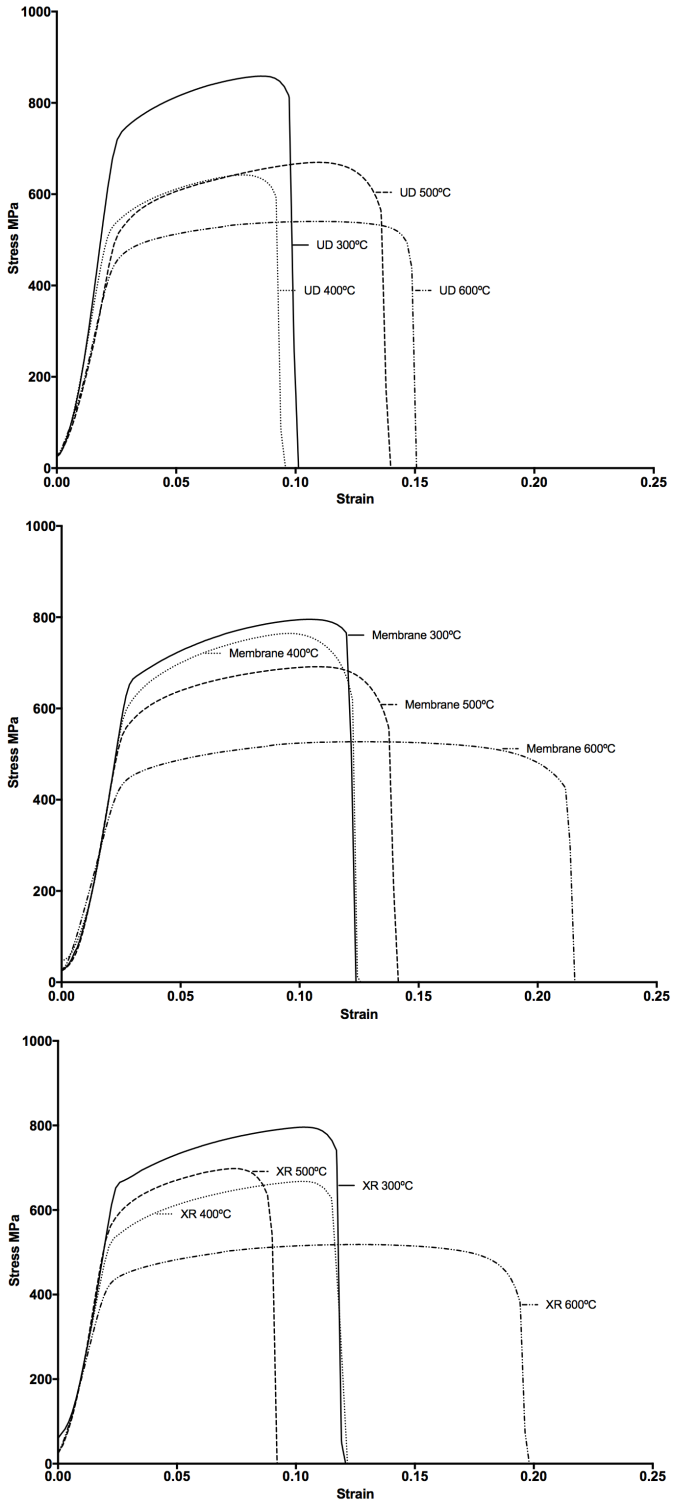


Figure 3.14: Stress/strain curves comparing the tensile behaviour of Ti-6Al-4V plates and sheet with oxygen-stabilised $\alpha$-case, when tested at temperatures from 300°C - 600°C. Top - UD plate, centre - membrane sheet, bottom - XR plate.

All of the specimens tested in this section were taken to failure, and as such all of the fracture faces were available for examination, which has proven to be one of the best techniques for identifying $\alpha$-case, as discussed in Section 3.5. This is particularly relevant in this instance, where identical specimens were being tested at different temperatures and displaying different results, because it highlights the distinction between measured $\alpha$-case and effective $\alpha$-case. The former can be obtained at room temperature, by techniques such as microscopy, hardness profiling or chemical analysis, whereas the latter will differ depending on operational temperature and crystallographic texture. With sufficient empirical data it should be possible to infer the effective $\alpha$-case depth from this, which is the far more useful measure for practical applications.

Fracture faces were examined in an FEI InspectF FEG-SEM, using secondary electron imaging with an accelerating voltage of 20 kV. Fractographs for the uni-directionally rolled plate specimens are shown in Figures 3.15 - 3.17, which correspond to the top stress/strain curves in Figure 3.14. There was a step-change in fracture appearance between the specimen tested at 300℃ (Figure 3.15) and the one tested at 500℃ (Figure 3.16). The lower temperature specimen exhibited a fracture appearance comparable to room temperature tests, such as that shown in Figure 3.18. The key similarities are the presence of well-defined facets in the near-surface region, some with visible slip banding, transitioning to dimpling towards the bulk, characteristic of microvoid coalescence. Some dimples in the transition region also exhibit slip lines, with the occurrence of such features decreasing further from the surface.

The 500℃ specimen differed in two respects; firstly, the dimpled region of the fracture face began approximately 20 $\mu$m below the surface, compared to approximately 150 $\mu$m in the 300℃ specimen. Secondly, there was no highly faceted area near the surface; the immediate sub-surface region displayed visible slip lines, but did not show evidence of cleavage fracture. The 600℃ specimen, shown in Figure 3.17, exhibited a similar 20 $\mu$m depth of material displaying slip lines prior to the dimpled region, although the steps on the grain faces were more prominent than in the 500℃ specimen. There were also possible indications of cleavage fracture in the initial 10 $\mu$m below the surface, although these were less defined than in the lower temperature specimens.

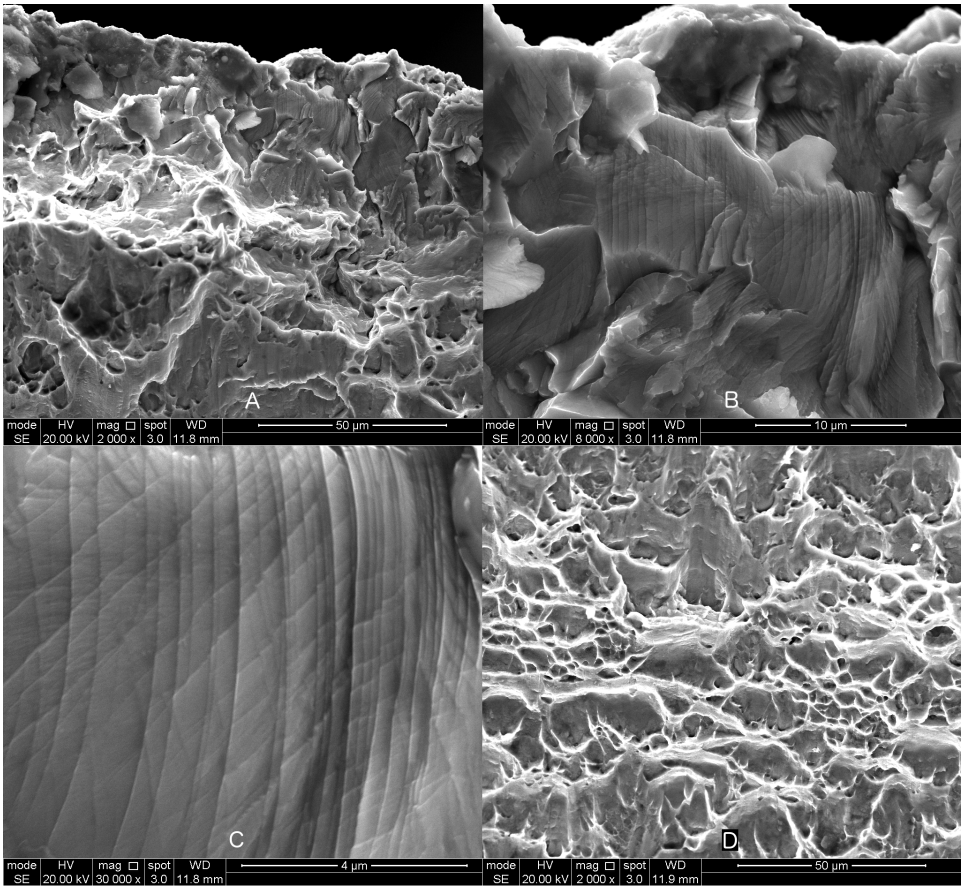


Figure 3.15: Secondary electron fractographs of unidirectionally rolled plate with an $O_2$-stabilised $\alpha$-case, monotonically tensile tested in the 0° direction at 300℃. A) Overview of region from surface towards bulk, showing a portion of the transition from cleavage fracture and slip to microvoid coalescence. B) Surface region showing distinct slip features directly below the surface, with only a small proportion of cleavage fracture visible. C) Magnified area of (B) highlighting the slip bands. D) Fully ductile region approximately 200 $\mu$m below the surface, exhibiting only microvoid coalescence.

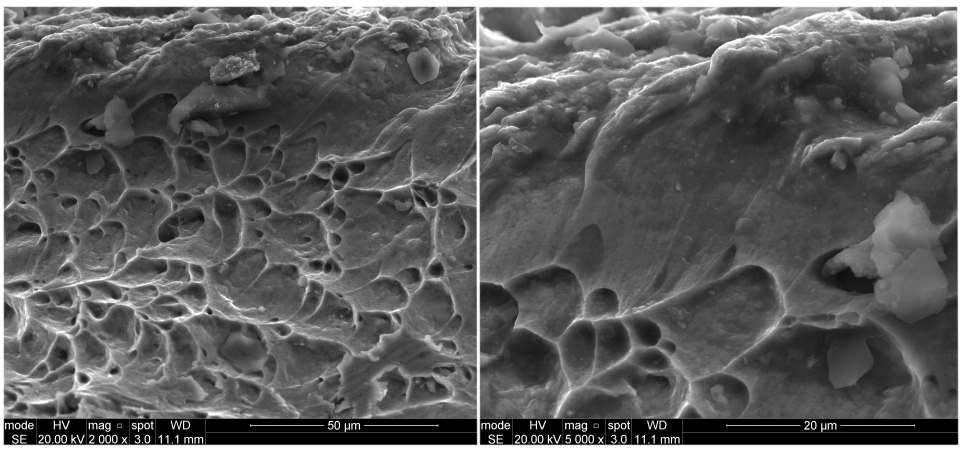


Figure 3.16: Secondary electron fractographs of unidirectionally rolled plate with an $O_2$-stabilised $\alpha$-case, monotonically tensile tested in the 0° direction at 500℃. Left: Overview from surface to bulk, showing the transition between slip to microvoid coalescence within the first 20 $\mu$m sub-surface. Right: Magnified surface region showing the slip bands in the initial 20 $\mu$m below the surface, and the transition to microvoid coalescence beyond this. The slip bands are less pronounced than in the higher test temperature specimen shown in Figure 3.17, which is thought to be due to different grain orientations in these two regions.

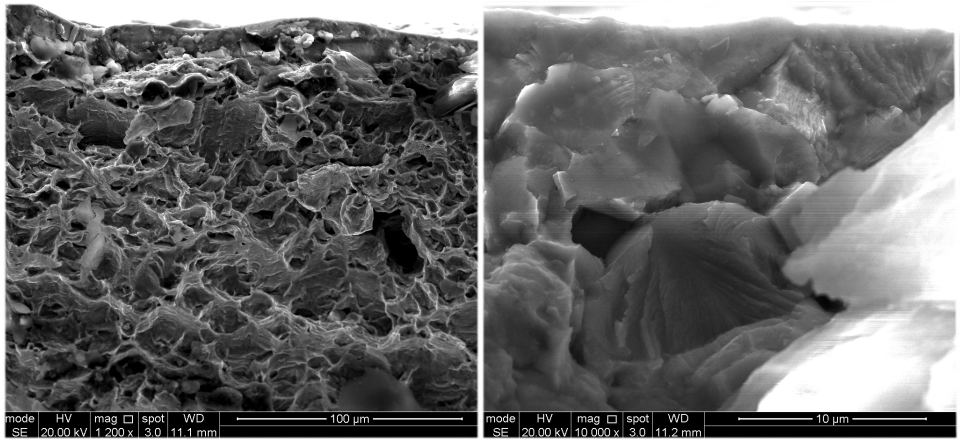


Figure 3.17: Secondary electron fractographs of unidirectionally rolled plate with an $O_2$-stabilised $\alpha$-case, monotonically tensile tested in the 0° direction at 600℃. Left: Overview from surface to bulk, showing the transition from slip to microvoid coalescence within the first 20 $\mu$m sub-surface. Right: Magnified area of the surface region from the top right of the LH image, showing the slip bands in the intital 20 $\mu$m, with possible cleavage fracture visible in the initial 10 $\mu$m sub-surface.

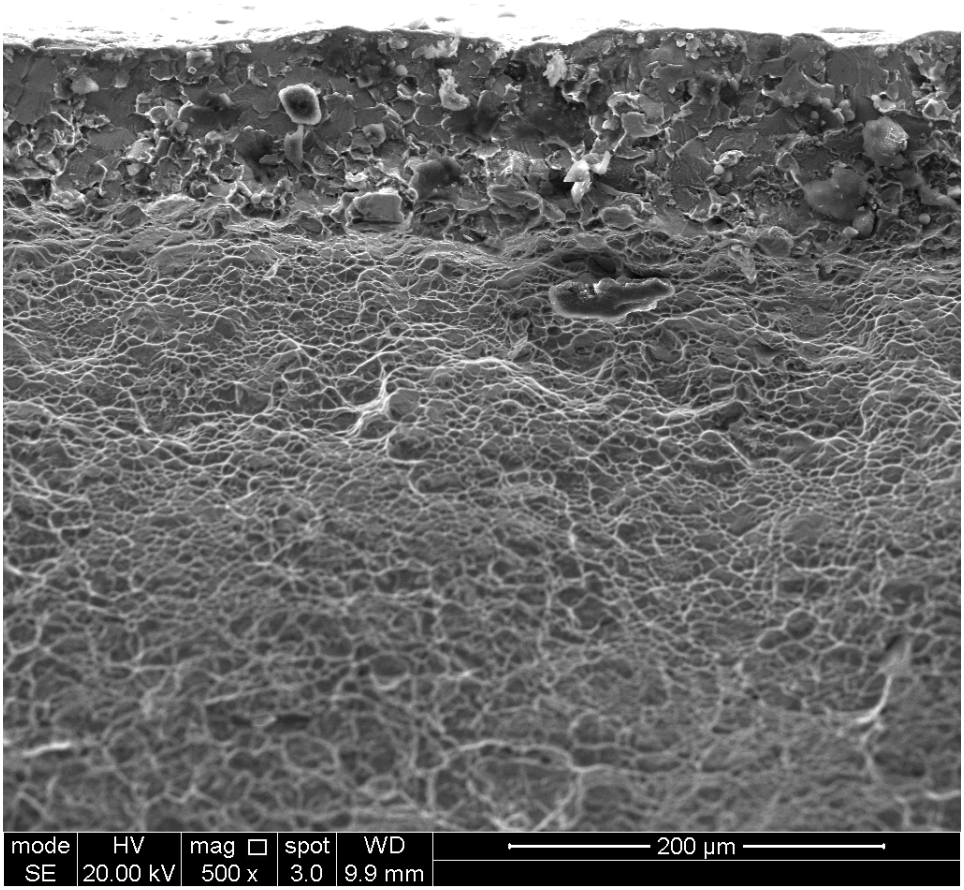


Figure 3.18: Secondary electron fractographs of unidirectionally rolled plate with an $O_2$-stabilised $\alpha$-case, monotonically tensile tested in the 0° direction at room temperature. The fracture features are similar to those seen in the specimens tested at 300℃ and 400℃, shown in Figure 3.15.

The cross-rolled (XR) specimens' fractographs are shown in Figures 3.19 and 3.20, which equate with the stress/strain curve in Figure 3.14. The specimens tested at 400℃, 500℃ and 600℃ had broadly similar fracture appearances, consisting solely of dimples suggesting microvoid coalescence, with the slight exception of the 400℃ specimen, which had a minor region of faceted fracture in the first 20 $\mu$m below the surface. The 400℃ specimen also displayed distinct changes in crack path direction at 40 $\mu$m- 50 $\mu$m beneath the surface; a feature it had in common with the 300℃ specimen, in Figure 3.20. This latter specimen had pronounced slip lines visible in the first 30 $\mu$m below the surface, which were not seen in cross-rolled material tested at any higher temperatures, suggesting a possible change in mechanism between 300℃ and 400℃. This is a lower temperature threshold than for the unidirectionally rolled material, which implies that the mechanisms are sensitive to crystallographic texture, and an increased number of test specimens may be expected to reveal a similar range of transition temperatures for both material types, depending on local texture at the point of fracture in each specimen.

The membrane specimens' fracture faces in Figures 3.21, 3.22 and 3.23 relate to the stress/strain curve in Figure 3.14. The 300℃ specimen in Figure 3.21 diplayed a range of fracture features similar to specimens tested at room temperature, with distinct regions of cleavage fracture, various forms of slip bands, and microvoid coalescence visible in the initial 60 $\mu$m below the surface. The slip lines on facets were more prominent than other test conditions, which was perhaps related to the grain orientations present in the membrane material near-surface.

The higher temperature membrane specimens, such as the one tested at 600℃ in Figure 3.22, exhibited cleavage fracture and slip lines in the first 10 $\mu$m below the surface, similarly to the uni-directionally rolled plate at 600℃, but contrary to the cross-rolled plate at the same temperature.

The 500℃ membrane specimen in Figure 3.23 displayed only dimpling on the fracture face, which did not appear to follow the temperature dependance of fracture mechanism seen in other specimens. Examination of a secondary crack on the surface, however, which did not proceed to fracture, revealed similar cleavage fracture and slip banding to that seen in the 600℃ specimen.

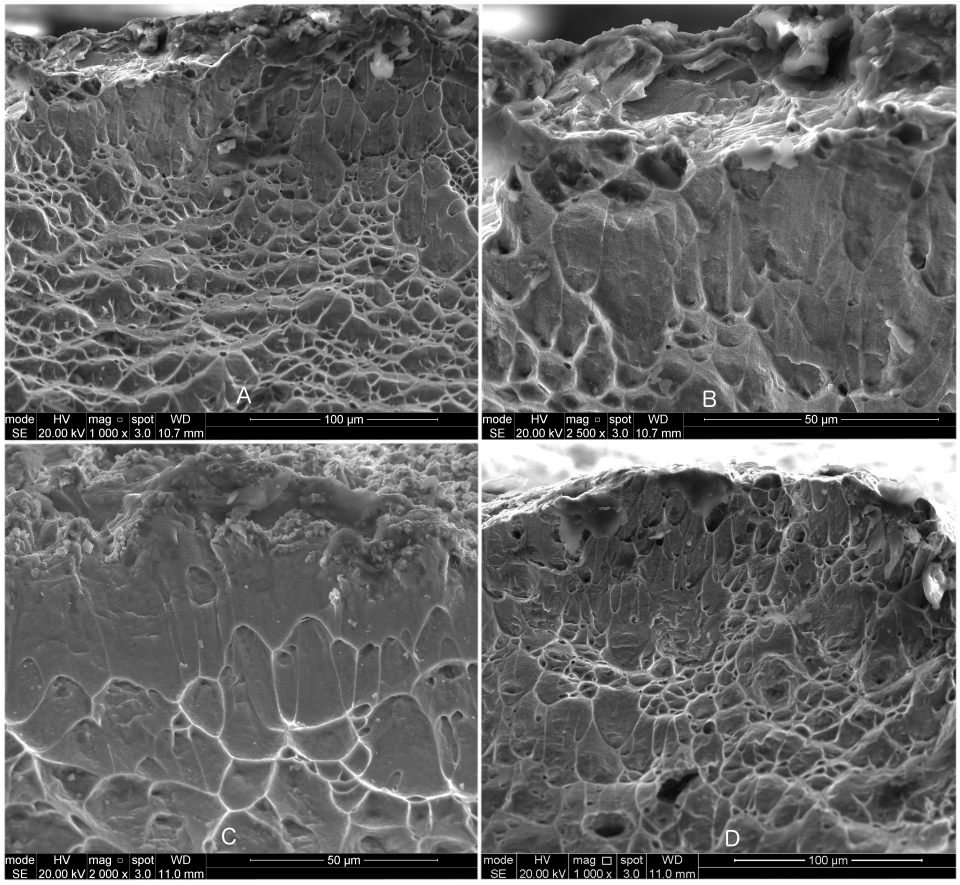


Figure 3.19: Secondary electron fractographs of cross-rolled plate with an $O_2$-stabilised $\alpha$-case, monotonically tensile tested at elevated temperature. A) Specimen tested at 400℃, exhibiting mainly dimpled fracture appearance, suggesting microvoid coalescence, but with a small region of more faceted fracture immediately sub-surface. B) Sub-surface from (A) showing slightly faceted region at higher magnification. C) Specimen tested at 500℃, showing only dimpled fracture appearance. D) Specimen tested at 600℃, also showing only dimpled fracture appearance.

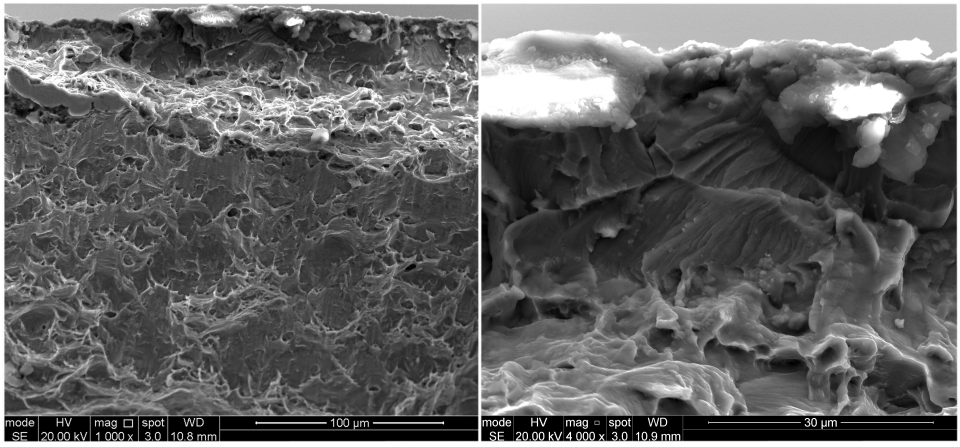


Figure 3.20: Secondary electron fractographs of cross-rolled plate with an $O_2$-stabilised $\alpha$-case, monotonically tensile tested at 300℃. A) Overview showing primarily dimpled fracture appearance, but with the first 30 $\mu$m below the surface region exhibiting distinct slip lines, shown in higher magnification in (B). There are two substantial changes in direction of the crack path, first at approximately 30 $\mu$m below the surface, and again at approximately 40 $\mu$m - 80 $\mu$m from the surface. These are likely to be linked to the banded texture of XR plate.

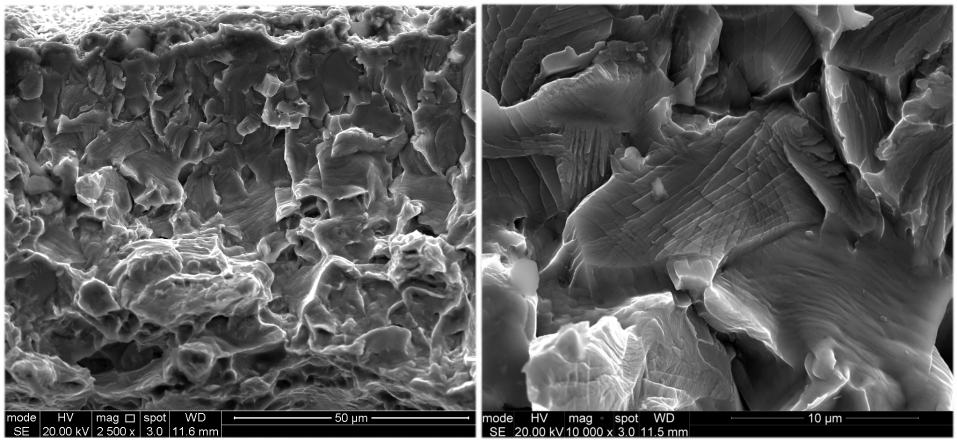


Figure 3.21: Secondary electron fractographs of membrane sheet with an $O_2$-stabilised $\alpha$-case, monotonically tensile tested at 300℃. Left - Overview showing the full range of fracture features: Cleavage fracture in the first 5 $\mu$m beneath the surface, distinct slip bands from 5 $\mu$m - 30 $\mu$m, transitioning to primarily wavy slip from 30$\mu$m - 50 $\mu$m, and microvoid coalescence dimpling from 50 $\mu$m onwards. Right - Higher magnification image of different slip line morphology in adjacent grains.

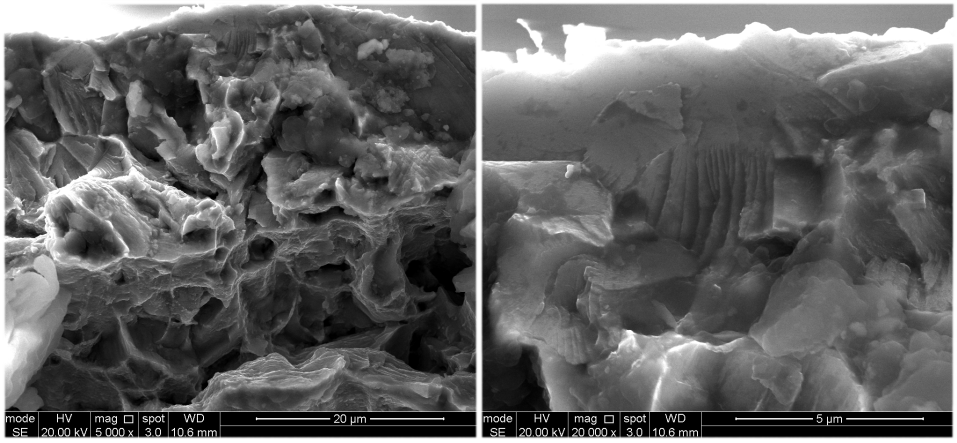


Figure 3.22: Secondary electron fractographs of membrane sheet with an $O_2$-stabilised $\alpha$-case, monotonically tensile tested at 600℃. Left - Overview showing three distinct regions of the fracture: cleavage fracture from 2 $\mu$m - 3 $\mu$m below the surface, slip lines from 3 $\mu$m -18 $\mu$m, and microvoid coalescence from 18 $\mu$m to the bulk. There is significant overlap in these ranges between samples, highlighting the influence of individual grain orientation on the local fracture mechanism. Right - Higher magnification image of the surface region showing cleavage fracture and slip lines, with possible evidence of wavy slip also visible in the right hand side of the image.

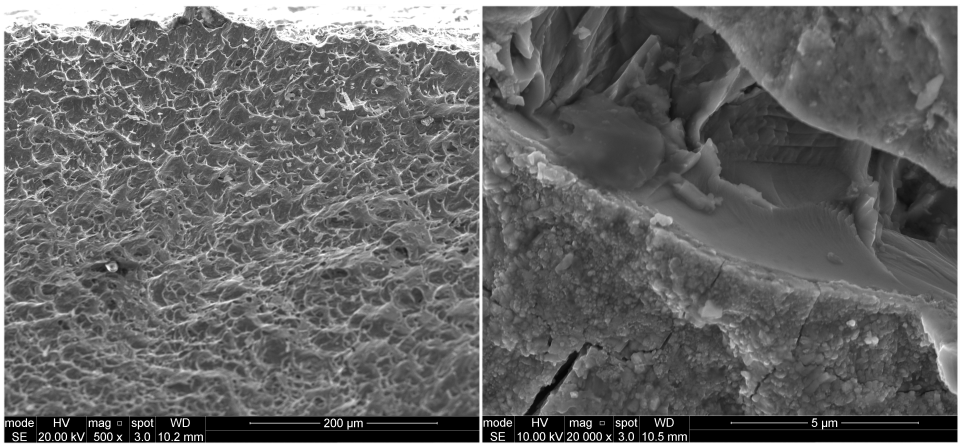


Figure 3.23: Secondary electron fractographs of membrane sheet with an $O_2$-stabilised $\alpha$-case, monotonically tensile tested at 500℃. Left - overview of fracture face, showing only microvoid coalescence dimpling. Right - View from specimen surface, looking into a crack which did not progress to failure. This crack exhibits cleavage fracture and slip lines, which were not evident in the primary crack.

The results presented in this section show pronounced differences between test temperatures, and material type. Analysis of the stress/strain curves in Figure 3.14 suggested a defined temperature for each specimen type (UD, XR or membrane) at which the fracture mechanism changed. This was identified by the large increase in strain-to-failure; a gradual increase in strain would be expected with increasing temperature for a given fracture mechanism, but for a step-change to occur, a change in mechanism would be required. Examination of the fracture faces revealed a more complex system than a simple change from one fracture mechanism to another, with at least three different regions occurring within a single fracture face, such as in Figure 3.21, suggesting that multiple fracture mechanisms were operating simultaneously or consecutively within a specimen.
The greatest number of different fracture mechanisms occurred in the lowest temperature (300℃) specimens, and with increasing temperature certain mechanisms ceased. There were no fracture features identified on the higher temperature specimens which were not also observed on the lower temperature ones. This indicates that, strictly speaking, a change in fracture mechanism was not the cause for the step-change in strain to failure, but instead it was the cessation of one of the several operating mechanisms which allowed an increase in strain.
However it appears that a particular mechanism may not need to completely deactivate in order to effect the step-change; Figure 3.22 for example, shows a specimen tested at 600℃ which clearly exhibits cleavage fracture, slip banding and microvoid coalescence. The former two mechanisms are thought to be the primary cause of the low ductility in $\alpha$-case, which are often not observed at these higher test temperatures, however it can be seen from Figure 3.14 that this specimen failed at a significantly higher strain than the specimens tested at lower temperatures. This indicates that either the operational depth from the surface of one or more of the fracture mechanisms reduced sufficiently to greatly diminish its effect on the overall strain to failure, or that the higher temperature altered the transition between mechanisms. An example of the latter would be between the initial cleavage fracture region, and the subsequent section of slip. As the temperature increased, the value of $K_{IC}$ at the crack tip may have increased sufficiently to prevent further growth by cleavage fracture, until sufficient slip had accrued to allow fracture. This "delay" in crack propagation would have manifested itself as an increase in failure strain.

A schematic of a cross section of material with $\alpha$-case, indicating the behaviour of cracks at various temperatures is shown in Figure 3.24. The most highly oxygen-enriched, $\beta$-depleted region immediately below the oxide layer will fracture in a faceted manner at all temperatures, although the depth of this mechanism will decrease with increasing temperature. As the oxygen level gradually decreases towards the bulk, a greater degree of slip is incorporated into the faceted crack growth, before eventually the crack no

longer proceeds in a brittle manner, and microvoid coalescence takes over. This marks the point of the end of the effective $\alpha$-case, and differs according to temperature.

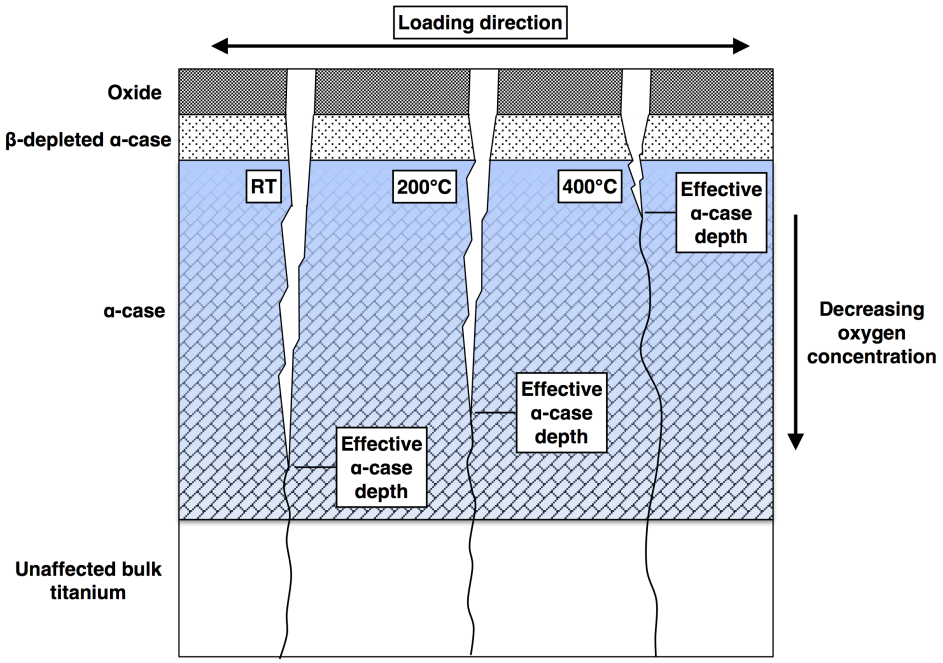


Figure 3.24: Schematic of a cross section of material with $\alpha$-case, indicating some of the differences that temperature has on crack growth, and how the effective $\alpha$-case depth changes with temperature.

The substantial increase in strain-to-failure that occurs in the XR and membrane specimens between 500℃ and 600℃, which does not occur in the UD specimen, is an important observation, as this substantiates the theory that $\alpha$-case ceases to behave in a brittle manner above 500℃. The crystallographic orientation relative to the crack propagation direction has an influence on the ductility of each grain, and in XR and membrane material, there are a greater range of grain orientations present than in the UD material.
At 500℃, only grains oriented within a narrow range of angles remain favourable for fracture, with the majority of grain orientations arresting the crack growth, and instead promoting failure in a ductile manner. In UD material, tested in the longitudinal direction, very few grains would have been oriented to favour brittle fracture, and so the crack growth stopped, with the corresponding overall increase in strain-to-failure. In the XR and membrane material, however, a greater number of variants would be present, and therefore the cracks would have continued to propagate along the brittle

direction, in a similar manner to at lower temperatures, leading to comparable strain-to-failure.
At 600℃, none of the grain orientations in the $\alpha$-case were brittle, and so failure strain of the XR and membrane material dramatically increased. This same transformation occurred in the UD material between 400℃ and 500℃, and only a minor increase was seen above this temperature. This suggests that $\alpha$-case becomes noticeably less brittle between 400℃ and 500℃, and ceases to be brittle at all between 500℃ and 600℃.
Figure 3.25 suggests a theoretical relationship between the temperature and critical grain orientation required for brittle fracture to occur, at a given elevated oxygen level, such as that present in the samples in this study at a depth of approximately 15 $\mu$m below the surface. A strongly textured material would be expected to show the step in failure strain at different temperatures, depending on the direction in which it was tested, with the temperature being lower when the majority of grains were oriented with the basal plane parallel to the surface, than when perpendicular.

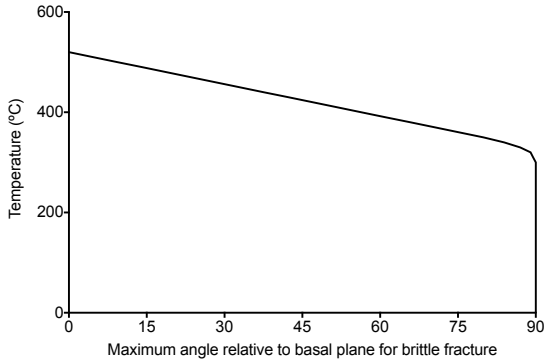


Figure 3.25: Proposed theoretical relationship between temperature, and the critical grain orientation (relative to crack propagation direction) required for brittle fracture to occur, at a given elevated oxygen concentration. Where a wide variety of grain orientations are present, or many grains have their basal plane approximately perpendicular to the surface, brittle fracture is likely to occur at higher temperatures than in material with the majority of grains' basal planes approximately aligned with the surface.

### 3.4.2 Crack initiation and path in $\alpha$-case

It was known from previous studies of crack growth in titanium [58], that crystallographic orientation has a marked effect on the location and direction of crack initiation. The majority of the research conducted in this area focused on fatigue, rather than monotonic loading, so it was not clear whether similar mechanisms would apply. One of the key findings from the work of Bantounas et. al. [58] was that fatigue crack initiation in uni-directionally rolled, cross-rolled and forged bar, would always occur in grains with a c-axis orientation of 15-40° to the principal loading direction. This cracking proceeded by faceted growth along a near-basal plane, and although initiation was limited to grains with a small range of orientations, propagation would then occur in a similar manner, but c-axis orientation varied from 0-90° to the principal loading direction, whilst still exhibiting near-basal faceting. The work of Williams et. al. [59] on fracture topography included an observation on the crack mechanisms in $\alpha$-titanium, which corroborate the effects which were seen in the $\alpha$-case. From examining the fracture faces of various titanium alloys, Williams noted that the yield strength of the $\alpha$-phase related to which of three mechanisms it failed by: at low strengths, the primary mechanism was alternating shear, identified by evidence of serpentine glide. At intermediate strengths, microvoid coalescence became the dominant mechanism, with the size of the dimples inversely related to the strength, and at the highest strengths, cleavage fracture occurred.
The point of crossover between these mechanisms was not found to be distinct, rather a region of mixed-mode fracture was usually identified, in particular between the areas of cleavage fracture and microvoid coalescence. This was determined to be due to the crystallographic orientation sensitivity of cleavage fracture; the cleavage plane in Ti-Al systems was established as being near to $(10\bar{1}7)$ - $(10\bar{1}8)$, and when the resolved normal stress on these planes was high, the resolved shear stress for $\langle 1120 \rangle$ slip was low.

There is a clear similarity between these observations from Williams et. al., and the varying fracture features which were identified in the cracked $\alpha$-case specimens, such as shown in Figure 3.26. The continuously decreasing oxygen concentration through the $\alpha$-case from surface to bulk Ti-6Al-4V draws a close parallel to the various strengths of $\alpha$-titanium to which Williams referred, given the well established relationship between oxygen content and strength, as illustrated in Figure 3.28. The features in the $\alpha$-case can therefore be compared to these three mechanisms, to test whether they can be applied in this situation. The region of highest oxygen concentration was the first 2 - 10 $\mu$m below the surface, which was thought to be close to oxide in composition. This is outside the range which was examined by Williams et. al., so will not be considered at this stage. The oxygen level continued to decrease towards the bulk, and between approximately 10 and 100 $\mu$m from the surface, dependent on specimen condition, the fracture

appearance could be seen to exhibit clear faceting, the orientation of which differed in each grain. This was comparable to the cleavage fracture which Williams found to occur in high strength $\alpha$-titanium, and so it stands to reason that the mechanism may be similar.

The faceted appearance began to show some evidence of a second mecha-

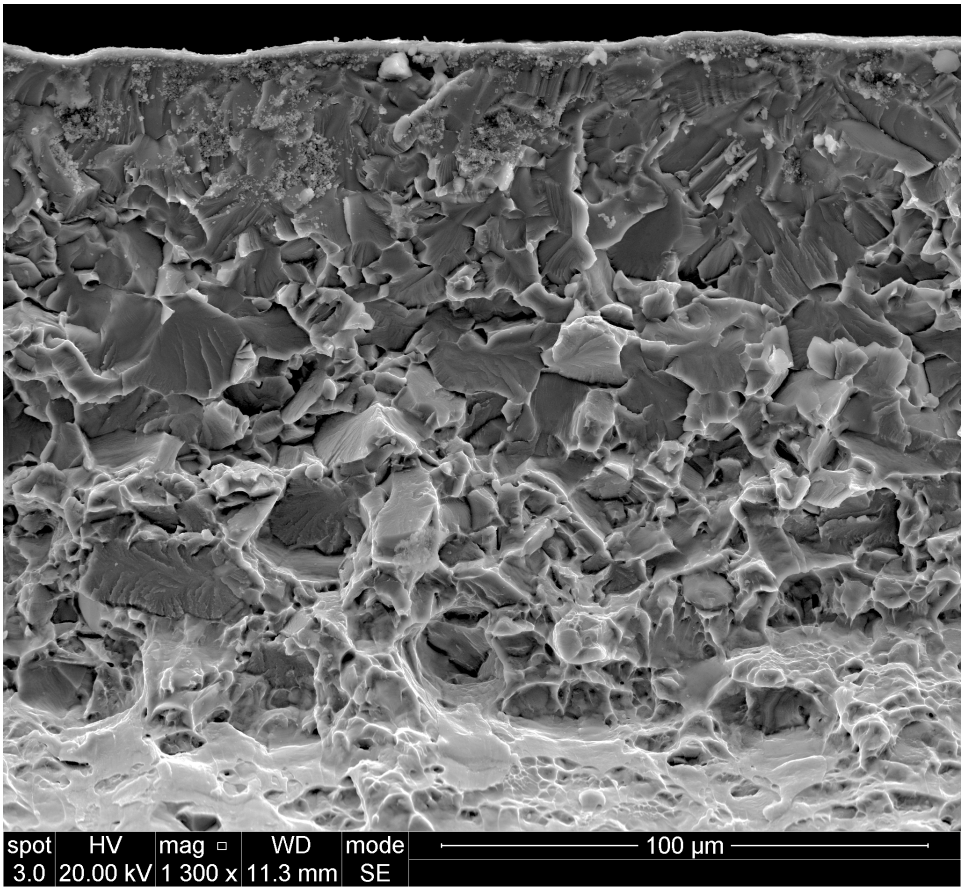


Figure 3.26: Secondary electron SEM image of fracture face of membrane specimen tensile tested at room temperature, following formation of $\alpha$-case by exposure to 1 % $O_2$, 99 % Ar for one hour at 900℃, followed by 5 % $N_2$, 95 % Ar for one hour at 900℃.The fracture face shows three distinct fracture modes; cleavage, slip, and microvoid coalescence. The hardness profile for this specimen is shown in Figure 3.27.

nism operating, as oxygen concentration continued to decrease towards the bulk. This was visible as dimples, interspersed with faceted grains initially, before becoming the sole feature at approximately 120 $\mu$m from the surface, through to the bulk. The size of the dimples increased through this range, in keeping with Williams' finding, and suggesting that microvoid coalescence is operating in this region, in combination with cleavage fracture only where

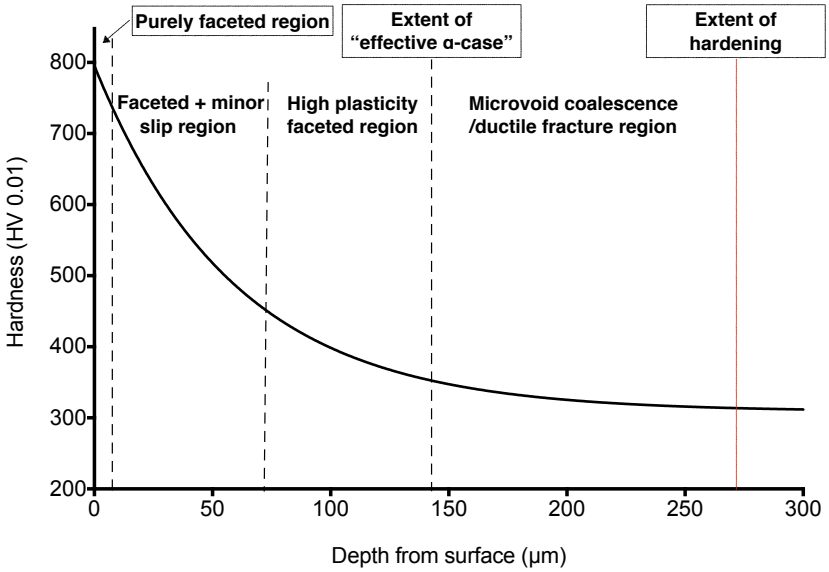


Figure 3.27: Micro-Vickers hardness profile of the specimen seen in Figure 3.26. The $\alpha$-case was formed by exposure to 1 % $O_2$, 99 % Ar for one hour at 900°C, followed by 5 % $N_2$, 95 % Ar for one hour at 900°C. The annotated regions relate to the different fracture appearances which can be identified in Figure 3.26.

the orientation strongly favours it.
Evidence of serpentine glide was not identified in any of the specimens, which was the third mechanism in the group which Williams proposed. However this may be on account of the bulk oxygen concentration of Ti-6Al-4V, at 2000 ppm, compared to <1500 ppm in the CP titanium in Williams' study. This, in combination with the six wt.% aluminium in Ti-6Al-4V, leads to the lack of any real "low strength $\alpha'$", which was said to be required for serpentine glide to occur.

One aspect which this comparison does not account for is the "stepped" appearance of many of the fracture facets, which are evidence for the occurence of limited slip. These stepped facets occur between the "smooth" cleavage facets, and the dimpled regions, implying that another mechanism is operating at an intermediate oxygen concentration. Figure 3.29 shows an example of a fracture surface exhibiting both forms of facets; from the surface, at the top of the image, to a depth of approximately 5 $\mu$m, only cleavage fracture is observed. Beyond this point, limited slip begins to occur, with the depth of onset varying by grain. For example, by following the annotated vertical line downwards, from the surface towards the bulk, three separate grains are passed through, each with different fracture characteris-

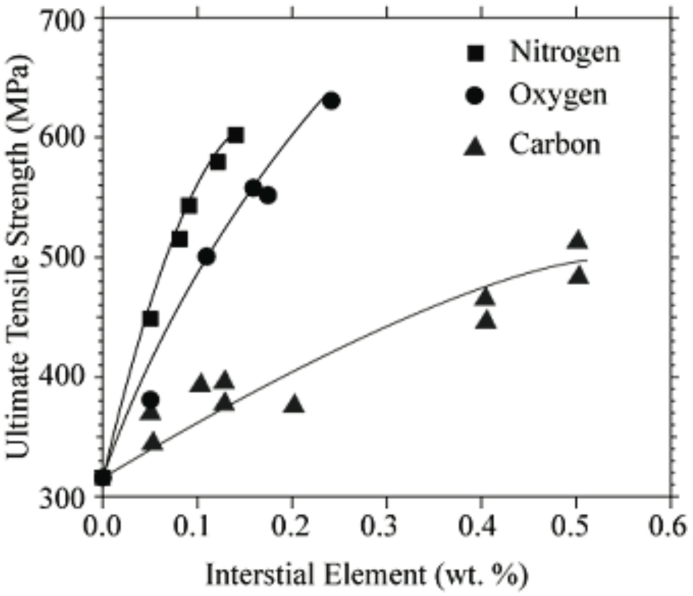


Figure 3.28: Figure illustrating the effect of three interstitial elements on the ultimate tensile strength of CP-titanium. [60]

tics. At the top centre of the figure, grain "1" demonstrates pure cleavage fracture, which extends from the surface to 5 $\mu$m depth. Directly below this, grain "2' shows some evidence of limited slip, in the region of 5 $\mu$m - 12 $\mu$m from the surface. Beyond this point, the degree of slip incorporated becomes much more significant, as seen in grain "3", and this progresses to the stage that the slip plane appears to become the dominant factor in the crack path, rather than the principal stress direction.
The crack path through $\alpha$-case can therefore be broken down in to five or six stages from surface to bulk:

1. Near-oxide composition. Crack initiates perpendicular to the direction of applied stress.

2. Crack progresses by cleavage fracture, with no evidence of slip. Controlled by linear elastic fracture mechanics (LEFM)

3. Mixed mode of cleavage fracture and limited slip. The former dominates, and crack path is still largely dictated by applied stress direction, with LEFM controlling the growth.

4. Mixed mode of cleavage fracture and extensive slip. The latter dominates, and the crack path will follow preferred slip planes where the grain is oriented such that the critically resolved shear stress is exceeded at a stress below that required for cleavage fracture. As $K_IC$

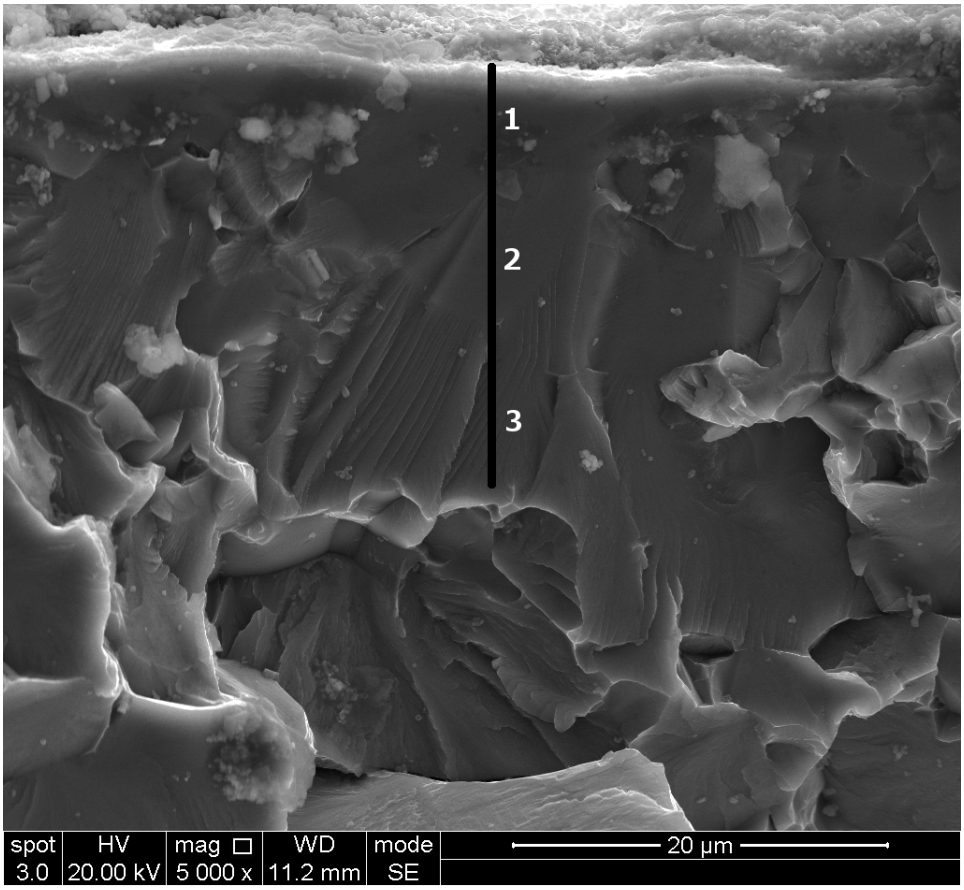


Figure 3.29: Secondary electron SEM image of fracture face of specimen tensile tested at 300℃, following formation of $\alpha$-case by exposure to 5 % $O_2$, 95 % Ar for one hour at 900℃. The transition from cleavage fracture to limited slip can be identified at depths of 7 $\mu$m - 15 $\mu$m from the surface, dependent on grain orientation. The grain annotated "1" shows pure cleavage fracture, grain "2" has evidence of limited slip, grain "3" shows substantial slip.

increases with decreasing oxygen content, the greater the distance from the surface, the higher the probability of slip occurring.

5. Microvoid coalescence. When the oxygen level drops sufficiently, slip becomes unfavourable and the crack propagates through microvoid coalescence, with the void size inversely correlating with oxygen content.

6. Serpentine glide - not detected in this material. This mechanism occurs in lower strength titanium alloys, and may be observed in Ti-6Al-4V if the bulk oxygen content is sufficiently low.

### 3.4.3 Comparison between material with and without $\alpha$-case

It was necessary to include control specimens in the testing programmes; specimens without any $\alpha$-case, in order to provide a reference against which the specimens with $\alpha$-case could be compared, and to confirm that the results observed were as a result of the interstitial enrichment, not just the temperature cycles. The reference specimens therefore underwent the same thermal process as used to form the $\alpha$-case, but with an atmosphere of 99.9999 % argon, to ensure that no contamination would occur. The testing at elevated temperatures was also performed under an argon atmosphere for these specimens. Figure 3.30c includes the stress strain curves for various specimens without $\alpha$-case, and a micrograph from a typical post-test membrane specimen is shown in Figure 3.30b, with a specimen with $O_2$-stabilised $\alpha$-case and tested under similar conditions shown in Figure 3.30a for comparison. No surface cracks formed in any of the specimens without $\alpha$-case, and there was no discernable difference in the bulk microstructure between the specimens with and without $\alpha$-case, indicating that the cracking was due to the $\alpha$-case, rather than the effect of the heat treatment cycle on the material.

A comparison between selected membrane samples with, and without $\alpha$-case is shown in Figure 3.30c. At each temperature the two specimens exhibit stress/strain curves with an identical elastic region, and in the case of the 600℃ samples, this continues beyond the yield point. The samples with $\alpha$-case then fracture at a substantially lower strain than those without $\alpha$-case, due to the surface cracks propagating through the material, and it was thought that the moment of failure was likely to correspond to the crack entering the microvoid colescence phase of its growth. The stress in the 600℃ specimen with $\alpha$-case was no lower than the specimen without $\alpha$-case, which implies that the crack depth prior to failure was very shallow, as it was not sufficient to noticeably reduce the cross sectional area. This supports the theory that the "effective $\alpha$-case" depth at this temperature is greatly reduced compared to lower temperatures, as the material can remain ductile with substantially elevated oxygen levels, therefore only the immediate sub-surface, with the highest oxygen concentration, formed brittle, faceted cracks. The area around these crack tips, which would have had an oxygen concentration substantially above bulk, was able to resist fracture until a much higher strain.

Conversely, the specimen with $\alpha$-case tested at room temperature failed at a substantially lower strain than the one without $\alpha$-case, as the effective case depth at this temperature was far greater than at 600℃, allowing the cracks to rapidly propagate in a brittle manner to a substantial proportion of the material thickness, followed immediately by final fracture.

The specimens tested at 300℃ did not show any notable variation in strain-to-failure, however the key difference between the two was the stress; the

specimen with $\alpha$-case yielded at an apparent stress approximately 50 MPa lower than the specimen without $\alpha$-case, and this disparity remained constant until near the point of fracture. This implied that the $\alpha$-case formed brittle cracks whilst in the elastic region of the deformation, as would be expected, and at this temperature these were of sufficient depth to noticeably impact the cross sectional area of the sample, reducing the calculated stress. As this difference in stress then remained constant, it could be inferred that the cracks were not propagating, since the effect of this would have been a further decrease in the measured load, and therefore calculated stress.

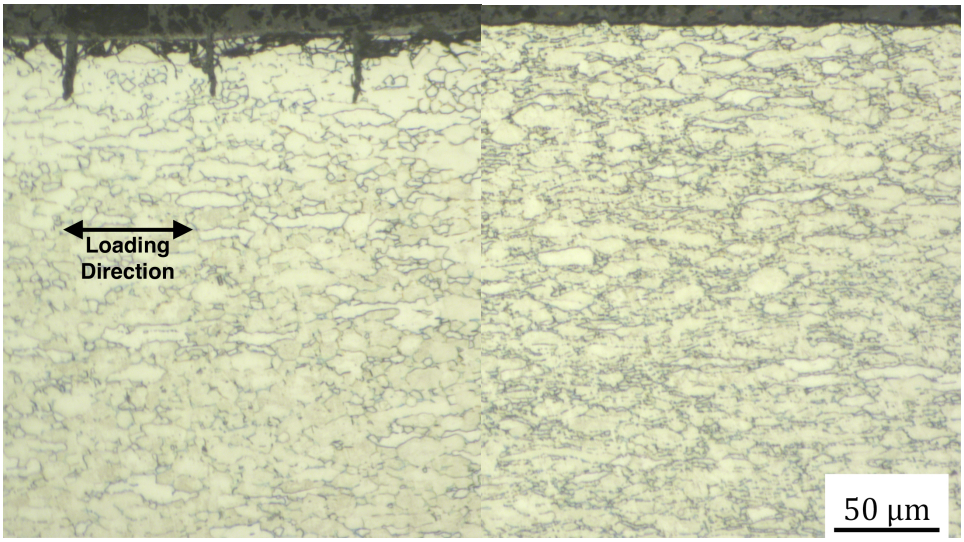


(a) (b)

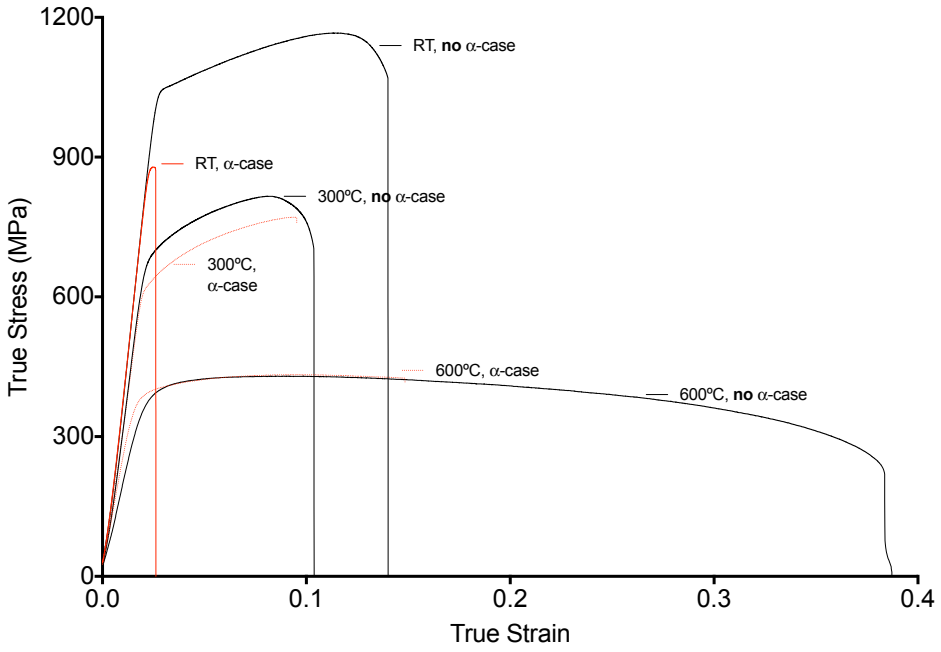


(c)

Figure 3.30: Light optical micrographs of etched Ti-6Al-4V membrane specimens, tensile tested to failure at 300 ℃ in argon. 3.30a had an $O_2$-stabilised $\alpha$-case and exhibited an array of cracks after testing, whereas 3.30b had no $\alpha$-case and did not crack. The stress strain curves in 3.30c, from selected Ti-6Al-4V membrane specimens tested at various temperatures, show the comparison between those with $O_2$-stabilised $\alpha$-case and those without $\alpha$-case.

## 3.5 Analysis techniques for characterising fracture behaviour

Several different techniques were utilised to analyse the fracture behaviour, the combination of which provided a robust assessment of the competing and complimentary mechanisms which were operating. The use of additional characterisation methods, such as quantitative tilt fractography and in-situ SEM tensile testing with DIC, would offer further insight into the behaviour, and this could be a useful area of future research. Conversely, for the regular assessment of material for production, where a sacrificial component or test piece could be analysed for $\alpha$-case by tensile testing, then SEM fractography alone would be sufficient to identify its presence.

### 3.5.1 Secondary electron SEM fractography

Figure 3.31 shows a near-surface region of the fracture face of a specimen tested at room temperature, with an $\alpha$-case formed by exposure to oxygen followed by nitrogen. The evidence of slip highlights one of the benefits of SEM fractography as a method for identifying $\alpha$-case, which is its ability to determine the degree to which the $\alpha$-case is controlling the fracture behaviour. The stage of the fracture at any given depth can be used to quantify the effect of the $\alpha$-case at that point, as discussed in section 3.4.2, and this is perhaps the best measure of "effective" $\alpha$-case depth.

For the analysis of fracture faces, SEM is often the most appropriate tool available, due to its large depth of field, necessary on three-dimensional fracture surfaces; and high resolution, which is required to identify the features associated with fracture mechanisms. Energy-dispersive x-ray spectroscopy (EDX) can be a powerful addition to SEM analysis, for the detection of chemical elements which may be linked to the fracture, or inhomogeneity in the material[61, 62, 63]. However in the instance of $\alpha$-case it is of limited value, due to the inability of EDX to quantitatively measure the concentration of light elements such as oxygen and nitrogen.

Light optical microscopy does have certain benefits over electron microscopy, such as the ability to view colours in the specimen, which can provide information which would not be obvious in an SEM. This can include thin oxidation films, or be linked to chemical deposits, such as in the work on "Blue Spot" in titanium by Saunders et al. [64].

Stereo light microscopy can be particularly useful for fracture surface analysis, as it can provide a large depth of field, but at lower magnifications than an SEM, which can be beneficial in the identification of macro level features, and the application of oblique lighting can aid in this. This technique was used throughout this study as a precursor to SEM examination, to identify the regions to be examined at high resolution, and aid in determining the most appropriate angle and method used to mount each specimen.

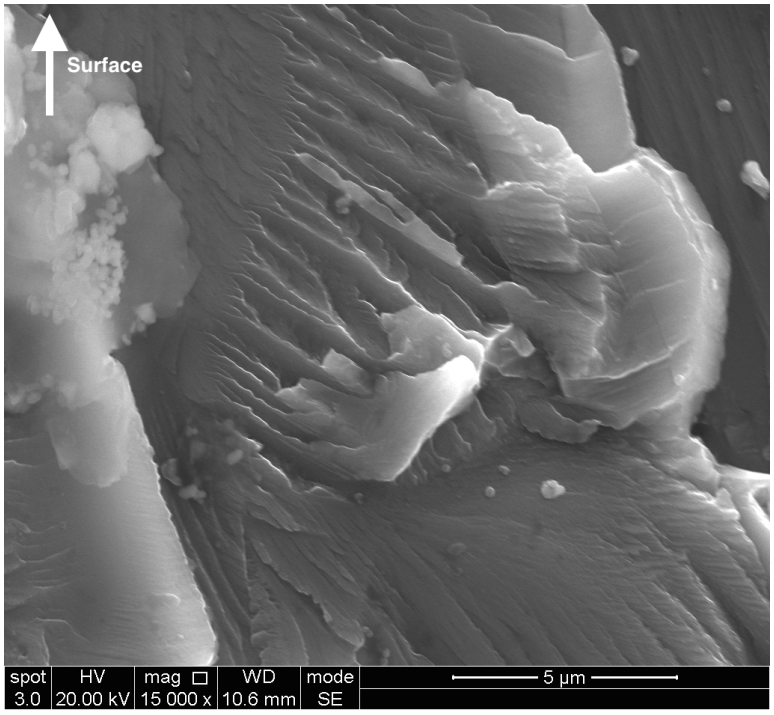


Figure 3.31: Secondary electron image of fracture face, showing evidence of limited slip in the near-surface region (approximately 30 $\mu$m below the surface) of a Ti-6Al-4V membrane specimen exposed to 5 % $O_2$ followed by 5% $N_2$, each for one hour at 900℃, and tensile tested at room temperature.

The SEM used to obtain the majority of the figures presented here was an FEI InspectF FEG-SEM, with some images also gathered on a Zeiss SEM at Rolls-Royce plc. in Bristol. The fractured specimens were sectioned on a Struers Secotom 50 precision cut-off machine to separate the fracture faces from the gauge, which were then rinsed in isopropanol to remove any residual cutting fluid. After macro examination under a stereo light microscope to identify areas of interest, the fracture faces were then attached to aluminium SEM sample stubs with faces at 0°, 45°, 70° or 90° as appropriate, using conductive carbon tape.

On low magnification, the SEM revealed a visible $\alpha$-case on specimens which were tested at lower temperatures, an example of which can be seen in Figure 3.32. This differed from the visible $\alpha$-case referred to in Section 2.2.2, seen in cross-section, which was a result of the degree of phase-stabilisation, whereas what could be seen in the SEM was linked to the fracture mechanism.

At higher magnifications, such as shown in Figure 3.26, this visible $\alpha$-case was observed to be demarcated by the switch to purely microvoid coalescence. As discussed in Section 3.5.2, the depth of this point corresponds to

the maximum depth of the other cracks in each specimen, which did not progress to fracture. This was quite a significant finding, as it linked the cracking in $\alpha$-case, which had been observed previously by other researchers [49, 5], with the mechanism by which these cracks were propagating. The visible $\alpha$-case on a secondary electron image of a fracture face can be considered to be the effective $\alpha$-case depth, and by removing this thickness of material from an identical sample's surface, it would not be expected to crack under the same testing conditions.
Furthermore, due to the other cracks in a specimen also displaying this same depth, inhomogenities in the material, such as macrozones, can also be accounted for. The combination of mechanisms leading to the crack length in each region would not need to be known, so long as the test specimen was sufficiently expansive, then the depth of the deepest crack which did not proceed to full fracture could be considered to be the $\alpha$-case thickness. For this purpose, it would not be relevant whether the region with this crack provided a more favourable path for interstitial diffusion, or less resistance to crack propagation; just the depth below the surface to which the crack extended.

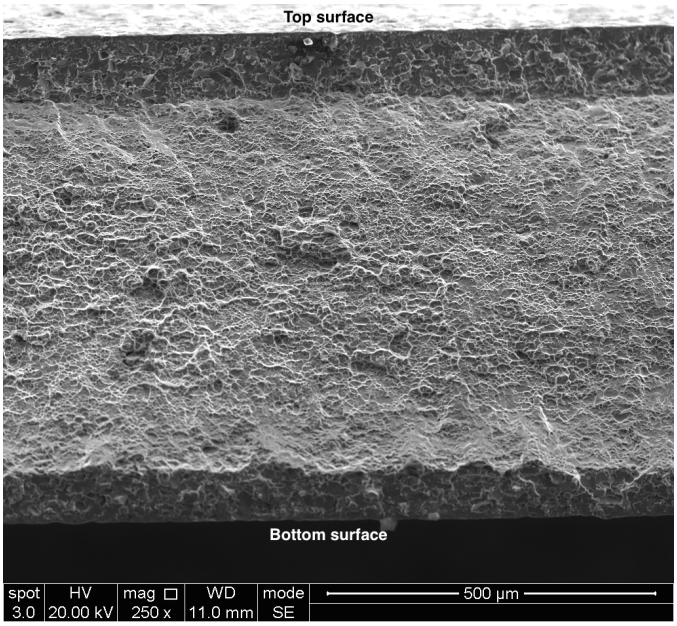


Figure 3.32: Low magnification secondary electron image of the fracture face of a Ti-6Al-4V membrane specimen, exposed initially at 900℃ to nitrogen, followed by oxygen, and tensile tested at room temperature. Some of the effects of the $\alpha$-case can be seen at the top and bottom surfaces of the specimen (top and bottom of the figure, respectively), where the brittle fracture is evident.

Figure 3.33 shows a crack in the surface of a Ti-6Al-4V membrane specimen with oxygen-stabilised $\alpha$-case, which was tensile tested at 500℃ to a total strain of 0.06, after which the load was relaxed. The specimen was extensively cracked across the surfaces, but none of the cracks extended through the thickness of the material. The crack shown exhibits two of the three main phases of fracture development seen in the fractography of failed specimens; the initial two - five micrometres of purely faceted crack growth, followed by faceted growth with a steadily increasing level of slip evident. What cannot be seen is a region of microvoid coalescence, nor was this observed in other cracks in this specimen, suggesting that at this temperature and strain, the $\alpha$-case would crack in the same manner as at lower temperatures, but at a depth of approximately eight micrometres, the value of $K_{IC}$ would be sufficiently high to prevent propagation of the crack by microvoid coalescence. The absence of this region could not be readily verified, however, since there was no open fracture surface to examine, and intentionally opening the fracture, as might be done to inspect fatigue cracks for instance, would not be beneficial, as the fracture surface caused by this process would not be distinguishable from the one being sought.
The oxide layer which formed on all specimens when exposed to oxygen at 900℃ is also visible in Figure 3.33, with a thickness of approximately 0.5 - 1 $\mu$m in this example. The tendency for cracking can be observed, with cracks both parallel and perpendicular to the loading direction. This is not thought to play any noticeable role in the cracking of the metallic substrate, as at this thickness the oxide is not sufficiently coherent with the metal for cracks to transition from the oxide.

### 3.5.2 Light optical microscopy of polished cross-sections

Ti-6Al-4V specimens afflicted with $\alpha$-case were found to exhibit regular arrays of surface cracks following tensile testing, which could readily be observed from the surface, as shown in Figure 3.34. The cracks would always form orthogonal to the loading direction, and their extent varied from the full specimen width to approximately 10 % of the width, depending on whether multiple cracks connected, or one crack could continue uninterrupted.
Sectioning the specimens longitudinally, followed by mounting the cross section and preparing using standard metallurgical procedures, allowed the depth and paths of these cracks to be analysed with light optical microscopy. Both brightfield and darkfield microscopy were used for the identification of cracks, which could sometimes be difficult to detect with the shorter and finer cracks. Specimens were examined in both the unetched condition, and after etching in Kroll's reagent (6 vol. % $HNO_3$, 2 vol. % HF in distilled $H_2O$) for approximately 10 seconds to reveal the grain structure.

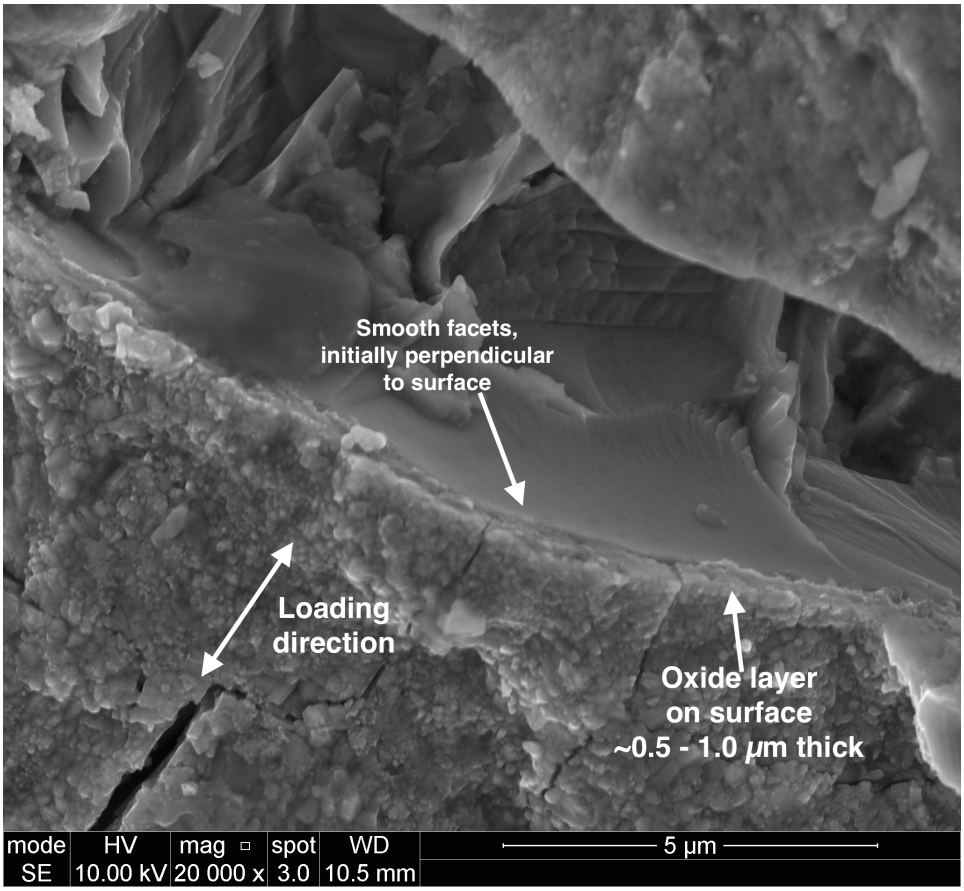


Figure 3.33: Secondary electron image of the surface of a Ti-6Al-4V membrane specimen, with oxygen-stabilised $\alpha$-case, tensile tested at 500℃. The main crack in the image ran in the transverse direction across the specimen, which exhibited numerous similar cracks. The smooth facets immediately below the oxide layer can be seen to transition to facets with slip-lines within the first few microns.

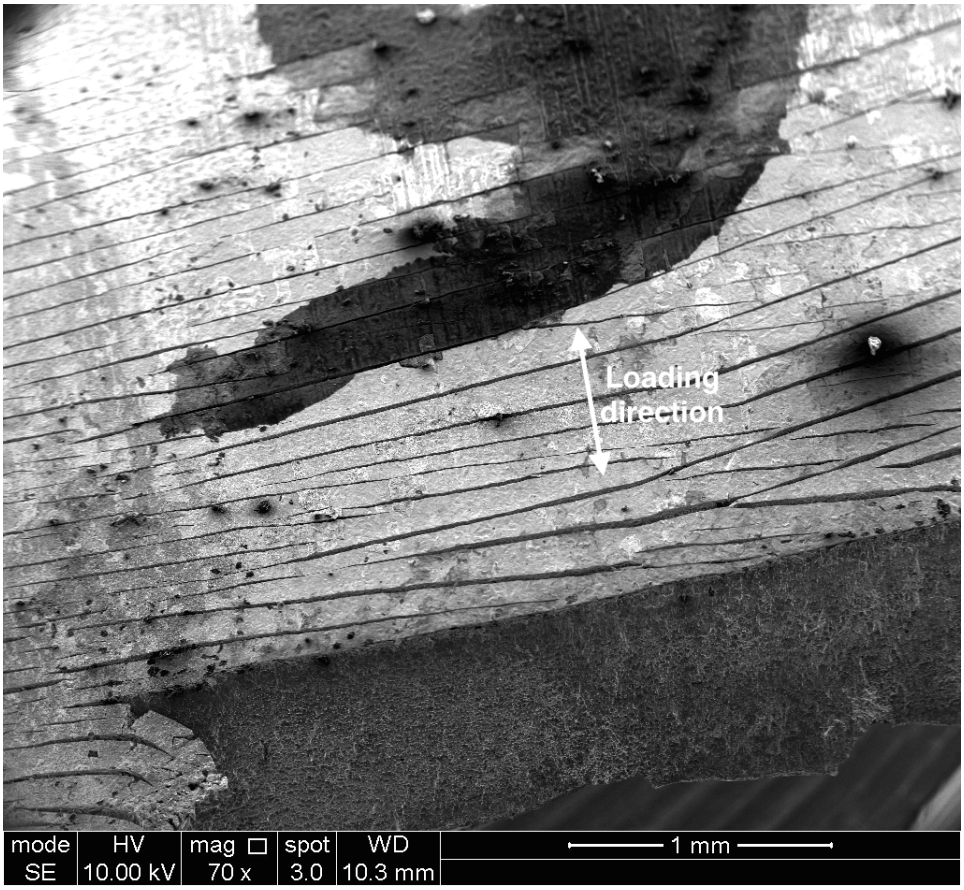


Figure 3.34: Secondary electron image of the surface of a Ti-6Al-4V membrane specimen, with oxygen-stabilised $\alpha$-case, tensile tested at 400℃. The point of final fracture is near the bottom of this figure. The regular array of cracks seen across the surface was observed on almost all specimens, and is indicative of the presence of $\alpha$-case. The black regions on the surface of this image are specimen identification markings.

Analysis of the polished cross sections revealed distinct regularity to the cracks, which would typically exhibit one of two patterns:

1. Singular array of cracks, similar in depth and path. See Figure 3.35
2. Duplex distribution of cracks. One array comparable to 1), interspersed with a second array of finer, shorter cracks. See Figure 3.36

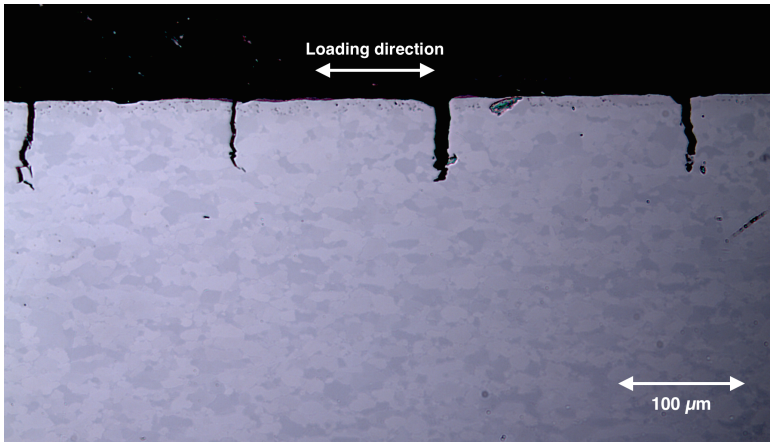


Figure 3.35: Light optical micrograph with cross-polarised light, showing a single array of cracks in a Ti-6Al-4V membrane specimen, with $\alpha$-case formed by exposure to 5 % $O_2$ at 900℃ for one hour, followed by tensile testing to failure at room temperature.

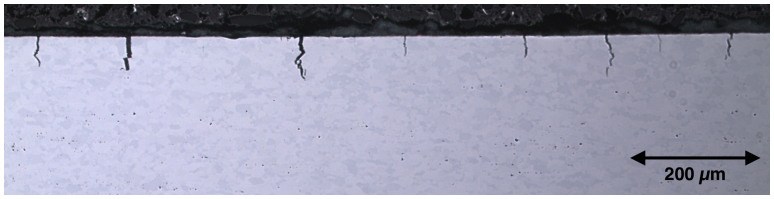


Figure 3.36: Light optical micrograph with cross-polarised light, showing duplex arrays of deep, coarse cracks and fine, thin cracks, in a Ti-6Al-4V membrane specimen, with $\alpha$-case formed by exposure to 5 % $N_2$ at 900℃ for one hour, followed by tensile testing to failure at room temperature.

The similarity between adjacent cracks in the singular array was high, with each crack exhibiting three main stages of growth, marked in Figure 3.37, which occurred at approximately the same distance beneath the surface within each specimen:

1. Crack initiation perpendicular to the surface. The stage of growth immediately following initiation extended approximately five microme-

tres, and was always perpendicular to the surface, within one or two degrees, apparently regardless of crystallographic texture.

2. Crack growth approximately perpendicular to the surface, but with some sensitivity to grain orientation, typically extending tens of micrometres. The boundary between this and Stage 1 was often indistinguishable in the cross sections, as the crack direction had not altered, however the crack path would sometimes reorient by several degrees, seemingly along a "soft" direction through a particular grain, or around the boundary of a grain oriented in a particularly "hard" direction.

3. Crack propagation controlled by crystallographic orientation, generally following the "soft" direction through a grain, or an intergranular path when this was not favourable. This stage would generally terminate at a comparable depth in all cracks with a specimen, within one grain diameter. This variation is likely due to the random orientation of the grain encountered by each crack near the point at which it terminated; a "harder" orientation would arrest the crack, whilst a "softer" orientation would allow it to proceed through the additional grain.

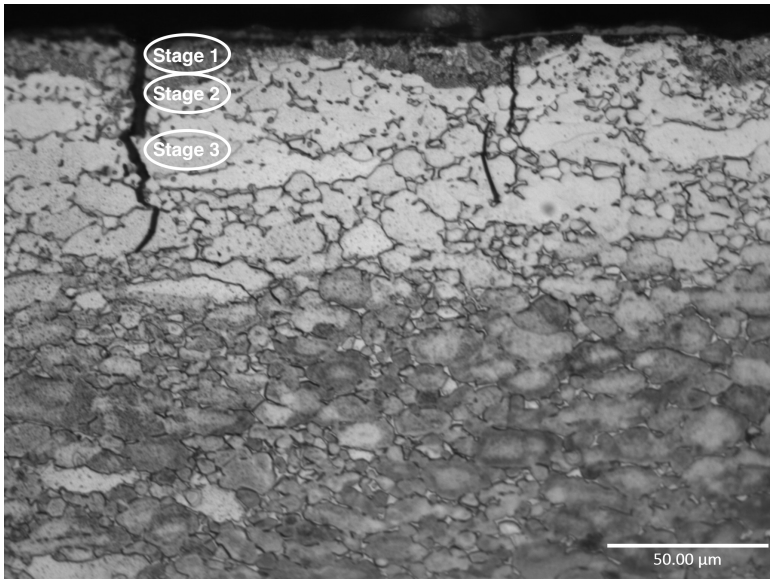


Figure 3.37: Light optical micrograph of an etched Ti-6Al-4V membrane specimen, with $\alpha$-case formed by exposure to 5 % $O_2$ at 900°C for one hour, followed by tensile testing to failure at room temperature. Three apparent stages of crack growth can be observed, which each occur at similar distances from the surface in every crack within the singular array in a specimen.

These stages clearly relate to the different regions of crack growth identified by fractography, as discussed in Section 3.4.2, and the comparison between the two can be seen visually in Figure 3.38. Comparison of the depths of cracks measured in cross section, with the fractography from the same specimens shows that the point at which the majority of cracks in an array terminate corresponds to the beginning of the microvoid coalescence phase of the crack which continued to full fracture. This suggests that the apparent absence of evidence of microvoid coalescence when viewing open cracks from the surface, as noted in Section 3.5.1, may be correct, and this stage only occurs at the point when one crack proceeds to fracture. It could be considered, especially if using the "traditional" $\alpha$-case definition of a discrete layer of $\alpha$-phase, that the termination of the cracks was linked to a change in microstructure. However this was considered unlikely, on account of the gradual transition of the $\alpha$-case to bulk, and the limited difference in crack propagation resistance between the microstructures present [65][66].

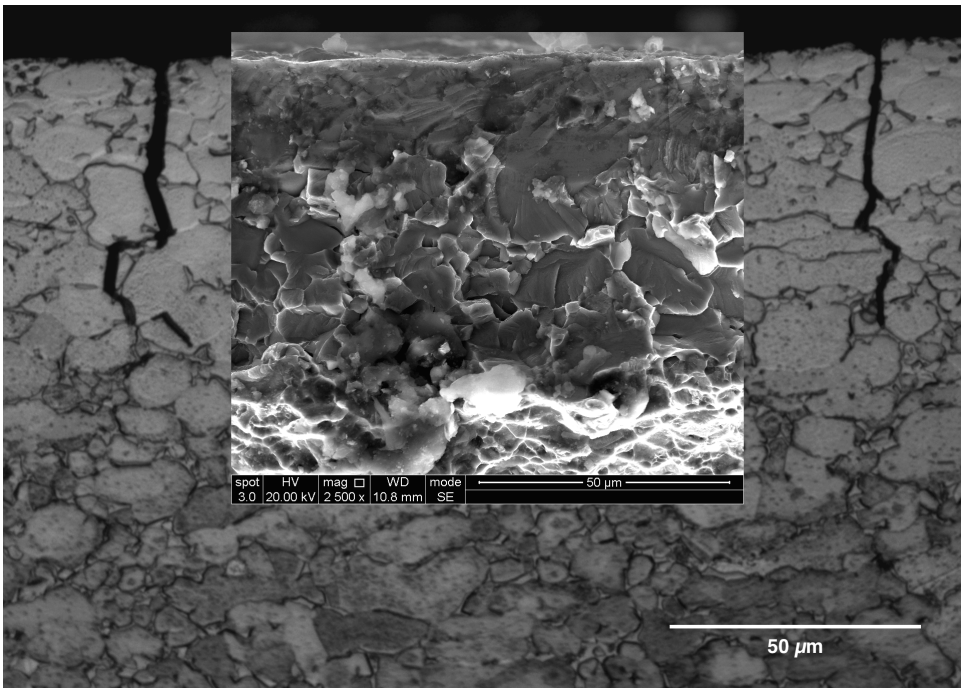


Figure 3.38: Composite image of fracture face and etched cross section, showing a comparison between crack path and fracture appearance. The two cracks shown in cross section did not progress beyond the region of faceting to the dimpled region, suggesting that these cracks experienced only cleavage fracture, and not microvoid coalescence. This specimen was exposed to an atmosphere of 5 % $O_2$, 95 % Ar, for 1 hour at 900℃, and uniaxially tensile tested to failure under monotonic loading. Note that the actual orientation of the fracture face is 90° to how it is shown, i.e. orthogonal to the page.

The second array was observed more commonly in specimens with a nitrogen-stabilised $\alpha$-case than an oxygen-stabilised case, however it was identified in both cases, and in cumulative exposures. Studies of crack formation in surface coatings have revealed a similar grouping effect, where cracks formed with regular spacing under tension, but with the continued increase in strain, the midpoint between each pair of cracks nucleated another crack, leading to a second regular array to be formed. This process would continue, bisecting the gap between cracks until the specimen failed. A similar process has been found to occur in surface coatings bonded to a substrate [67], which although a different situation, since $\alpha$-case is not bonded to the surface, but rather is a largely coherent region of the surface, some parallels can still be drawn.

It is thought that this was the mechanism by which increasing strain was accommodated in all tested specimens, however positive identification was often not possible from the cross-section of a fractured specimen. The higher proportion of nitrogen-stabilised specimens exhibiting the effect than oxygen-stabilised specimens is likely due to the shallower $\alpha$-case present in the former, leading to the primary cracks' growth terminating at a lower strain. This caused these cracks to open to a greater width, emphasising the difference between them and the secondary cracks.

The interrupted tensile testing, discussed in Section 3.2.4, was used to identify the formation of the primary and secondary cracks in some specimens. Figures 3.39, 3.40a, 3.40b and 3.41 show the progressive crack formation in three nominally identical specimens of unidirectionally rolled Ti-6Al-4V plate, which were tensile tested to preset strains of 0.02, 0.03, 0.04 and 0.05. The lowest strain, shown in Figure 3.39, was sufficient to form the primary array of cracks, which at the point of test termination appeared to be propagating in Stage 3 of the crack growth, as described in Section 3.5.2.

At 0.03 strain, the array of secondary cracks had nucleated, marked "2" in Figure 3.40a, subdividing the array of primary cracks. The depth of the primary crack in this image, marked "1", is shorter than others seen in the specimens which experienced a higher total strain, which appears to suggest that the secondary cracks initiated before the growth of the primaries had ceased. However examination of the other primary cracks in this specimen found them to be deeper, implying that the relatively short length of the primary crack in this image was due to microstructural variation, and that most likely it had stopped propagating at this point.

At a strain of 0.04, the difference between the primary and secondary cracks can be seen clearly in Figure 3.40b, where the primary crack, again marked "1", is substantially deeper and broader than the secondary crack, the visible breadth being a result of the crack opening both in the plane of the paper, perpendicular to the crack direction, and also orthogonal to the page. The primary crack tip represents the limit of the "effective $\alpha$-case", where the ductility of the material becomes sufficient to prevent further crack propa-

gation at this stress.
An increase in strain to 0.05 caused the secondary cracks to also reach this point, shown in Figure 3.41, which also did not propagate any further. This was approaching the limit of the total strain that the material would achieve under these conditions, and only one specimen did not fracture before reaching the next integer strain value of 0.06. A composite image of the array of cracks is shown in Figure 3.42, the spacing of which was similar to that in Figure 3.41, suggesting that a tertiary array of cracks *did not* nucleate; instead the breadth of the existing cracks increased to accommodate the strain. The crack spacing and depth controls this behaviour, and evidently at this spacing of approximately 200 $\mu$m and effective $\alpha$-case depth of 80 $\mu$m, it was not favourable for additional cracks to nucleate. Had the specimen reached a higher strain before the bulk material fractured, then it is expected that this situation would tend towards generating further arrays of cracks.

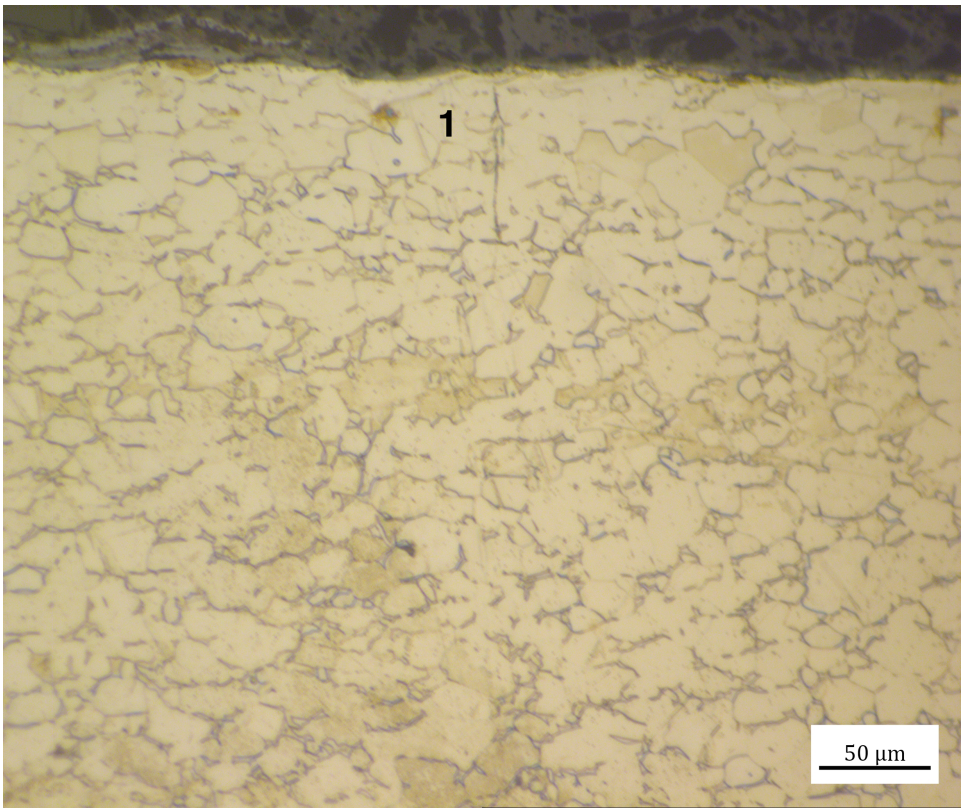


Figure 3.39: Light optical micrograph of an etched Ti-6Al-4V UD specimen, with $\alpha$-case formed by exposure to 5 % $O_2$ at 900℃ for one hour, followed by tensile testing to a preset strain of 0.02 at room temperature. A single primary crack is visible, which is part of an array of such cracks across the specimen.

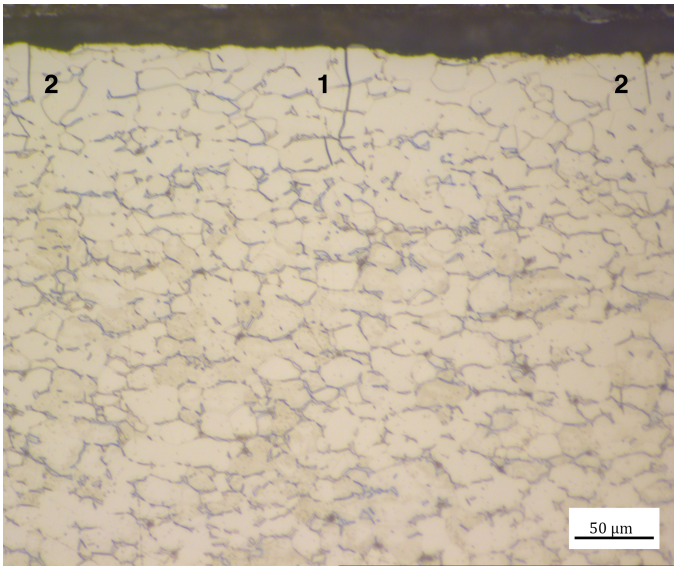


(a)

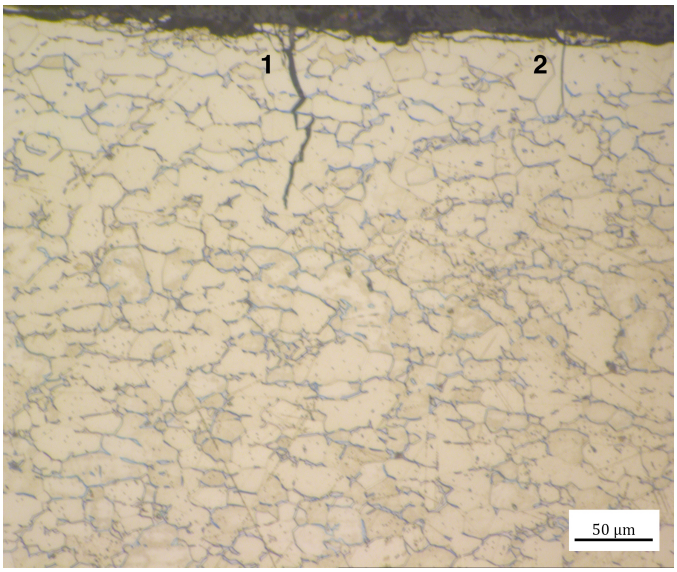


(b)

Figure 3.40: Light optical micrographs of etched Ti-6Al-4V UD specimens, with $\alpha$-case formed by exposure to 5 % $O_2$ at 900℃ for one hour, followed by tensile testing to a preset strain of 0.03 (3.40a) or 0.04 (3.40b) at room temperature. In 3.40a, three thin cracks are visible; a primary crack, marked "1", and two secondary cracks, marked "2". In 3.40b, a crack from the first array, marked "1", appeared to have stopped growing, and secondary array of cracks nucleated to accommodate the strain, one of which is shown here marked "2"

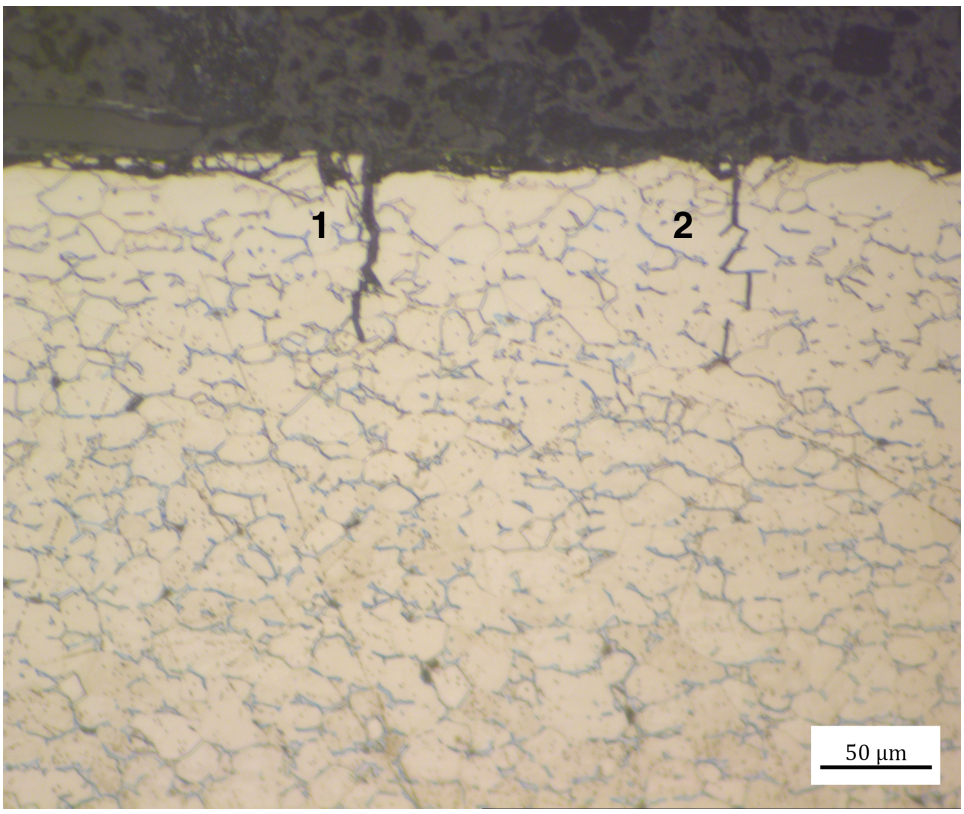


Figure 3.41: Light optical micrograph of an etched Ti-6Al-4V UD specimen, with $\alpha$-case formed by exposure to 5 % $O_2$ at 900℃ for one hour, followed by tensile testing to a preset strain of 0.05 at room temperature. This specimen was taken to a slightly higher strain than Figure 3.40b, which was sufficient for the secondary crack, marked "2", to reach the same depth as the primary crack, "1".

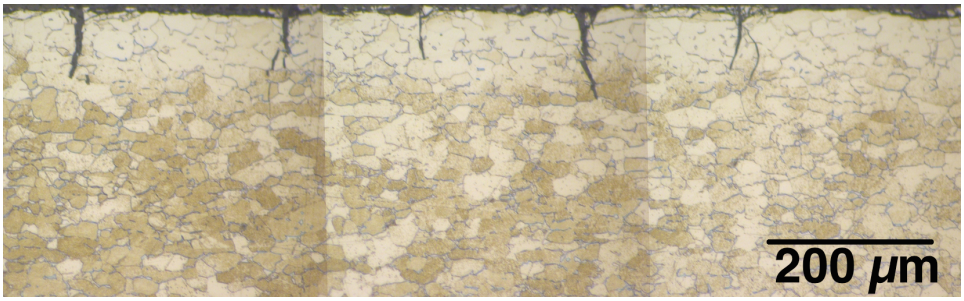


Figure 3.42: Light optical composite micrograph of an etched Ti-6Al-4V UD specimen, with $\alpha$-case formed by exposure to 5 % $O_2$ at 900℃ for one hour, followed by tensile testing to a preset strain of 0.06 at room temperature. This specimen reached the highest strain of any in this set without fracture, but still initiated only two separate arrays of cracks.

### 3.5.3 Electron backscatter diffraction (EBSD) analysis

It was clear from the fractography and cross-section analysis that crystallographic orientation was a factor at some positions within the $\alpha$-case, but not others. In order to understand how the orientation was influencing the crack path, a small number of specimens were selected for EBSD analysis. This was conducted on polished cross sections, using an FEI Sirion FEG-SEM. This differed from some other studies on the crystallography of fracture facets [68, 69, 70] which utilised quantitative tilt fractography with EBSD, as this technique is more suited to fully faceted fracture faces, rather than the cross sections of cracks exhibiting several different fracture mechanisms in this study.

Sample geometry was an issue, due to the thin tensile specimens and lack of flexibility in the microscope's sample holder, which required samples at least five millimetres in width, compared to the one millimetre specimen width, when oriented to analyse the face of interest. This was coupled with a need to obtain a finely polished surface with minimal strain imparted by the polishing process, in order to achieve a sufficiently high indexing rate on the EBSD to resolve the necessary features.

The technique utilised to achieve this was hot mounting the specimens to allow the a flat polished surface to be obtained, after which an attempt was made to section the sample to the required size. When successful, this was positioned in the EBSD sample holder, with silver paint to ensure electrical contact with the specimen. When unsuccessful, due to the resin fracturing or de-bonding, the specimen would be entirely separated from the resin, and instead placed in a bespoke aluminium sample holder.

The EBSD analysis was conducted with a step size of 0.5 $\mu$m, which gave sufficient resolution and points within each grain to obtain data from every grain even when the indexing rate dropped below the 85 % that was targeted. The cracks to be analysed were first imaged on a light optical microscope, to provide a higher resolution image of the crack than could be produced by EBSD. When required to clearly see the crack path, these were subsequently superimposed over the EBSD maps, using grain morphology and position over the entire image to ensure the scaling and location were correct. The EBSD data was processed using HKL Channel 5 software, with a moderate level of noise reduction and point interpolation utilised where necessary to aid the completeness of the grain maps. Maps with such post-processing methods applied were compared to the unmodified maps, to ensure that no data was lost or misrepresented.

The tortuous path typical of many cracks observed in $\alpha$-case is shown in Figure 3.43, with IPF colouring and some overlaid HCP crystal schematics to indicate the orientation of each grain. The crack can be seen to have initiated perpendicular to the surface along a pyramidal plane, a relatively

"hard" direction, and continued to progress in this direction along a near-basal direction of the sub-surface grains. At a depth of approximately 20 $\mu$m, the crack had clearly entered Stage 2 or 3 of its growth, and could seen to follow the basal plane of the grains it passed through, to the extent that it would alter direction by up to c. 80° when necessary. In grains in this region where lattice rotation had occurred, either during tensile testing due to extensive wavy slip, or in the initial forming of the material, the crack can be seen to follow an elliptical path as it propagates along the basal plane. An example of this can be seen parallel to the red line annotation, and the misorientation profile chart shows the rotation along this line, with the maximum value of 33° agreeing with the change in crack direction seen in this section.

A weakness with this technique is that whilst the grain orientation can be identified three-dimensionally, the crack is only visible in two-dimensions, and there is no viable method to determine the path or angle of the crack in the plane perpendicular to the page. Assumptions must therefore be made regarding this, and quantitative assessments are not possible, however from a qualitative perspective the information is interesting and provides valuable insight into the mechanisms operating. An example of this limitation can be seen in Figure 3.44, where the region ringed in red shows the crack apparently propagating along the "hard" prismatic plane. It is considered to be unlikely that this was the preferred direction of crack growth here, suggesting that the explanation for this behaviour lies in the crack's position in the plane perpendicular to the page. If the crack's direction was constrained by the grains in this plane on either side of the ringed grain, for instance if these were oriented with the basal plane aligned with the crack direction seen in the image, then this may have made it favourable for some intermediate sections of the crack front to propagate along the prismatic plane, rather than deviate around. The use of quantitative tilt fractography could provide more definitive information on this type of occurrence, if the cracks and grains of interest were identified in cross section and the cracks were then "broken open", in tension or bending. This would allow the third dimension to be viewed and correlated with this cross-section information. The challenge would be in ensuring that the correct crack proceeded to fracture, given that a 20 mm section of material would likely contain many tens of cracks, however if a sufficient number of candidate cracks could be identified, then the odds of success would substantially improve.

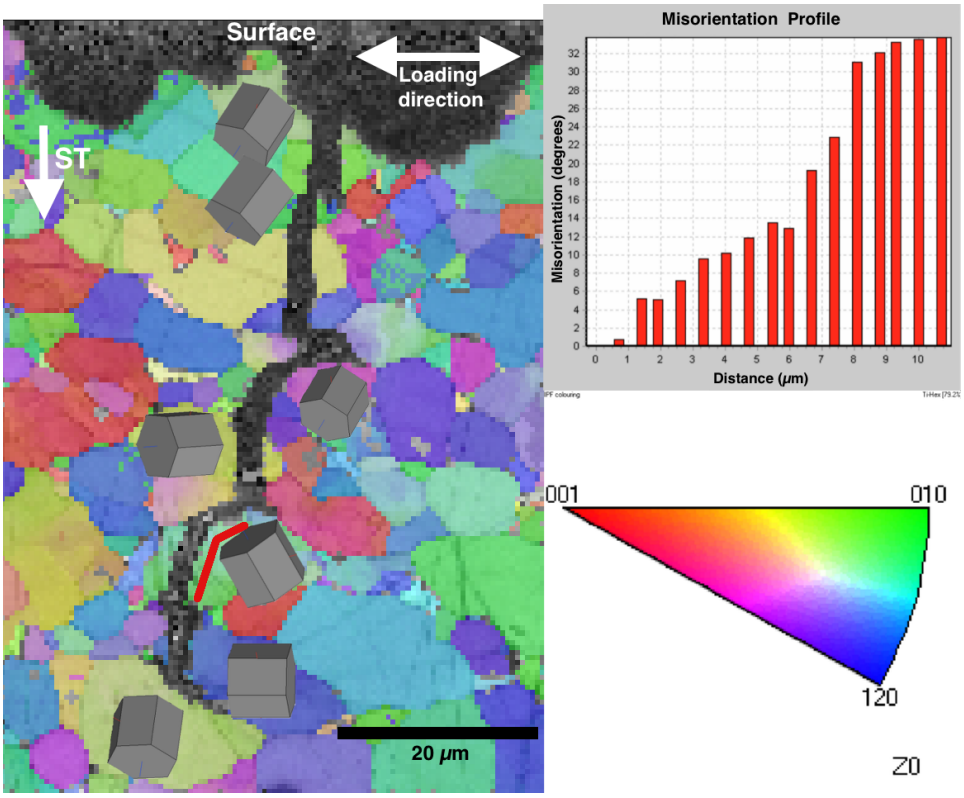


Figure 3.43: EBSD map with Z-direction IPF colouring, showing the path of a typical crack in a specimen with $\alpha$-case developed from exposure to 1 % $O_2$ for one hour at 900℃, followed by 5 % $N_2$ at 900℃, and tensile tested to failure at RT. The overlaid HCP crystals indicate the orientation of most of the grains that the crack passed through, showing the effect of orientation on crack direction. The red line shows the area analysed within one grain to produce the misorientation chart shown, demonstrating the influence of lattice rotation on crack path.

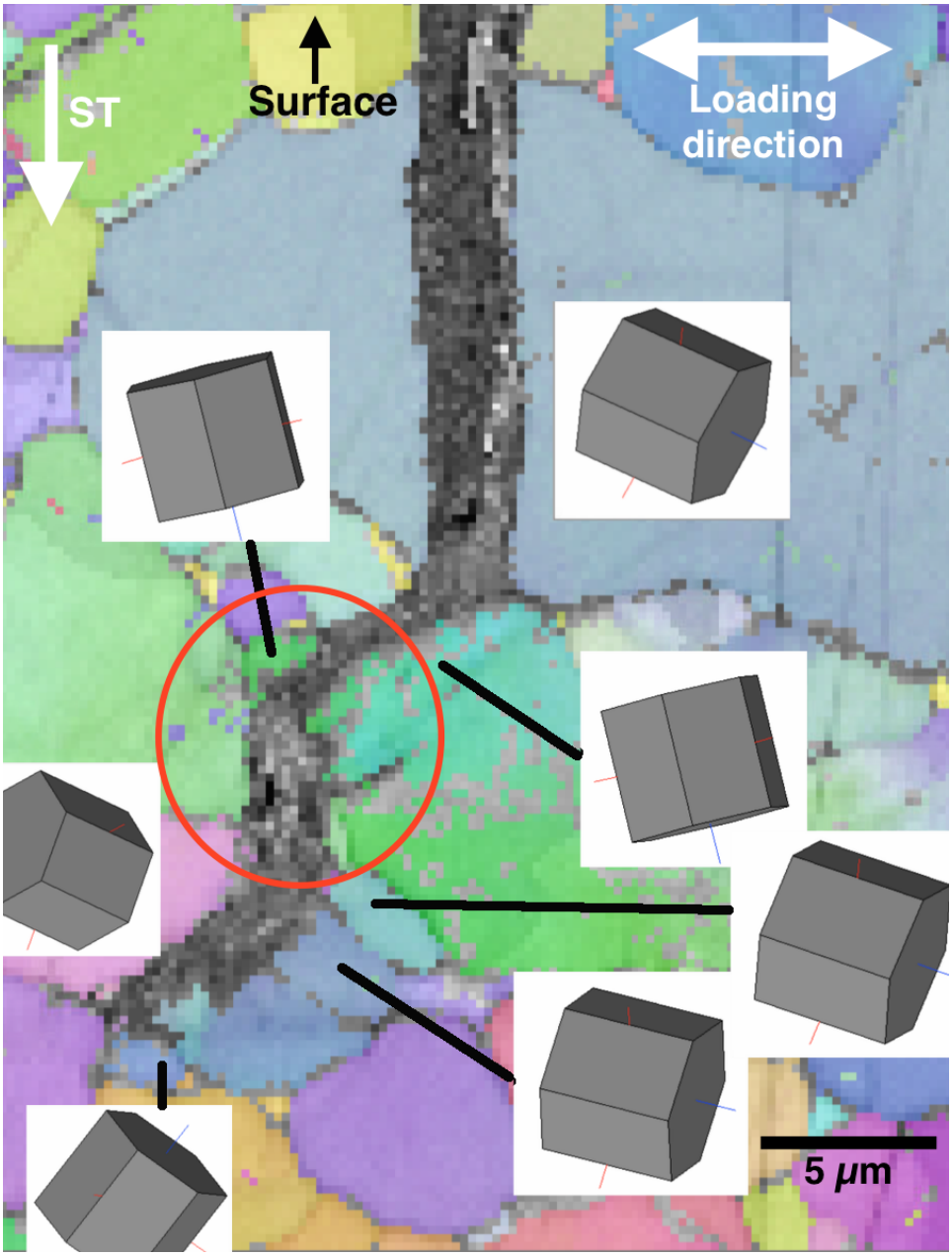


Figure 3.44: EBSD map with Z-direction IPF colouring, showing the path of a typical crack in a specimen with $\alpha$-case developed from exposure to 5 % $O_2$ for one hour at 900℃, and tensile tested to failure at RT. The overlaid HCP crystals indicate the orientation of most of the grains that the crack passed through, indicating that the crack direction is near-basal, except for the region ringed in red, which shows the crack apparently propagating along the prismatic plane, a "hard" direction.

## 3.6 Factors influencing the mechanisms of crack propagation

It has been established through SEM and light microscopy in Section 3.5 that the crack growth occurs in several distinct stages, and as a crack progresses from surface to bulk it will proceed through some or all of these stages. There are a number of factors which influence which stages will occur, and the analysis technique used will affect which ones can be detected. In Figure 3.45 for example, there appear to be two separate stages of crack growth visible; linear fracture, perpendicular to the loading direction; and crystallographic orientation controlled growth. The former could be coincidental however, if the cracked grains have their c-axes parallel to the surface, then this region may simply be fracturing along the preferential plane. The latter is also ambiguous, as the degree of slip cannot be ascertained, meaning that the fracture may be proceeding in an entirely faceted manner, or with the assistance of significant slip, which represent two different stages of crack growth. In these cases SEM fractography of an open crack, or EBSD of the cross-section would allow positive identification and differentiation of the stages, however when only light microscopy is available then caution is clearly required to prevent false conclusions from being reached.
The factors which are thought to control the stages of growth a crack will undergo are:

- Oxygen content
- Nitrogen content
- Severity of oxygen/nitrogen gradient
- Temperature
- Crystallographic texture
- Strain rate

It is evident that prediction of the occurrence of each stage is not trivial, and if a stage occurs only over a very short distance, then its identification becomes less likely. It is beyond the scope of this thesis to create a constitutive model for the stages of crack growth in $\alpha$-case, which would require an extensive experimental programme to isolate all of the separate factors. However the identification of these stages, and under multiple sets of conditions, provides the framework required to undertake such a study, and the increased understanding that this would bring to $\alpha$-case behaviour would be of substantial benefit.

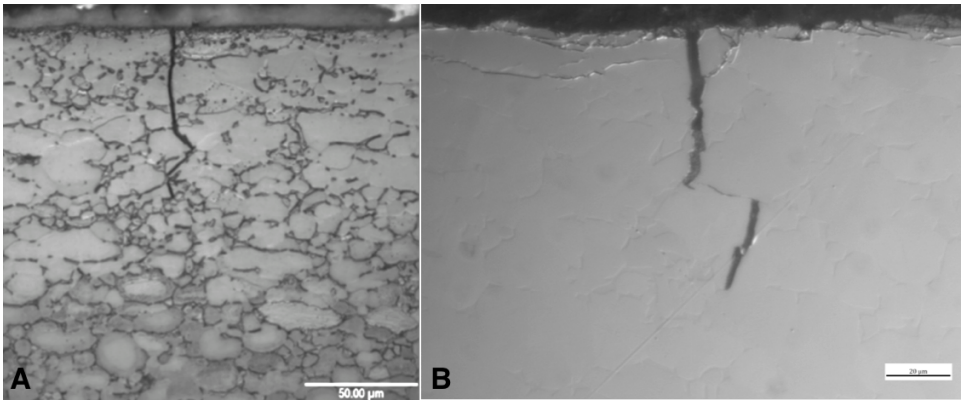


Figure 3.45: Cracks in $O_2$-stabilised $\alpha$-case showing multiple stages of crack growth. From these cross-sections under light optical microscopy, it is not possible to identify all the five possible stages of crack growth that may occur, only the initial linear stage and the second or third orientation-biased stages can be positively identified.

### 3.6.1 Crack mechanisms

There have been a number of studies of quasi-cleavage facet formation and crystal plasticity in titanium alloys in recent years [71, 72, 73, 74, 75], and the terms are generally associated with dwell fatigue. There are similarities between the reported mechanisms, and those seen in the present study however, and these will become more prominent when considering the behaviour of $\alpha$-case under fatigue loading conditions, which although beyond the scope of this study, is an important research area given the applications of titanium alloys in rotating parts. The interplay between the quasi-cleavage facets in fatigue, which are considered to result from extensive slip rather than brittle fracture [76], and the combination of brittle facets and facets with slip banding in $\alpha$-case, would produce a complex but interesting situation.
There exists visual similarity between quasi-cleavage from fatigue, and the facets with a high degree of slip observed in the present study, as seen in Figure 3.46, and despite the differences in loading regimes, the mechanisms may be comparable between the two. The presence of an oxygen or nitrogen rich layer has in some circumstances been found to be beneficial to fatigue performance [45], a phenomenon which Cassar et. al. attributed to the compressive surface stress state caused by the presence of the nitrogen-interstitials, which was not annealed out at the treatment temperature of 700℃. The triode-enhanced plasma diffusion treatment used to create the oxygen and nitrogen rich layers differs from the purely thermal process associated with normal $\alpha$-case formation, however the effect on the material is broadly similar. Such an effect would not have been expected to occur in the monotonic loading in the present study, as the applied stress would

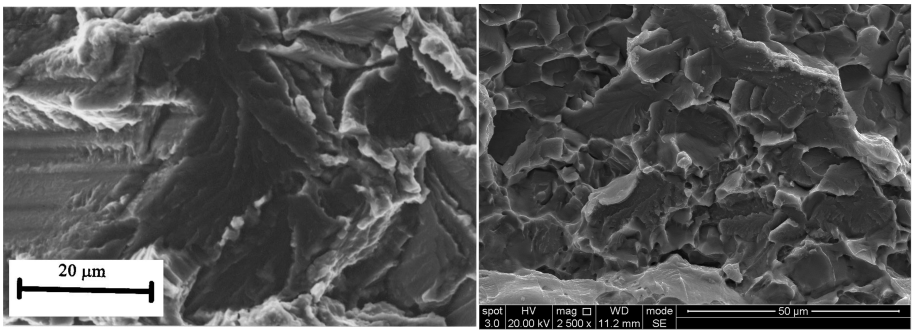


Figure 3.46: Comparison between secondary electron fractography images. Left: Quasi-cleavage facets in IMI834, as a result of separation along persistant slip planes during fatigue [72]. Right: Facets with varying degrees of slip, formed during monotonic loading of a specimen with $O_2$-stabilised $\alpha$-case.

far exceed the residual compressive stress in the material, however it is surprising that this beneficial effect of the enriched interstitials has not been observed elsewhere in studies of $\alpha$-case in fatigue. This suggests that there are more differences than expected in the behaviour of the surface between triode plasma-enhanced treated material and thermally formed $\alpha$-case, and there may therefore be some virtue in the use of the surface treatment as protection against the negative effects of $\alpha$-case. The density and integrity of the thin TiN layer which forms during triode plasma treatment may be a key difference, as it allows the layer to act as an effective barrier to oxygen diffusion, and the residual compressive stress within it resists crack initiation, thereby protecting both the substrate material, and the integrity of the layer.
Although it can be made to be beneficial, however, the presence of any form of $\alpha$-case is far more likely to be detrimental to the fatigue properties of titanium, and the risks associated with increasing the interstitial concentration at the surface are greater than the potential benefits which may be gained.

### 3.6.2 The influence of crystallographic texture on crack path

The influence of crystallographic texture on the crack growth and mechanical properties of titanium is well established [77][78], and controlling texture through processing has potential for improving the resistance against $\alpha$-case formation, and crack propagation. The latter is likely to be of greater use in industry, as it could allow $\alpha$-case tolerant materials to be designed. An example of this could be a component which, if $\alpha$-case formed, would crack with little resistance to a given depth and then be arrested, with a sufficient length to be detectable by standard NDT methods.

The effect of texture in this study was two-fold; firstly, it could influence

the ingress of oxygen and nitrogen into the material [79], and secondly, it could control the crack path as already shown. Only the latter is considered here in detail, however the effect of the former would have been a factor, albeit one that is not readily quantified due to the variation in diffusion data, as presented in Section 2.1.1. The fracture face of a unidirectionally rolled Ti-6Al-4V specimen is shown in Figure 3.47, which had an oxygen-stabilised $\alpha$-case and was tested at 400℃. The change in fracture direction visible in the top centre of the image, for a length of approximately 350 micrometres, is indicative of a macrozone - a region of adjacent grains with very similar crystallographic orientation, originating from a prior beta grain. Such features are known to influence certain types of fatigue [80, 81, 82], and the interplay between $\alpha$-case, macrozones and low-cycle fatigue would be an interesting topic for further research.
The relevance of the macrozone in Figure 3.47, however, was as evidence that the crack path through the $\alpha$-case at this point was controlled by the texture of the material, not just by the fracture mechanics.

Figure 3.48 shows a cross-section of a unidirectionally rolled specimen, with an $O_2$-stabilised $\alpha$-case, which was tensile tested at room temperature. The array of cracks that formed were seen to differ in depth, and etching the specimen revealed that the presence of a macrozone which was oriented a few degrees off-parallel to the surface was the cause of this, as it was arresting the cracks. EBSD analysis was not performed on this specimen, but it is expected that this region is oriented with the c-axis approximately perpendicular to the surface, i.e. aligned with the crack direction.

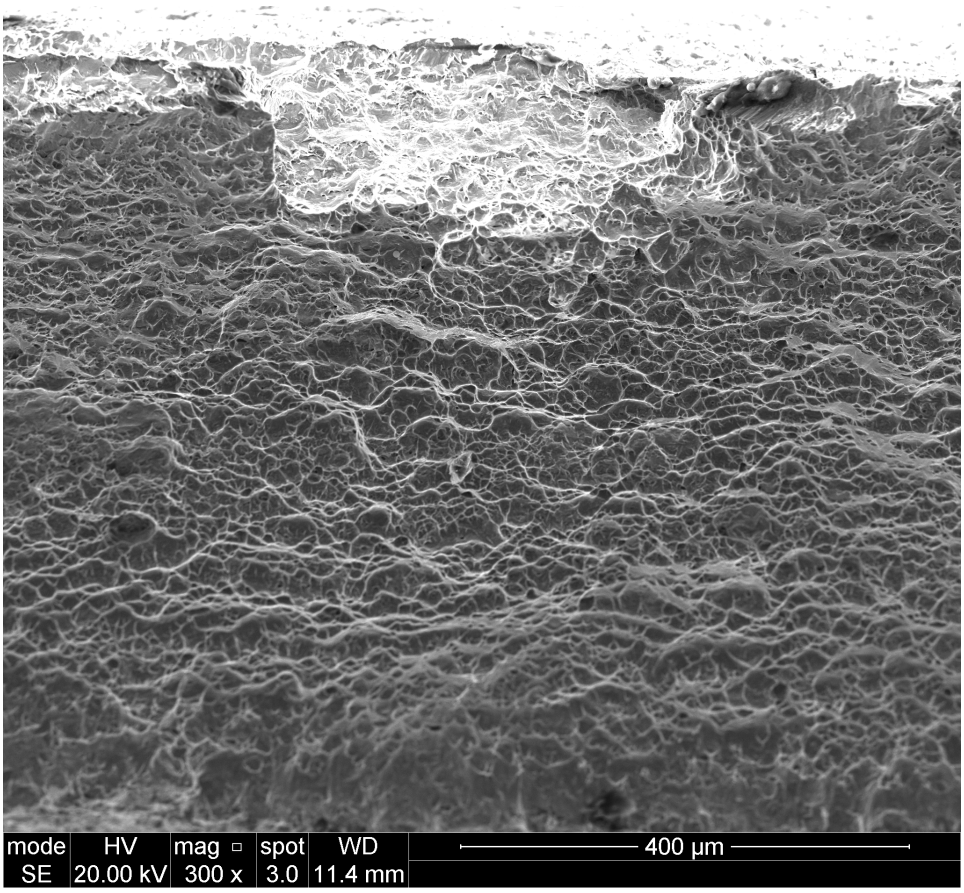


Figure 3.47: Secondary electron fractograph of specimen with oxygen-stabilised $\alpha$-case tested at 400℃. The material was unidirectonally rolled Ti-6Al-4V plate. The surface of the specimen, at the top centre of the figure, shows a region approximately 350 micrometres in length with a different fracture path, likely due to a macrozone in the material.

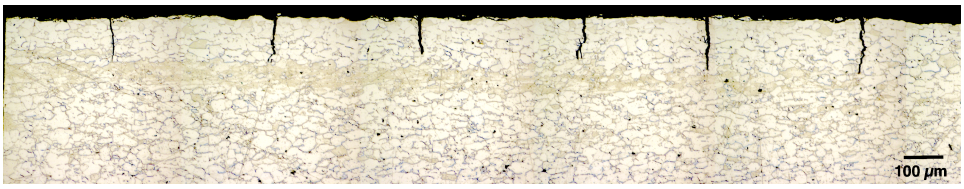


Figure 3.48: Light optical micrograph of unidirectionally rolled material with $O_2$-stabilised $\alpha$-case, tested to failure at room temperature. Etching in Kroll's reagent revealed a what appeared to be amacrozone, which can be seen to be arresting the cracks, and as the distance from the surface of this potential macrozone increases from left to right in the image, so too does the crack depth.

## 3.7 Chapter summary

The negative effects of $\alpha$ case on the tensile performance of Ti-6Al-4V have been demonstrated, with the characteristic arrays of cracks produced as per previous studies [5, 49], but under a number of different conditions. Additional aspects to the formation of the cracks have been identified, in particular the primary and secondary arrays which can occur in certain circumstances, and the depth and gradient of the $\alpha$-case have been proposed as the main determining factor in whether they will initiate in this manner. Various techniques for identifying the onset of cracking have been trialled, and digitial image correlation (DIC) with some novel adaptions has been found to be an effective method. The crack path has been investigated using light optical and electron microscopy, and three distinct stages of crack growth have been isolated, along with hybrid regions showing characteristics of more than one stage. The use of electron backscatter diffraction (EBSD) on polished cross sections has allowed analysis of the effect of crystallographic orientation on crack path, strengthening the defining attritbutes of each stage of crack growth.
The use of tensile testing as a method of detecting and quantifying $\alpha$-case depth in production parts has been proposed, as a simple and reliable technique, which will allow the minimum loss of yield.

# Chapter 4

# The formation and behaviour of $\alpha$-case under superplastic forming (SPF) conditions

## 4.1 Introduction

This project was originally envisaged to serve as a precursor to forming multi-layer sandwich structures using a 200T SPF press, in order to reduce the number of variables to be changed in that project. However as the experimental plan developed, it became apparent that the tests in the Z250 could eliminate the need for the multi-layer sandwich project entirely, since they would allow for closer control over strain, strain rate and temperature, and the relative simplicity would increase the number of tests which could be completed.

The static thermal exposures which were performed at the University of Sheffield allowed a considerable insight into the behaviour of titanium $\alpha$-case. However because part of the focus of the project was the contribution of oxygen and nitrogen ingress during the SPF process, it was necessary to understand the combined effects of interstitial absorption and superplastic deformation, and how they would influence each other. To achieve this, dynamic thermal exposures were performed; introducing oxygen or nitrogen into the system during high temperature deformation.

The intention had been to tensile test the post-forming material at room temperature, to allow a comparison of dynamically and statically formed $\alpha$-case, with a correction factor applied to account for the reduction in properties due to the temperature cycle, based on the work of Cope et. al. [84]. However it quickly became apparent that this was not practical, as many of the specimens fractured before reaching the target 0.7 strain, and the remaining specimens exhibited significant cracking, which would have caused artificially rapid failure when testing at room temperature. The focus was

therefore shifted to analysis of the flow stress during the forming, and the cracking within the formed material.
There is no data in the literature concerning the effect of SPF on the formation of $\alpha$-case, so this investigation is thought to be the first to consider it. Evans et. al. conducted a study into the effect of $\alpha$-case on creep performance of IMI834 [85], in which the specimens were exposed to air for the duration of the creep tests. Although the test regime and material are different to those in this study, some parallels may be drawn between the mechanisms, in particular for the different fracture modes which were observed depending on the applied stress. Evans found that at the higher stresses, of over 250 MPa, failure was intergranular and caused by the coalescence of cavities formed at grain boundaries, which is a common creep failure mechanism. Although surface cracks formed in the $\alpha$-case, they did not penetrate significantly beyond the visible $\alpha$-case depth of 35 $\mu$m, and were not the cause of failure. At stresses below 250 MPa, however, fracture occurred due to propagation of the surface cracks through the specimen.
The reason for these two different mechanisms occurring was proposed to be due to the difference in stress intensity factor, $K_t$; at higher stress. Once the crack had propagated beyond the visible $\alpha$-case, $K_t$ at the crack-tip was too low to allow further crack growth (due to the ductility of the material), but the stress was sufficiently high to promote cavity formation in the bulk material, causing cavitation to become the dominant mechanism. At lower stresses however, cavity formation was sufficiently sluggish to allow localised $\alpha$-case formation below the crack tip, due to the presence of air in the open crack, thereby increasing $K_t$ towards its theoretical value and allowing crack growth, which would then occur incrementally by the repeat of this mechanism.
This study also adds value to the warm tensile testing investigation in Section 3.4.1, on account of the observations on crack depth versus $\alpha$-case thickness of samples tensile tested in air at 600°C, which although at a lower temperature, may exhibit similar mechanisms. There are clear differences between the two situations, in particular the alloys (and alloy classes), and the temperature. In both cases however, the temperature was substantially (several hundred degrees Celsius) below the $\beta$ transus, so the phase proportions would have been broadly similar. Grain growth would have been more rapid in the IMI 834 than Ti-6Al-4V, on account of the higher temperature; Cassar et. al. [86] measured the grain size increase in Ti-6Al-4V as 125% after an eight hour nitiriding treatment at 800°C, and a comparable increase would be expected in the IMI 834, whereas at 600°C, negligable grain growth was measured.

Diffusion bonding is a technique regularly employed in association with superplastic forming, as SPF lends itself itself to the formation of multilayered structures, and diffusion bonding provides the optimum method for joining the sheets [14]. The fine-grained equiaxed material used for SPF is

also well-suited to diffusion bonding. There are two main techniques utilised in the process; matched metal tooling, and stop-off with external gas pressure. In the former, machined metal dies are used to apply compressive stress to the sheets being bonded, allowing diffusion to occur between them and thereby forming a homogeneous bond. The latter does not use dies, but instead the entire structure is held under external pressure by an inert gas, providing an isostatic force to cause bonding to take place. Prior to this, the regions where bonding is not desired are coated with yttrium oxide, the stop-off, which acts as a diffusion barrier between titanium surfaces and prevents bonding. This technique is generally preferred over the matched metal dies, as it is capable of achieving more consistent bonding due to the evenly applied pressure, whereas the dies are subject to the tolerances in the tooling and sheet, which can lead to regions of unsatisfactory joins. In more complex structures, a combination of the two methods may be used in order to obtain the optimum properties.
The process appears to be somewhat tolerant of an oxidised surface[87], as the conditions under bonding cause diffusion of this oxide in to the bulk, so it is not expected that $\alpha$-case would cause a particular problem if it were to occur during or prior to the process. This would also be aided by the lack of deformation occurring, and the compressive stress in the material; neither of which would lead to crack formation.
In some components, however, diffusion bonding must take place in multiple stages, some of which will occur after some superplastic forming has occurred. An example of this is shown in Figure 4.1, where bonds C and D cannot be made until the material has been formed to the final shape. Superplastic forming involves significant deformation of the material, under tensile loading, so the formation of cracks is possible at this stage of the process if $\alpha$-case is present. The typical cycle time is of the order of several hours [88], which is sufficient for substantial diffusion of oxygen into the surface to occur, should it be present, but not necessarily for it diffuse homogeneously into the bulk.

## 4.2 Experimental methods

A Zwick/Roell Z250 tensile testing machine; a floor standing, vertical rig with a 250 kN frame, was used for this set of experiments. For the SPF testing it was fitted with a Zwick/Roell Xforce HP 1 kN load cell, which had an accuracy of 0.02 % at the loads used in these tests.

### 4.2.1 Adaptation of the SPF tensile testing rig at the AFRC

As a process which uses high temperatures, low forces, and is sensitive to changes in temperature and strain rate, SPF requires particularly careful setup for testing. Issues such as the o-ring binding, as discussed in Section

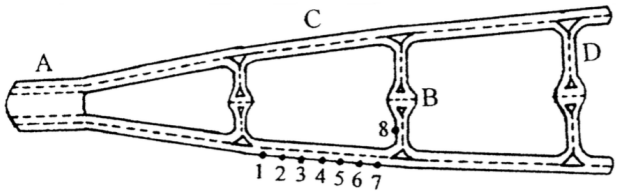


Figure 4.1: Schematic of a diffusion bonded, superplastic formed component[89]. The component would initially consist of five flat sheets, so diffusion bonding must take place in several stages to achieve the required bonds. Bonds A and B can occur whilst in this flat sheet state, but C and D require a certain degree of superplastic forming to take place before they become possible.

3.2.2, are insignificant in conventional tensile tests, as service temperatures are generally used, so stresses of several hundred MPa are typical, and strain rates are not low. In SPF however, where the peak stress may be only 25 MPa, and specimens have a small cross sectional area, a step of a few Newtons is proportionately very large. Perhaps more importantly the sudden increase in strain rate as the sample "catches up" to the crosshead is likely to have an effect on the mechanisms operating. These short term increases in strain rate can be seen in the up-slope of each step in Figure 4.2, which can be compared with the overall slope of the graph in this region. The use of a fibrous seal in place of the o-ring was successful in eliminating this problem, and was an essential modification to ensure the results were reliable.

Temperature is also particularly important in SPF, and the reasonably long test durations of approximately two hours, plus the long final length of the specimens, make furnace temperature stability a key consideration. A difference in temperature of 5℃ between one part of the gauge length and another, could be sufficient to cause more of the elongation to be localised to one area, leading to unequal deformation and earlier failure. However there are also issues with spending time to achieve stable furnace conditions before the start of each test. At the test temperature of 920℃, the oxygen or nitrogen which was stabilising the $\alpha$-case would be diffusing towards the bulk, altering the properties of the surface region, and also potentially affecting the global behaviour of the specimen, by altering the $\alpha/\beta$ phase ratio [90]. Kahveci et. al. [91] calculated the effect of oxygen on the $\beta$ transus of Ti-6Al-4V as:

$$\beta - transus(^{\circ}C) = 937^{\circ}C + 242.7 \times wt.\%\, O_2 \tag{4.1}$$

Whilst this was unavoidable during the heat-up phase and test, it was important that it was consistent between specimens. Similarly the grain growth

which was expected at this temperature needed to be comparable for all tests, since grain size is a factor in SPF behaviour [92]. For this reason, furnace temperature overshoot was also to be avoided.

The split tube furnace fitted to the Z250 was capable of achieving the required temperature stability throughout its hot-zone, which was longer than the pre-determined maximum length that any specimens would reach in these tests. This was monitored with thermocouples positioned at the upper and lower sample holders, as well as adjacent to the centre of the sample, and also at the upper and lower extremes of the hot zone which the ends of the sample would reach during the test. Independent adjustment of three regions of the furnace allowed all temperatures to be maintained within 1℃ of the nominal temperature. The furnace heat-up cycle was set to ramp at 12℃/min from RT to 880℃, 5℃/min from 880℃ to 910℃, and 2℃/min up to the 920℃ test temperature. This allowed furnace overshoot to be limited to a consistent maximum of 1℃.

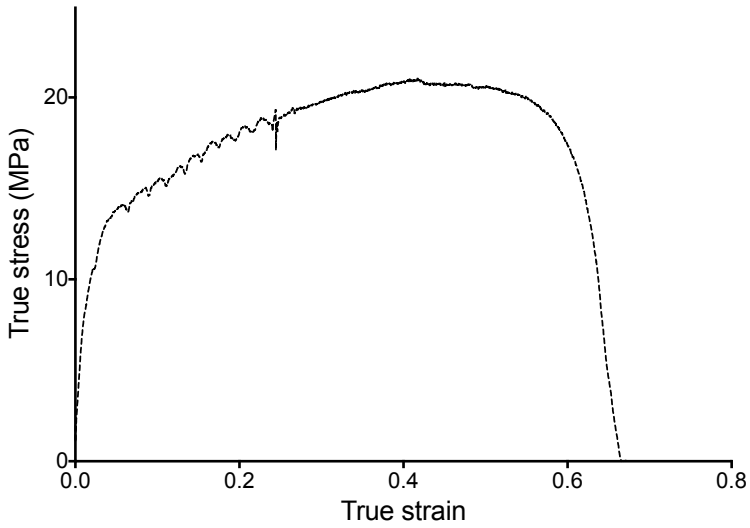


Figure 4.2: Stress strain curve from an SPF test of a specimen with $O_2$ stabilised $\alpha$-case. The retort's o-ring seal was binding, causing the steps seen in the first half of the curve. This was replaced with a fibrous seal for remaining tests, which eliminated the problem.

Three different conditions of Ti-6Al-4V were used throughout these tests; uni-directionally rolled plate (UD), cross-rolled plate (XR), and cross rolled SPF membrane, hereafter referred to simply as membrane. The UD material was supplied as plate with variable thickness, from approximately 4 mm to 10 mm, the cross rolled material supplied as a consistent thickness 20 mm plate, and the membrane as sheet with either 0.7 or 1.0 mm thickness.
The specimen geometry utilised throughout this testing, shown in Figure

3.2, was in accordance with ASTM E2448, the industry standard for uniaxial tensile testing of superplastic forming. Testing of superplastic materials provides a unique challenge in terms of specimen design; in other tensile testing set-ups, the specimen is designed such that deformation is confined to the gauge length, by making its cross section substantially smaller than that of the grips. However in SPF, the material flow from the grips cannot be avoided, as the entire specimen must be maintained at the test temperature, to avoid temperature gradients which would cloud the results, since SPF is highly temperature sensitive process. [93][94]
The inability to isolate deformation to the gauge length is mitigated by two factors; firstly, the ASTM specimen minimises variation between tests by transferring the force via the specimen shoulders, rather than clamping the surface, thereby allowing material flow to occur unimpeded, and preventing localised deformation or slip around the clamping area from being an issue. Figures 4.4 and 4.3 show a schematic of the specimen holder, and a loaded specimen, respectively. Secondly, the large deformations that occur in superplastic forming mean that the flow from the grips plays only a minor role in the overall extension, so it does not have a significant effect on the final elongation.

Figure 4.3: Specimen under test, with only the gauge visible. The two plates do not clamp the specimen, they only prevent it from falling out of the holder. All force is transferred through the specimen shoulders.

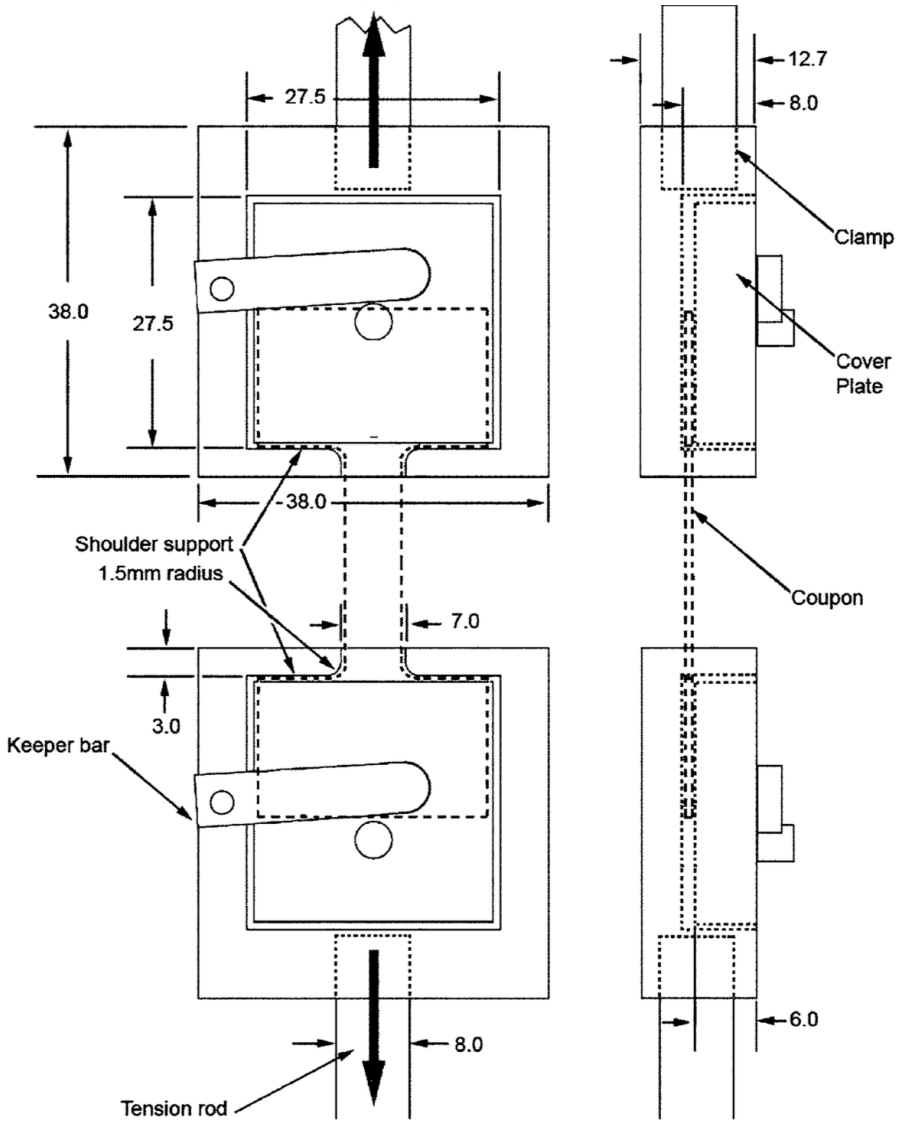


Figure 4.4: Clamping mechanism for ASTM E2448 specimens. The force is transferred only through the shoulders of the specimen, not through clamping on the faces, so that material flow from the grip is not inhibited. Schematic by Comley [95].

## 4.3 Results and discussion

### 4.3.1 Analysis of the effect of introducing oxygen or nitrogen to virgin Ti-6Al-4V during the SPF process

When considering the possibility of $\alpha$-case forming through gas contamination during the SPF process, it cannot be assumed that the formation mechanism will be the same as under static conditions. The lattice rotation and grain boundary sliding will affect the diffusion paths for the interstitial elements, and the deformation may cause repeated fracture of the oxide or nitride layer.

The stress-strain curves from the SPF testing are shown in Figures 4.5, 4.7 and 4.11. These values were calculated from the output load and displacement data from the Z250 tensile testing rig, and were converted to true stress and true strain, which are the most appropriate measures for SPF testing, where sample elongation is substantial, but deformation is uniform. Due to the relatively long duration of these tests, it was not possible to perform repeats for most conditions, as this would have limited the number of variables which could be tested, and therefore limited the analysis which could be performed. Verification of the test results would be advisable to increase confidence in them, as this is a novel area of research, and there is no existing test data to serve as a comparison. When repeats were required however, due to a suspected equipment malfunction, the results of the repeat test matched those of the original relatively closely, as can be seen from Figure 4.5. Three test specimens are shown in Figure 4.6; the top image is a UD plate specimen as a reference of the initial condition before SPF. This particular specimen was not tested, on account of a machine malfunction when it was being sectioned from plate by EDM, leading to the transverse marks that can be seen in the image, and small areas of residual recast layer, which were not removed by the pickling process on account of the increased local thickness. The specimen in the centre was tested in an atmosphere of 5 % $O_2$, but suffered fracture before reaching the target strain of 0.7; it can be seen from Figure 4.7 that it failed at a strain of 0.62.

Figure 4.8 shows the cross section of this specimen, which exhibited a regular array of fine, deep cracks, between 30 and 70 $\mu$m in depth. In comparison to the final specimen thickness of 440 $\mu$m, this crack length is a significant proportion, especially considering that the cracks were forming from both sides of the specimen. This will have substantially increased the stress intensity factor at the crack tip, in addition to making the calculation of the stress an underestimate. Ideally the flow stress curves would have been adjusted to account for this 30 % decrease in effective thickness, however this approach has two key difficulties associated with it:

1. It was not known at which stage of the test the cracks initiated, and nor was the rate of propagation known. The only known value was

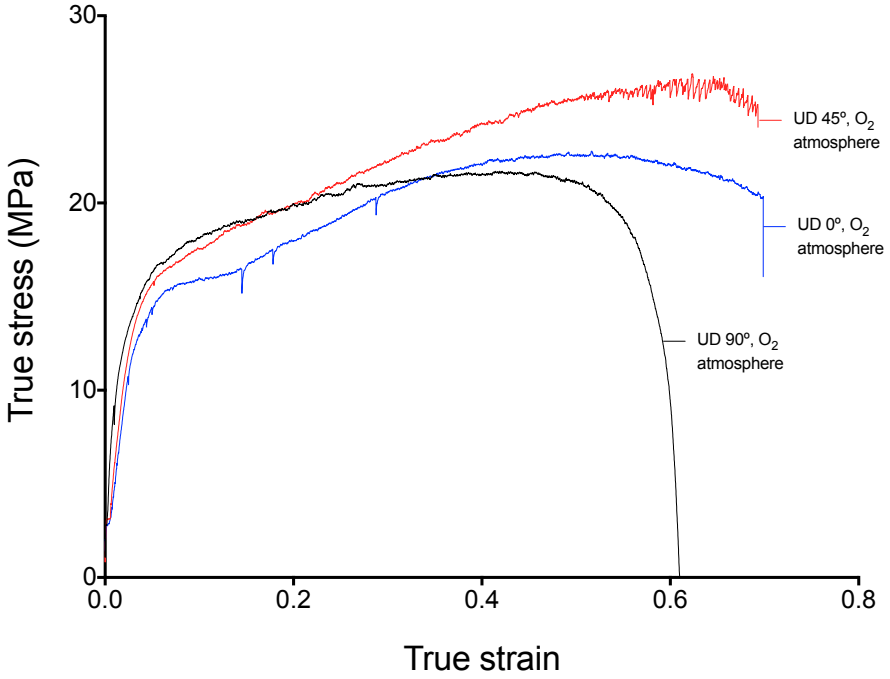


Figure 4.5: Stress strain curves for two pairs of Ti-6Al-4V UD specimens tested at a constant true strain rate of $1x10^{-4}$ $s^{-1}$ at 920°C. Tests 15 and 17 experienced minor equipment malfunctions, which can be identified by the spikes in the graph, and so were repeated in tests 16 and 18 respectively. The repeated tests matched the results from the initial test closely, with the exception of the fracture of Specimen 15, thought to be due to the early spike in load.

the final crack depth, however if this value was used for the entire test then it would most likely overestimate the stress for a substantial proportion of the test. Live measurement of the crack depth, via acoustic emissions monitoring [96] for instance, could provide a solution to this problem in future.

2. The crack front was unlikely to be consistent across the width of the specimen. Many cracks which have been analysed from the surface were found to be discontinuous across the width of the specimen, and those that extend across the entire specimen are unlikely to have reached a constant depth for the full extent.

The flow stress values were therefore not altered to correct for the crack length, and as such the values reported for specimens with longer cracks will be understated, for at least a portion of the curve. Repeating these experiments with thicker specimens, so that the ratio of anticipated crack

length to sample thickness does not exceed 0.1, would eliminate the effect of the increase in $K_{IC}$, and diminish the impact of the reduced cross section on stress calculations.

The specimen shown at the bottom of Figure 4.6 was tested using the same parameters as Specimen 19, except the atmosphere was 5 % $N_2$ rather than $O_2$. The target strain was reached, and the shape of the curve in Figure 4.7(Specimen 20) indicated that failure was not imminent at the point the test was ended. Analysis of the cross section, shown in Figure 4.9, revealed an array of cracks, but these were typically 20 - 25 $\mu$m in depth, and spaced an average of 350 $\mu$m apart; significantly shorter and more widely spaced than those in Specimen 19. This suggests that the effect of nitrogen in the SPF process is less deleterious than oxygen, although both will cause crack formation and therefore ultimately failure. A comparison of the

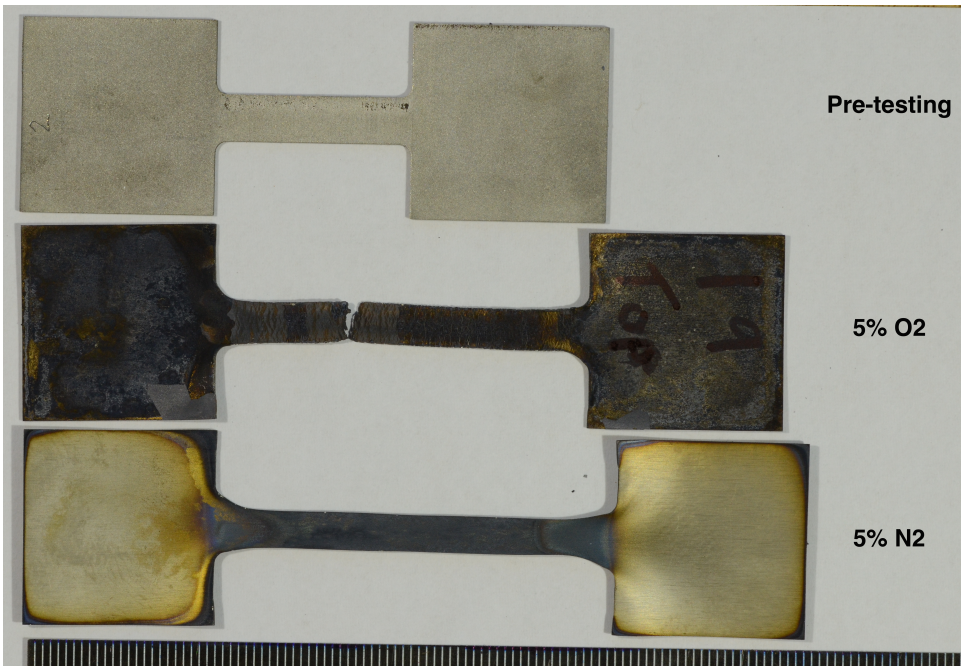


Figure 4.6: Three Ti-6Al-4V membrane SPF test specimens. Top: Specimen prior to testing, in the as-received condition. Centre: Specimen tested in an atmosphere containing 5 % $O_2$, which fractured before reaching the target of 0.7 true strain. Bottom: Specimen tested in an atmosphere containing 5 % $N_2$, which reached the target strain of 0.7.

unidirectionally rolled specimens' flow curves is illustrated in Figure 4.11; all specimens were tested in the as-received condition in an atmosphere of 5 % $O_2$.
All three orientations exhibited similar flow stress, with the longitudinal

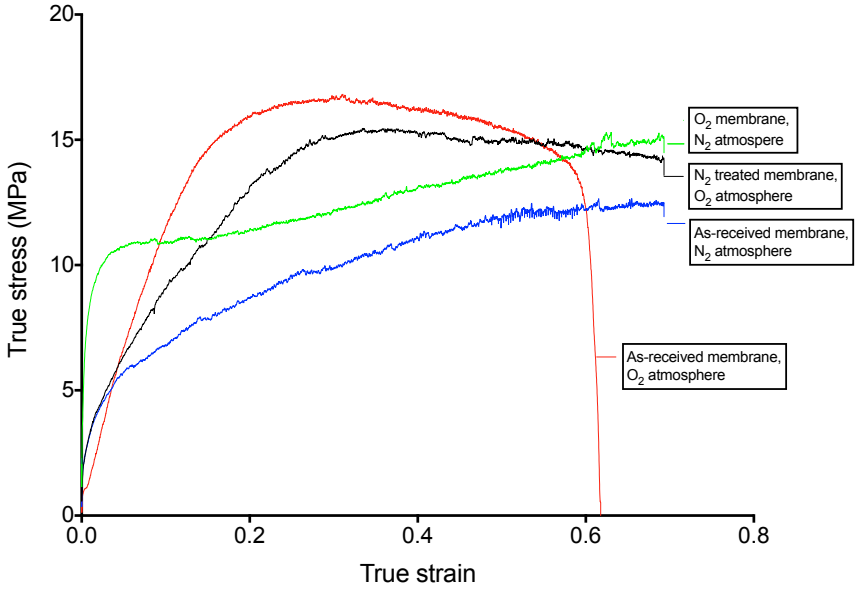


Figure 4.7: Stress strain curves for four Ti-6Al-4V membrane specimens tested at a constant true strain rate of $1x10^{-4}$ $s^{-1}$ at 920°C. Specimens 21 and 22 were pre-treated to respectively form an $N_2$-stabilised and $O_2$-stabilised $\alpha$-case prior to SPF testing. Specimen 19 fractured before reaching the target strain of 0.7.

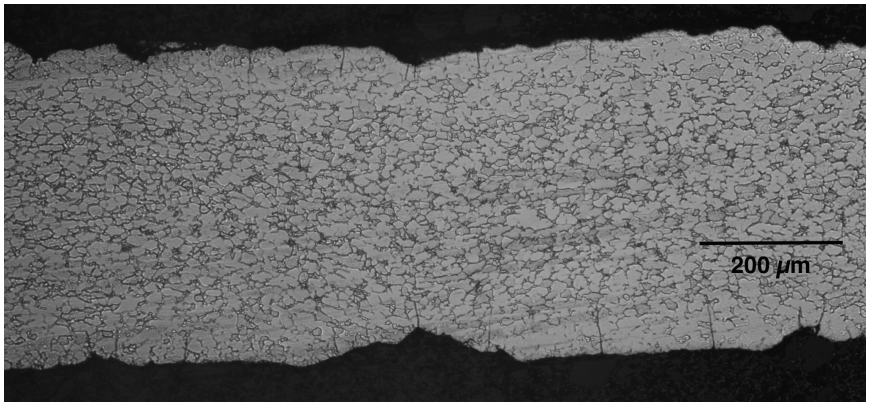


Figure 4.8: Light optical micrograph of Ti-6Al-4V membrane specimen 19, tested at a constant true strain rate of $1x10^{-4}$ $s^{-1}$ at 920°C in $O_2$. This specimen fractured before reaching the target strain of 0.7, and exhibited a regular array of fine cracks between 30 and 70 $\mu$m in depth.

(0°) specimen being slightly lower, although this was thought to have been affected by a minor malfunction in the equipment, which caused the spikes visible in the flow stress curve. The flow curve of the transverse (90°) speci-

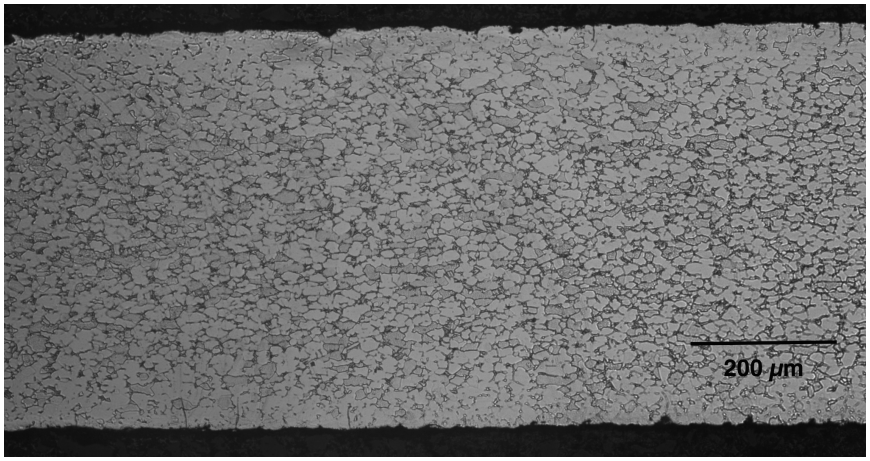


Figure 4.9: Light optical micrograph of Ti-6Al-4V membrane specimen 20, tested at a constant true strain rate of 1x10$^{-4}$ s$^{-1}$ at 920°C in $N_2$. This specimen reached the target strain of 0.7 without fracture, and exhibited a widely spaced regular array of fine cracks between 20 and 25 $\mu$m in depth.

men began to deviate after approximately 0.2 strain, as the rate of increase of stress reduced compared to the other two specimens. This may have been due to some degree of necking occurring in the specimen, which does not generally occur in SPF-grade Ti-6Al-4V, or the gradual propagation of a crack. Subsequent examination of the specimen favoured the latter explanation, as no significant necking could be identified, as can be seen from Figure 4.10. The micrographs for the three specimens showed similar crack depths of approximately 40 - 50 $\mu$m, with no readily discernible effect from the different orientations.

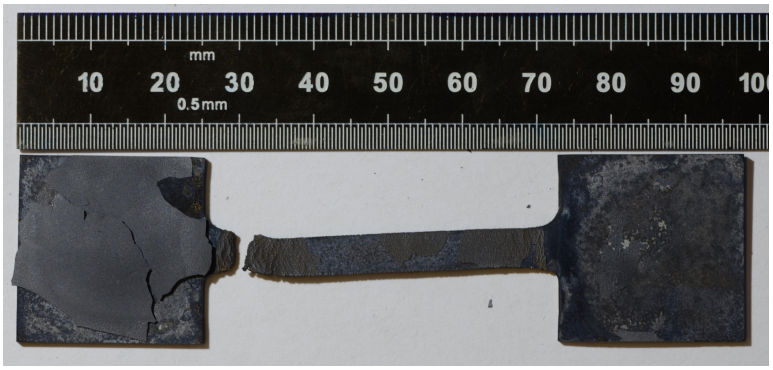


Figure 4.10: Photograph of Ti-6Al-4V UD 90° specimen 18, tested at a constant true strain rate of 1x10$^{-4}$ s$^{-1}$ at 920°C in $O_2$. This specimen began to show a decreased rate of increase in flow stress from 0.2 strain, and fractured at 0.6 strain. No significant necking can be seen in the specimen.

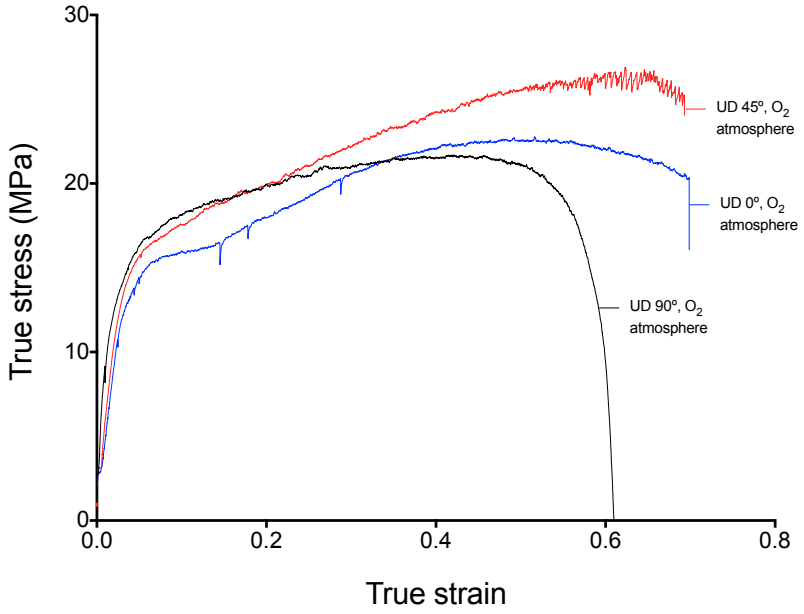


Figure 4.11: Stress strain curves for three Ti-6Al-4V UD specimens; longitudinal (0°), transverse (90°) and 45°, tested at a constant true strain rate of $1x10^{-4}$ $s^{-1}$ at 920℃. Specimen 18 fractured before reaching the target strain of 0.7.

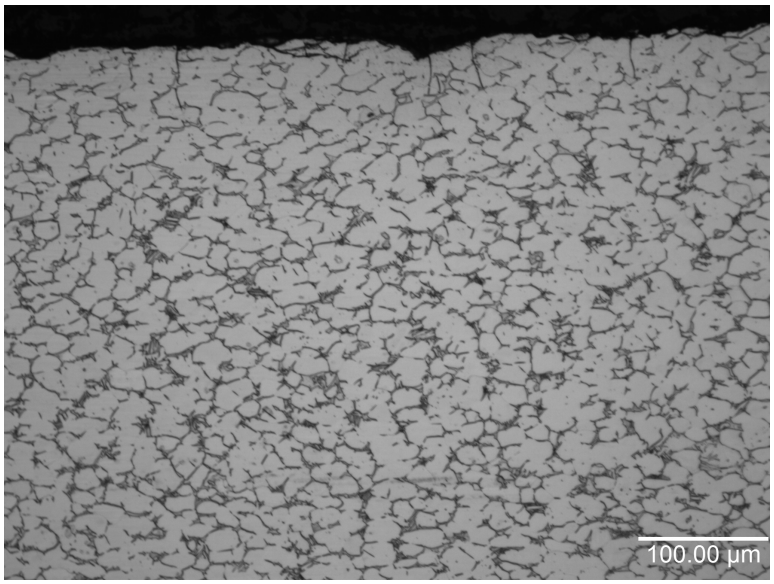


Figure 4.12: Light optical micrograph of Ti-6Al-4V UD 0° specimen 13, tested at a constant true strain rate of $1x10^{-4}$ $s^{-1}$ at 920℃ in $O_2$. This specimen reached the target strain of 0.7 without fracture, and exhibited a regularly spaced regular array of fine cracks between 35 and 50 $\mu$m in depth.

### 4.3.2 Analysis of the effect of pre-existing $\alpha$-case on the SPF process

The flow curve for Test 21, in Figure 4.7, shows the effect of a pre-existing $N_2$-stabilised $\alpha$-case on the process. When this was compared to Test 20, an as-received specimen tested in a nitrogen atmosphere, the early stages of deformation up to 0.02 strain were identical between the two specimens. This suggested that any effect which the pre-existing $\alpha$-case was having on the flow stress was very localised to the surface of the specimen, and therefore under deformation the as-received specimen rapidly reached the same state.

Beyond this point, however, the as-received specimen's flow stress began to level off, whilst Test 21 continued to increase at a high rate, with the oxygen atmosphere apparently becoming more significant than the pre-existing $\alpha$-case. The peak stress was more comparable to the as-received specimen tested in oxygen than nitrogen, implying that it was the oxygen atmosphere that had a greater influence than the nitrogen in the original $\alpha$-case. One major difference was that Test 21 did not fracture, however, whilst Test 19 failed at a strain of 0.61, which suggests that the nitrogen may have been inhibiting the ingress of oxygen and limiting the effective $\alpha$-case depth. The cross-section in Figure 4.13 added some weight to this theory, as the array of cracks was more similar to specimens exposed only to nitrogen atmospheres, than it was to those exposed to oxygen. Conversely Test 22, which had a

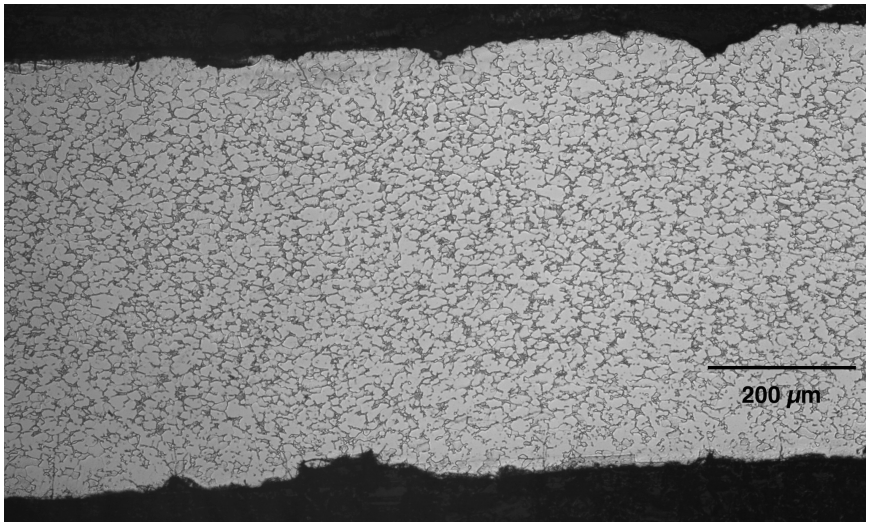


Figure 4.13: Light optical micrograph of Ti-6Al-4V UD 90° specimen 21, tested at a constant true strain rate of $1x10^{-4}$ $s^{-1}$ at 920°C in $O_2$. This specimen had a pre-formed $N_2$-stabilised $\alpha$-case, and whilst its flow behaviour was similar to specimens exposed only to oxygen during SPF, the crack formation was more comparable to those exposed to nitrogen.

pre-existing $O_2$-stabilised $\alpha$-case and was SPF tested under nitrogen, initially showed flow behaviour comparable to the as-received specimen tested in oxygen, but at a strain of 0.05 began to level off and more closely match the slope of the test conducted in nitrogen. Examination of the cross-section revealed that it had not formed any cracks, which differentiated it from the other specimens in this set of tests.

### 4.3.3 The influence of oxygen and nitrogen on the flow stress of SPF-grade Ti-6Al-4V

It had been anticipated that the presence of $\alpha$-case would have an effect on the flow stress during SPF, on account of the increased concentration of $\alpha$-stabilising elements in the specimen, and therefore the reduced proportion of $\beta$-phase, which is known to promote lower flow stress in SPF [92]. However what hadn't been expected was the immediacy of the change in flow stress when oxygen or nitrogen was introduced during the process.

The test durations were approximately 120 minutes, and the atmospheres were switched at the mid-point by simultaneously closing one regulator and opening another. The furnace was not purged with a separate gas when switching, since it was taking place during an active test, and this would add an additional variable. Figure 4.14 illustrates the effect that altering the SPF atmosphere has on the flow stress of virgin Ti-6Al-4V. It can be seen that upon switching the atmosphere, the material began to respond within approximately 30 seconds, with a sudden decrease in flow stress when switching to oxygen, followed 60 - 120 seconds later by a change to a steep positive gradient, which was maintained for several minutes. The inverse occurred when switching from oxygen to nitrogen. There were therefore two main points of interest on the flow stress curves: the small (approximately 1 - 1.5 MPa) peak or trough immediately after the atmosphere was switched, and the longer, larger magnitude (6 - 8 MPa) increase or decrease in flow stress following this.

One potential culprit for these observations was a change in temperature, since this could have occurred when introducing a different atmosphere, and would have had an effect on the flow stress. Analysis of the thermocouple readings from three areas of the samples showed a variation of less than 1.5°C throughout the entire duration of each test, however, and with no sudden changes at the point of introducing the second atmosphere. An example of one of the thermocouple traces can be seen at the top of Figure 4.15. Temperature variation could therefore be eliminated as a possible cause of the change in flow stress.

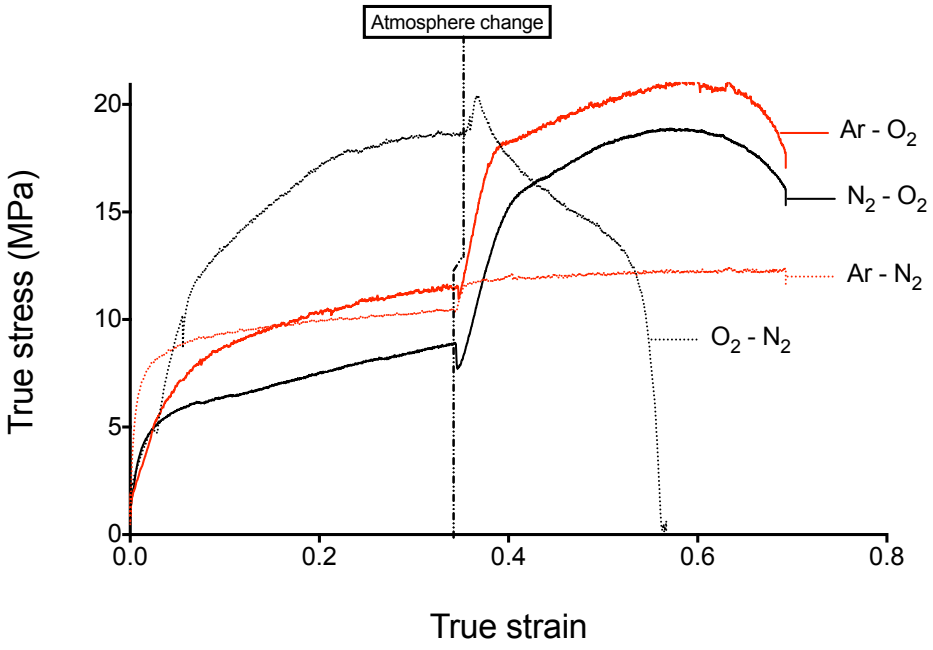


Figure 4.14: Stress strain curve from four SPF tests on specimens with no pre-existing $\alpha$-case. The test atmosphere was changed mid-way through the test, and had an almost immediate effect on the flow stress. Sample temperature was monitored by thermocouples throughout and did not change by more than 1℃.

Figure 4.15 further demonstrates the effect that introducing nitrogen or oxygen to the atmosphere during SPF can have on the flow stress of Ti-6Al-4V. A similar phenomenon has been observed by Shaoqing et. al. [97], who identified a pronounced reduction in flow stress of Ti-6Al-4V when it was exposed to hydrogen. Hydrogen is a $\beta$-stabiliser, and it was suggested that the large increase in $\beta$-phase was partly responsible for the drop in flow stress, but also that the presence of hydrogen allowed pinned dislocations to be released, reducing the number of grains with high dislocation density. The optimum hydrogen concentration for this effect to occur was between 0.1 wt.% and 0.17 wt.%. Since oxygen and nitrogen are $\alpha$-stabilisers, the mechanism will not be the same, but it is possible that with oxygen in particular, the reverse is occurring, causing the observed increase in flow stress. The relatively low concentrations of hydrogen required to have a notable effect would allow for the short timescales observed for the change, although there is nothing to suggest that the concentrations of oxygen or nitrogen necessary to have an effect of similar magnitude would be similar.

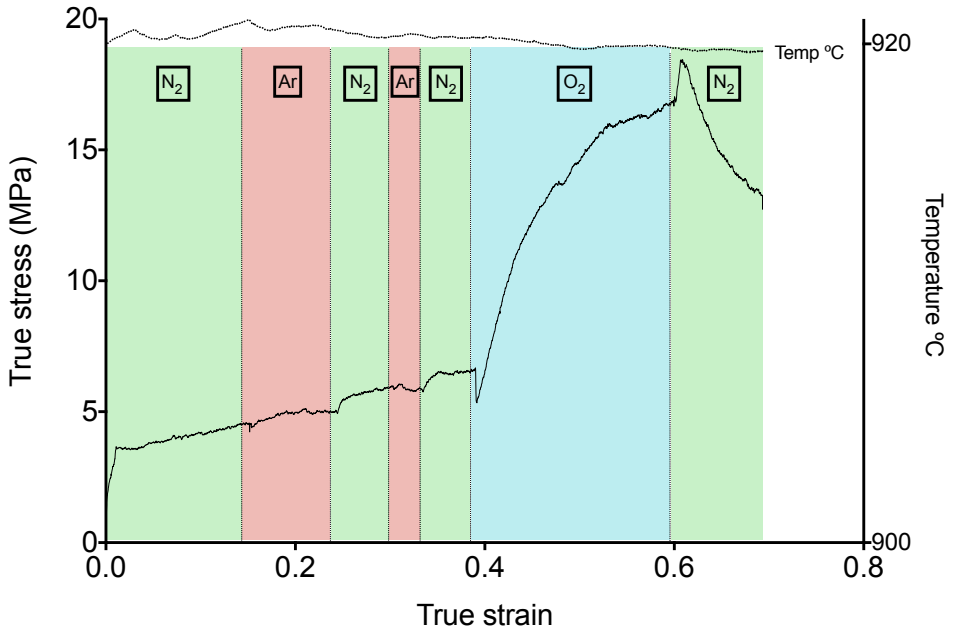


Figure 4.15: Stress strain curve from an SPF test of a specimen with no pre-existing $\alpha$-case. The test atmosphere was changed multiple times throughout the duration of the test, with a pronounced effect on the material's flow stress within 30 seconds of switching the gas.

## 4.4 Chapter summary

The SPF testing programme provided valuable insight in to the effects that oxygen and nitrogen can have on Ti-6Al-4V under superplastic forming conditions, both in the case where the inert gas is contaminated during the process, and where the material has pre-existing $\alpha$-case. Although many new questions have been raised, the following conclusions can be drawn:

- The flow stress during the SPF process was highly dependant on the atmosphere. An oxygen-containing atmosphere caused the flow stress to increase compared to argon, whilst a nitrogen containing atmosphere caused it to remain largely similar to argon, or even decrease.
- The effect of atmosphere on the flow stress was very rapid, of the order of approximately 30 seconds from the atmosphere being switched to the change in flow stress being observed. It is not thought that significant diffusion can occur in this time period, so the mechanism is currently unclear.
- $\alpha$-case formed cracks during the SPF process, despite the high ductility of the material at 920℃, although it was not possible to determine whether these cracks formed during SPF or the cooldown period. This could be determined by conducting a test under the same conditions, but after the cooldown period had concluded, raising the system back up to temperature and continuing the test. If the cracks had not formed or developed during the cooldown, it may be expected that the load/displacement curve would continue from the end of the previous test.
- Material which had $\alpha$-case formed prior to SPF, appeared to perform better than the as-received material, when subjected to SPF in an oxygen or nitrogen containing atmosphere, in terms of resistance to fracture and formation of regular cracks. Since the mechanism by which the atmosphere affects SPF is not yet known, the relationship between the atmosphere and material condition cannot be readily postulated.

# Chapter 5

# Conclusions and recommendations for further work

## 5.1 Conclusions

A research programme to better understand the effects of $\alpha$-case in titanium has been undertaken, with a focus on the diffusion bonding - superplastic forming process, and the behaviour under tension. The material used throughout the study was fine-grained Ti-6Al-4V, but the principles would be expected to apply to other $\alpha+\beta$ alloys also. The key outcomes of this research are as follows:

- The measurement of $\alpha$-case thickness is highly dependant on the measurement technique used. Microscopy of etched cross-sections and hardness profiles give substantially different results, with hardness profiling always suggesting a greater affected depth.
- The concept of a "effective" $\alpha$-case depth definition has been proposed, which determines the depth to which $\alpha$-case will have a detrimental effect on the material. This is a context-dependant definition, as a material used exclusively at elevated temperature will be able to tolerate a greater degree of interstitial-enrichment than one used at room temperature. The suggested method for determining the depth is to tensile test a sacrificial specimen to failure, at elevated temperature if appropriate to the context, and either measure the crack depth in cross section or analyse the fracture face.
- Both oxygen and nitrogen have been found to readily form $\alpha$-case, and the properties of each are subtly different. Under tension, both will form regular arrays of surface cracks orthogonal to the loading direction, and the cracks in nitrogen-stabilised $\alpha$-case tend to be shorter

and more closely spaced. Primary and secondary arrays of cracks have been found to occur, with the latter bisecting the former to accommodate increasing levels of strain.

- Multiple stages of crack growth in $\alpha$-case under monotonic tensile loading have been identified by microscopy and EBSD. The crack initiation appears to be independent of crystallographic orientation, whereas later stages of propagation tended to preferentially occur along the basal plane as the oxygen or nitrogen concentration decreased.
- SEM fractography revealed faceted crack growth in the near-surface regions of the $\alpha$-case, with an increasing level of slip evident as the crack proceeded towards the bulk.
- Thermal gravimetric analysis revealed distinct differences in the absorption rates between oxygen and nitrogen, and when the two atmospheres were applied consecutively, the order was important, as the first atmosphere affected the absorption of the second.
- The presence of oxygen or nitrogen in the atmosphere during SPF caused $\alpha$-case to form, and in some cases with an oxygen atmosphere, fracture of the specimen at a true strain of approximately 0.6. The majority of samples formed arrays of cracks in the $\alpha$-case.
- $\alpha$-case was formed on specimens which were subsequently SPF tested in atmospheres containing oxygen or nitrogen. It was found that these specimens were less susceptible to cracking and failure during SPF, than those without pre-existing $\alpha$-case.
- Introducing oxygen or nitrogen into the SPF atmosphere was found to cause a rapid change in flow stress. The mechanism behind this is not yet clear.

## 5.2 Recommendations for further work

There have been many new questions raised during the course of this research, and whilst the project was deliberately dynamic to allow as many of these as possible to be investigated, some were beyond the scope of what could be achieved.
One key area which requires clarification is the combined effects of oxygen and nitrogen, as the results from TGA, monotonic tensile testing, SPF testing and microstructural analysis, have all contributed to the understanding of how they interact, but some form of quantitative analysis is required to fully explain the mechanisms and develop a model. The most promising candidate for this is dynamic secondary ion spectrometry (D-SIMS), which with the use of calibrated standards, can produce a quantitative map of

the nitrogen and oxygen concentration with respect to distance below the surface, and example of which is shown in Figure 5.1. This is achieved by sputtering away material in multiple regions of a cross-sectioned sample, corresponding to various depths from the surface, and analysing the secondary ions which are produced using mass spectrometry. The spatial and chemical resolution of the technique is sufficient to accurately identify the extent of $\alpha$-case, whether stabilised by oxygen or nitrogen, and it is expected that it could provide some of the insight required to understand the interaction between the two stabilising elements.

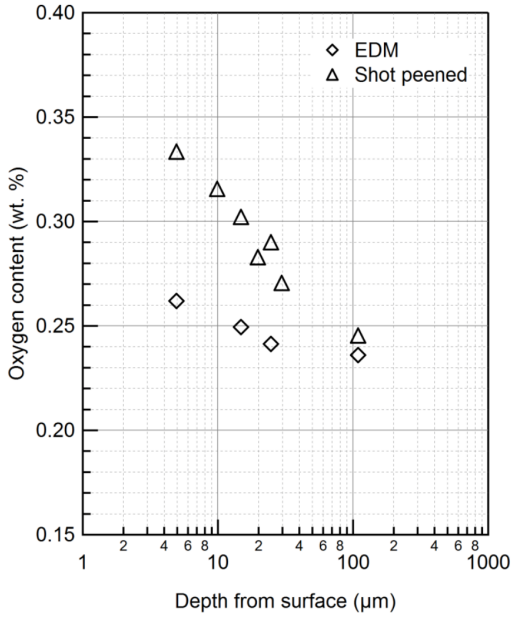


Figure 5.1: Oxygen concentration profiles of titanium alloy Ti-834, produced with dynamic secondary ion mass spectrometry (D-SIMS) [98].

Rutherford backscattering spectroscopy (RBS) might also provide useful information on the sub-surface composition, if used similarly to D-SIMS for measuring the chemistry at various points on a cross-section, however a better utilisation would be the analysis of surface oxide and nitride layers, which otherwise would be difficult to distinguish. The high sensitivity of the technique could allow identification of the various layers present on the surface of the titanium, information which would help to explain the combined ingress rates of oxygen and nitrogen.

The effect of atmosphere composition on flow stress during SPF has the potential to become a significant research project, and could potentially be utilised as a practical technique to tailor the SPF process in certain applications, or detect the effects of oxygen or nitrogen contamination during

forming from analysis of localised heterogeneous deformation. A comprehensive study, perhaps combined with quantitative chemical profiling with D-SIMS, would provide fascinating information on the process.

The final area which particularly merits further research is the mechanisms of crack initiation and growth, in particular the point at which each stage occurs with respect to strain. The interrupted tensile testing provided some useful insight into this, however it could only ever provide limited "strain resolution". Continuous monitoring of the crack behaviour during tensile testing would allow the stages of initiation and growth to be captured in far more detail, with the use of an SEM with in-situ tensile testing capabilities. This could be achieved by exposing the tensile specimens to form the $\alpha$ case, and then polishing a side face of the sample. This would provide a cross-sectional view, similar to those presented in this thesis, through which it may be possible to capture the various stages of crack growth when tensile tested in the SEM. This would aid the understanding of the mechanisms operating in $\alpha$-case under tension, allowing improved modelling of its effect on the material in various operating conditions.

# Bibliography


[1] R. G. Dobeson, S. D. McDonald, and M. S. Dargusch. Determination of minimum machining depth after heat treatment of ASTM Grade 2 titanium alloy. *Advanced Engineering Materials*, 14(7):473–476, 7 2012.

[2] K. S. Chan, M. Koike, B. W. Johnson, and T. Okabe. Modeling of -$\alpha$-case formation and its effects on the mechanical properties of titanium alloy castings. *Metallurgical and Materials Transactions A*, 39(1):171–180, 1 2008.

[3] R. Gaddam, B. Sefer, R. Pederson, and M. L. Antti. Study of $\alpha$-case depth in Ti-6Al-2Sn-4Zr-2Mo and Ti-6Al-4V. In *IOP Conference Series: Materials Science and Engineering*, volume 48, page 012002. IOP Publishing, 2013.

[4] D Jordan. Study of -$\alpha$ case formation on heat treated Ti-6Al-4V alloy. *Heat Treating Progress*, 8(3):45, 2008.

[5] A. L. Pilchak, W. J. Porter, and R. John. Room temperature fracture processes of a near-$\alpha$ titanium alloy following elevated temperature exposure. *Journal of Materials Science*, 47(20):7235–7253, 7 2012.

[6] D. P. Satko, J. B. Shaffer, J. S. Tiley, S. L. Semiatin, A. L. Pilchak, S. R. Kalidindi, Y. Kosaka, M. G. Glavicic, and A. A. Salem. Effect of microstructure on oxygen rich layer evolution and its impact on fatigue life during high-temperature application of $\alpha/\beta$ titanium. *Acta Materialia*, 107:377–389, 2016.

[7] SAE International. AMS 2642E - structural examination of titanium alloys etch-anodize inspection procedure, 02 2016.

[8] G. Cassar, J. C. Avelar-Batista Wilson, S. Banfield, J. Housden, A. Matthews, and A. Leyland. Surface modification of Ti-6Al-4V alloys using triode plasma oxidation treatments. *Surface and Coatings Technology*, 206(22):4553–4561, 6 2012.

[9] Simon Zabler. Interstitial oxygen diffusion hardening a practical route for the surface protection of titanium. *Materials Characterization*, 62(12):1205–1213, 2011.

[10] I. Gurrappa and A. K. Gogia. High performance coatings for titanium alloys to protect against oxidation. *Surface and Coatings Technology*, 139(2):216–221, 2001.

[11] Cunzhen Yu, Shenglong Zhu, Dezhou Wei, and Fuhui Wang. Amorphous sol–gel $SiO_2$ film for protection of Ti6Al4V alloy against high temperature oxidation. *Surface and Coatings Technology*, 201(12):5967–5972, 2007.

[12] H. L. Du, P. K. Datta, J. S. Burnell-Gray, and D.B. Lewis. Effect of Nb coating on the sulphidation/oxidation behaviour of Ti and Ti-6Al-4V alloy. *Journal of Materials Science*, 30(10):2640–2647, 1995.

[13] S. N. Patankar, Y. T. Kwang, and T. M. Jen. $\alpha$-casing and superplastic behavior of Ti-6Al-4V. *Journal of Materials Processing Technology*, 112(1):24–28, 2001.

[14] L. D. Hefti. Advances in fabricating superplastically formed and diffusion bonded components for aerospace structures. *Journal of Materials Engineering and Performance*, 13(6):678–682, 2004.

[15] A. J. McEvily. Failures in inspection procedures: case studies. *Engineering Failure Analysis*, 11(2):167–176, 2004.

[16] T Uihlein and H Schiegel. Titanium fire in jet engines. pages 25–1 – 25–12.

[17] David Rugg, Mark Dixon, and Justin Burrows. High-temperature application of titanium alloys in gas turbines. material life cycle opportunities and threats–an industrial perspective. *Materials at High Temperatures*, 33(4-5):536–541, 2016.

[18] R. R. Boyer. An overview on the use of titanium in the aerospace industry. *Materials Science and Engineering: A*, 213(1):103–114, 1996.

[19] P. Kofstad, K. Hauffe, and H. Kjollesdal. Investigation on the oxidation mechanism of titanium. *Acta Chemica Scandinavica*, 12(2):239–266, 1958.

[20] Private communications with Dave Rugg and Mark Dixon of Rolls Royce plc.

[21] Z. Liu and G. Welsch. Literature survey on diffusivities of oxygen, aluminum, and vanadium in -$\alpha$ titanium, $\beta$ titanium, and in rutile. *Metallurgical Transactions A*, 19(4):1121–1125, 1988.

[22] K.M. Browne. Mechanical relaxation and diffusion of interstitial atoms in H.C.P. metals. *Acta Metallurgica*, 20, April 1972.

[23] TN Wittberg, J Douglas Wolf, R Gerald Keil, and Pu Sen Wang. Low-temperature oxygen diffusion in $\alpha$-titanium characterized by auger sputter profiling. *Journal of Vacuum Science & Technology A: Vacuum, Surfaces, and Films*, 1(2):475–478, 1983.

[24] D. David and G. Beranger. A study of the diffusion of oxygen in -$\alpha$-titanium oxidized in the temperature range 460℃ - 700℃. *J. Electrochem. Soc.: Solid-state Science and Technology*, (6), June.

[25] D. S. R. Krishna, Y. L. Brama, and Y. Sun. Thick rutile layer on titanium for tribological applications. *Tribology International*, 40(2):329–334, 2007.

[26] A. M. Chaze and C. Coddet. The role of nitrogen in the oxidation behaviour of titanium and some binary alloys. *Journal of the Less Common Metals*, 124(1):73–84, 1986.

[27] H. L. Du, P. K. Datta, D. B. Lewis, and J. S. Burnell-Gray. Air oxidation behaviour of Ti-6Al-4V alloy between 650℃ and 850℃. *Corrosion Science*, 36(4):631–642, 1994.

[28] G. K. J. M. Bertrand, K. Jarraya, and J. M. Chaix. Morphology of oxide scales formed on titanium. *Oxidation of Metals*, 21(1-2):1–19, 1984.

[29] J. Desmaison, P. Lefort, and M. Billy. Oxidation mechanism of titanium nitride in oxygen. *Oxidation of Metals*, 13(6):505–517, 1979.

[30] D. B. Lee, M. J. Kim, L. Chen, S. H. Bak, O. Yaskiv, I. Pohrelyuk, and V. Fedirko. Oxidation of nitride layers formed on Ti-6Al-4V alloys by gas nitriding. *Metals and Materials International*, 17(3):471–477, 6 2011.

[31] H. Okamoto. O-Ti (oxygen-titanium). *Journal of Phase Equilibria and Diffusion*, 32(5):473–474, 2011.

[32] *Alloy Phase Diagrams, ASM Handbook*, volume 3. ASM International, 2016.

[33] J.W. Rogers Jr., K.L. Erickson, and D.N. Belton. Low temperature diffusion of oxygen in titanium and titanium oxide films. *Applied Surface Science*, 35:137–152, 1988-89.

[34] R. Dobeson, N. Petrazoller, M. Dargusch, and S. McDonald. Effect of thermal exposure on the room temperature tensile properties of Grade 2 titanium. *Materials Science and Engineering: A*, 528(10):3925–3929, 2011.

[35] R. A. Brockman, A. L. Pilchak, W. John Porter, and R. John. Estimation of grain boundary diffusivity in near-$\alpha$ titanium polycrystals. *Scripta Materialia*, 65(6):513–515, 9 2011.

[36] W. Yan and X. X. Wang. Surface hardening of titanium by thermal oxidation. *Journal of Materials Science*, 39(16):5583–5585, 2004.

[37] W. J. Boettinger, M. E. Williams, S. R. Coriell, U. R. Kattner, and B. A. Mueller. $\alpha$ case thickness modeling in investment castings. *Metallurgical and Materials Transactions B*, 31(6):1419–1427, 2000.

[38] M. Koike, D. Jacobson, K. Kwai, and T. Okabe. Grindability of $\alpha$-case formed on cast titanium. *Dental Materials Journal*, 28(5):587–594, 2009.

[39] C. Schuman, E. Lenarduzzi, S Weber, M-J. Philippe, D. Petelot, and P. Bounie. Modelling the oxygen diffusion profile in TA3V and T40 during heat-treatment under air between 620℃ and 850℃. *Surface and Coatings Technology*, 200(14):4572–4578, 2006.

[40] H. Conrad. Effect of interstitial solutes on the strength and ductility of titanium. *Progress in Materials Science*, 26(2):123–403, 1981.

[41] Walter Lengauer. Properties of bulk $\delta$-tin 1-x prepared by nitrogen diffusion into titanium metal. *Journal of alloys and compounds*, 186(2):293–307, 1992.

[42] R. N. Shenoy, J. Unnam, and R. K. Clark. Oxidation and embrittlement of Ti-6Al-2Sn-4Zr-2Mo alloy. *Oxidation of Metals*, 26(1):105–124, 1986.

[43] W. Sinke, G. P. A. Frijlink, and F. W. Saris. Oxygen in titanium nitride diffusion barriers. *Applied Physics Letters*, 47(5):471–473, 1985.

[44] J. Unnam, R. N. Shenoy, and R. K. Clark. Oxidation of commercial purity titanium. *Oxidation of Metals*, 26(3):231–252, 1986.

[45] G. Cassar, J. C. Avelar-Batista Wilson, S. Banfield, J. Housden, M. Fenech, A. Matthews, and A. Leyland. Evaluating the effects of plasma diffusion processing and duplex diffusion/PVD-coating on the fatigue performance of Ti-6Al-4V alloy. *International Journal of Fatigue*, 33(9):1313–1323, 9 2011.

[46] N. Kashaev, H-R. Stock, and P. Mayr. Nitriding of Ti-6Al-4V alloy in the plasma of an intensified glow discharge. *Metal Science and Heat Treatment*, 46(7):294–298, 2004.

[47] FW Wood and OG Paasche. Dubious details of nitrogen diffusion in nitrided titanium. *Thin Solid Films*, 40:131–137, 1977.

[48] H. Dong and X. Y. Li. Oxygen boost diffusion for the deep-case hardening of titanium alloys. *Materials Science and Engineering: A*, 280(2):303–310, 2000.

[49] T. A. Parthasarathy, W. J. Porter, S. Boone, R. John, and P. Martin. Life prediction under tension of titanium alloys that develop an oxygenated brittle case during use. *Scripta Materialia*, 65(5):420–423, 9 2011.

[50] T. M. Mower. Degradation of titanium 6Al-4V fatigue strength due to electrical discharge machining. *International Journal of Fatigue*, 64:84–96, 7 2014.

[51] E. M. M. Sutter and G. J. Goetz-Grandmont. The behaviour of titanium in nitric-hydrofluoric acid solutions. *Corrosion Science*, 30(4-5):461–476, 1990.

[52] K. Forsberg T. Schneiker. Process chemistry and acid management for titanium pickling processes. *VP Research and Development Scanacon AB, Stockholm, Sweden*, 2014.

[53] M. A. Daeubler and D. Helm. Influence of long time exposure at elevated temperatures in air on mechanical properties of the high temperature titanium alloy, IMI834. In *Proc. Int. Conf. on Titanium Products and Applications, Orlando, Florida*, pages 244–255, 1990.

[54] R. Clark, W. D. Dover, and L. J. Bond. The effect of crack closure on the reliability of NDT predictions of crack size. *NDT international*, 20(5):269–275, 1987.

[55] J. D. Carroll, W. Abuzaid, J. Lambros, and H. Sehitoglu. High resolution digital image correlation measurements of strain accumulation in fatigue crack growth. *International Journal of Fatigue*, 57:140–150, 12 2013.

[56] Bing Pan, Kemao Qian, Huimin Xie, and Anand Asundi. Two-dimensional digital image correlation for in-plane displacement and strain measurement: a review. *Measurement science and technology*, 20(6):062001, 2009.

[57] P. L. Reu, W. Sweatt, T. Miller, and D. Fleming. Camera system resolution and its influence on digital image correlation. *Experimental Mechanics*, 55(1):9–25, 2015.

[58] I. Bantounas, D. Dye, and T. C. Lindley. The effect of grain orientation on fracture morphology during high-cycle fatigue of Ti-6Al-4V. *Acta Materialia*, 57(12):3584–3595, 2009.

[59] James C. Williams, Rodney R. Boyer, and Martin J. Blackburn. The influence of microstructure on the fracture topography of titanium alloys. Technical report, DTIC Document, 1968.

[60] B. Sefer. Oxidation and -$\alpha$-case phenomena in titanium alloys used in aerospace industry: Ti-6Al-2Sn-4Zr-2Mo and Ti-6Al-4V. 2014.

[61] M. Park, Y-H. Hwang, Y-S. Choi, and T-G. Kim. Analysis of a J69-T-25 engine turbine blade fracture. *Engineering Failure Analysis*, 9(5):593–601, 2002.

[62] J. R. Laguna-Camacho, L. Y. Villagrán-Villegas, H. Martínez-García, G. Juárez-Morales, M. I. Cruz-Orduña, M. Vite-Torres, L. Ríos-Velasco, and I. Hernández-Romero. A study of the wear damage on gas turbine blades. *Engineering Failure Analysis*, 61:88–99, 2016.

[63] J. Tian, W. Wang, W. Yan, Z. Jiang, Y. Shan, and K. Yang. Cracking due to Cu and Ni segregation in a 17-4 PH stainless steel piston rod. *Engineering Failure Analysis*, 65:57–64, 2016.

[64] E. A. Saunders, T. P. Chapman, A. R. M. Walker, T. C. Lindley, R. J. Chater, V. A. Vorontsov, D. Rugg, and D. Dye. Understanding the "Blue Spot": Sodium chloride hot salt stress-corrosion cracking in titanium-6246 during fatigue testing at low pressure. *Engineering Failure Analysis*, 61:2–20, 2016.

[65] M. Benedetti, J. Heidimann, J. O. O. Peters, and G. Lutjering. Influence of sharp microstructural gradients on the fatigue crack growth resistance of -$\alpha$+$\beta$ and near–$\alpha$ titanium alloys. *Fatigue Fracture of Engineering Materials and Structures*, 28(10):909–922, 10 2005.

[66] G Lütjering. Influence of processing on microstructure and mechanical properties of ($\alpha$+ $\beta$) titanium alloys. *Materials Science and Engineering: A*, 243(1):32–45, 1998.

[67] B. Ollivier, S. J. Dowey, S. J. Young, and A. Matthews. Adhesion assessment of DLC films on PET using a simple tensile tester: Comparison of different theories. *Journal of Adhesion Science and Technology*, 9(6):769–784, 1 1995.

[68] V. Sinha, M. J. Mills, and J. C. Williams. Crystallography of fracture facets in a near-$\alpha$ titanium alloy. *Metallurgical and Materials Transactions A*, 37(6):2015–2026, 2006.

[69] D. C. Slavik, J. A. Wert, and R. P. Gangloff. Determining fracture facet crystallography using electron backscatter patterns and quantitative tilt fractography. *Journal of Materials Research*, 8(10):2482–2491, 1993.

[70] A.L. Pilchak, R.E.A. Williams, and J.C. Williams. Crystallography of fatigue crack initiation and growth in fully lamellar Ti-6Al-4V. *Metall and Mat Trans A*, 41(1):106–124, 11 2009.

[71] M. R. Bache, F. P. E. Dunne, and C. Madrigal. Experimental and crystal plasticity studies of deformation and crack nucleation in a titanium alloy. *The Journal of Strain Analysis for Engineering Design*, 45(5):391–399, 7 2010.

[72] M. R. Bache, M Cope, H. M. Davies, W. J. Evans, and G. Harrison. Dwell sensitive fatigue in a near -$\alpha$ titanium alloy at ambient temperature. *International Journal of Fatigue*, 19(93):83–88, 1997.

[73] E. Sackett, L. Germain, and M. Bache. Crystal plasticity, fatigue crack initiation and fatigue performance of advanced titanium alloys. *International Journal of Fatigue*, 29(9-11):2015–2021, 9 2007.

[74] F.P.E. Dunne and D. Rugg. On the mechanisms of fatigue facet nucleation in titanium alloys. *Fatigue & Fracture of Engineering Materials & Structures*, 31(11):949–958, 11 2008.

[75] M. R. Bache, W. J. Evans, and H. M. Davies. Electron back scattered diffraction (EBSD) analysis of quasi-cleavage and hydrogen induced fractures under cyclic and dwell loading in titanium alloys. *Journal of Materials Science*, 32(13):3435–3442, 1997.

[76] W. J. Evans and M. R. Bache. Dwell-sensitive fatigue under biaxial loads in the near-$\alpha$ titanium alloy IMI685. *International Journal of Fatigue*, 16(7):443–452, 1994.

[77] I. Bantounas, T. C. Lindley, D. Rugg, and D. Dye. Effect of microtexture on fatigue cracking in Ti-6Al-4V. *Acta Materialia*, 55(16):5655–5665, 2007.

[78] M. R. Bache and W. J. Evans. Impact of texture on mechanical properties in an advanced titanium alloy. *Materials Science and Engineering: A*, 319:409–414, 2001.

[79] Jaimie Tiley, Joshua Shaffer, Adam Shiveley, Adam Pilchak, and Ayman Salem. The effect of lath orientations on oxygen ingress in titanium alloys. *Metallurgical and Materials Transactions A*, 45(2):1041–1048, 2014.

[80] David Lunt. The effect of macrozones in Ti-6Al-4V on the strain localisation behaviour. 2015.

[81] L. Germain, N. Gey, M. Humbert, P. Vo, M. Jahazi, and P. Bocher. Texture heterogeneities induced by subtransus processing of near-$\alpha$ titanium alloys. *Acta Materialia*, 56(16):4298–4308, 2008.

[82] P. O. Tympel, T. C. Lindley, E. A. Saunders, M. Dixon, and D. Dye. Macrozones and dwell fatigue crack initiation in Ti-6Al-4V. In *Proceedings of the 13th World Conference on Titanium*, pages 985–991. Wiley Online Library.

[83] J. I. Gersten and W. Smith. *The Physics and Chemistry of Materials*. John Wiley and Sons, Inc., 2001.

[84] M. T. Cope, D. R. Evetts, and N. Ridley. Post-forming tensile properties of superplastic Ti-6Al-4V alloy. *Materials Science and Technology*, 3(6):455–461, 1987.

[85] R. W. Evans, R. J. Hull, and B. Wilshire. The effects of -$\alpha$-case formation on the creep fracture properties of the high-temperature titanium alloy IMI834. *Journal of Materials Processing Technology*, 56(1-4):492–501, 1996.

[86] G. Cassar, A. Matthews, and A. Leyland. Triode plasma diffusion treatment of titanium alloys. *Surface and Coatings Technology*, 212:20–31, 11 2012.

[87] H-S. Lee, J-H. Yoon, and Y-M. Yi. Oxidation behavior of titanium alloy under diffusion bonding. *Thermochimica Acta*, 455(1-2):105–108, 4 2007.

[88] D. G. Sanders and M. Ramulu. Examination of superplastic forming combined with diffusion bonding for titanium: Perspective from experience. *Journal of Materials Engineering and Performance*, 13(6):744–752, 2004.

[89] Y. W. Xun and M. J. Tan. Applications of superplastic forming and diffusion bonding to hollow engine blades. *Journal of Materials Processing Technology*, 99(1):80–85, 2000.

[90] A. K. Mukherjee M. L. Meier, D. R. Lesuer. The effects of the -$\alpha/\beta$ phase proportion on the superplasticity of Ti-6Al-4V and iron-modified Ti-6Al-4V. *Materials Science and Engineering: A*, 154:165–173, 1992.

[91] AI Kahveci and GE Welsch. Effect of oxygen on the hardness and $\alpha/\beta$ phase ratio of ti-6al-4v alloy. *Scripta metallurgica*, 20(9):1287–1290, 1986.

[92] T. Zhang, Y. Liu, D. G. Sanders, B. Liu, W. Zhang, and C. Zhou. Development of fine-grain size titanium 6Al-4V alloy sheet material for low temperature superplastic forming. *Materials Science and Engineering: A*, 608:265–272, 2014.

[93] M. T. Cope and N. Ridley. Superplastic deformation characteristics of microduplex Ti-6Al-4V alloy. *Materials Science and Technology*, 2(2):140–145, 1986.

[94] M. T. Cope, D. R. Evetts, and N. Ridley. Superplastic deformation characteristics of two microduplex titanium alloys. *Journal of Materials Science*, 21(11):4003–4008, 1986.

[95] P. N. Comley. ASTM E2448 - a unified test for determining SPF properties. *Journal of Materials Engineering and Performance*, 17(2):183–186, 2008.

[96] T. M. Roberts and M. Talebzadeh. Acoustic emission monitoring of fatigue crack propagation. *Journal of Constructional Steel Research*, 59(6):695–712, 2003.

[97] Z. Shaoqing and Z. Linruo. Effect of hydrogen on the superplasticity and microstructure of Ti-6Al-4V alloy. *Journal of Alloys and Compounds*, 218(2):233–236, 1995.

[98] Meurig Thomas. On the characterisation of subsurface deformation microstructures in aerostructural titanium alloys. 2012.